THERMOELASTIC STRESS ANALYSIS TECHNIQUES FOR MIXED MODE FRACTURE AND STOCHASTIC FATIGUE OF COMPOSITE MATERIALS

A Dissertation
Presented to
The Academic Faculty

by

Bo-Siou Wei

In Partial Fulfillment
of the Requirements for the Degree
Doctor of Philosophy in the
School of Civil and Environmental Engineering

Georgia Institute of Technology
August 2008

THERMOELASTIC STRESS ANALYSIS TECHNIQUES FOR MIXED MODE FRACTURE AND STOCHASTIC FATIGUE OF COMPOSITE MATERIALS

Approved by:

Dr. Rami Haj-Ali, Advisor
School of Civil and Environmental Engineering
Georgia Institute of Technology

Dr. Bruce Ellingwood
School of Civil and Environmental Engineering
Georgia Institute of Technology

Dr. Kenneth Will
School of Civil and Environmental Engineering
Georgia Institute of Technology

Dr. Arash Yavari
School of Civil and Environmental Engineering
Georgia Institute of Technology

Dr. Richard Neu
School of Mechanical Engineering
Georgia Institute of Technology

Date Approved: April 22, 2008

ACKNOWLEDGEMENTS

I would like to express my deep gratitude to my advisor, Dr. Rami Haj-Ali, for his knowledgeable guidance to research and advanced solid mechanics. He always raises sharp questions and provides effective solutions to solve the problems. I will never forget the time we spent in the coffee shop to review our journal publications together. He is a great mentor as an advisor and a friend. I would also like to thank my Ph.D. committee members, Dr. Ellingwood, Dr. Will, Dr, Yavari, and Dr. Neu, for their detailed review and discussions we had to improve this research work.

My admiration and thanks also go to my colleges. Interacting with Joonho, Hee-sun, and Hoankee always makes the work more enjoyable. I would like to express my special thanks to Shane. We have gone through numerous research experiments, industrial projects, and discussions on research and life. I also thank Dr. Armanios, Xinyuan, Dr. El-Hajjar, and Dr. Popil for collaborating with me on various journal publications. The time I spent with my friends at Georgia Tech brings back great memories for me.

I owe my most sincere gratitude to my family. My mother-in-law and sister-in-law helped us when we had our lovely baby, Iris. My parents' endless love and encouragement supported me throughout my entire education from the beginning until the Ph.D. Finally, my deepest thanks and appreciation go to my wife, Te-Ling, and our lovely daughter, Iris. They let me know how beautiful life is and future can be. They continue to be the greatest motivation in my life.

TABLE OF CONTENTS

LIST OF TABLES

LIST OF FIGURES

SUMMARY

This study develops new quantitative thermoelastic stress analysis (TSA) techniques for fracture and fatigue damage analysis of composite materials.

The first part deals with the thermo-mechanical derivation of two quantitative TSA techniques applied to orthotropic composites with and without a transversely-isotropic surface coating layer. The new TSA test procedures are derived in order to relate the thermal infrared (IR) images with the sum of in-plane strains multiplied by two newly defined material constants that can be experimentally pre-calibrated. Experiments are performed to verify the TSA methods with finite element (FE) numerical results along with available anisotropic elasticity solution.

The second part of this study applies the quantitative TSA techniques together with the Lekhnitskii's general anisotropic elasticity solution to calculate mixed-mode stress intensity factors (SIFs) in cracked composite materials. The cracked composite coupons are subjected to off-axis loadings with respect to four different material angles in order to generate mixed-mode SIFs. A least-squares method is used to correlate the sum of in-plane strains from the elasticity solution with the measured TSA test results. The mode-I and mode-II SIFs are determined from eccentrically loaded single-edge-notch tension (ESE(T)) composite specimens. The FE models and virtual crack closure technique (VCCT) are utilized for comparisons.

In the third part, a new stochastic model is proposed to generate S-N curves accounting for the variability of the fatigue process. This cumulative damage Markov chain model (MCM) requires a limited number of fatigue tests for calibrating the probability

transition matrix (PTM) in the Markov chain model and mean fatigue cycles to failure from experiments. In order to construct the MCM stochastic S-N curve, an iterative procedure is required to predict the mean cycles to failure. Fatigue tests are conducted in this study to demonstrate the MCM method. Twenty-one open-hole S2-glass laminates are fatigue-cycled at two different stress levels. The coupon overall stiffness and surface-ply TSA damage area have been used as two damage metrics. The MCM can satisfactorily describe the overall fatigue damage evolution for a limited number of coupons (less than 6) subjected to a given specific stress level. The stochastic S-N curve can be constructed using at least two sets of fatigue tests under different stress levels. Three available fatigue tests for different E-glass laminates from the literature are also investigated using the proposed MCM approach. The results show the MCM method can provide the stochastic S-N curves for different composite systems and a wide range of fatigue cycles.

CHAPTER 1

INTRODUCTION

Fracture mechanics (FM) employs energy and stress-intensity based metrics and measures in order to predict potential failure in structures. Traditional stress-based design methodologies take into account applied stress and yield or ultimate strength. On the other hand, fracture mechanics design-based methods take into account applied stress, fracture toughness, and assume flaw size. Existing fracture procedures have been widely advanced and accepted for the failure analysis of metallic materials. However, the use of FM in fiber reinforced polymeric (FRP) materials is relatively new and not widely used. This is because of the complicated nature of fracture and damage behavior in FRP materials due to the heterogeneous and anisotropic nature of FRP materials. The latter leads to fracture branching and brittle crack growth under unstable mixed modes. The change in direction of the crack growth as a function of time and loading (i.e. non-self-similar crack growth) is also due to the layered nature of laminated anisotropic composites. This damage in FRP materials is further complicated by the various intra and inter-layer interacting failure mechanisms, such as matrix cracking, fiber bridging, fiber rupture, fiber pullout, microbuckling, and delamination.

Fatigue damage tolerance is often taken into account in the design of FRP structures. Therefore, methods and techniques for service life prediction are crucial. The well-known S-N curve used for characterizing the fatigue behavior of metallic materials has been also adopted for open-hole and other well-defined FRP coupons. Due to the composite material heterogeneity, the spatial damage distribution during fatigue experi-

ments is usually scattered rather than behaving in a deterministic fashion within the specimens. Therefore, the fatigue lives of different specimens exhibit relatively large variations. A probabilistic damage approach is advantageous over a deterministic method in order to account for this variability of the test results along with other mechanical properties.

Conventional fracture mechanics in combination with new full-field non-destructive evaluation tools such as infrared thermography (IR-T) is attractive since the full-field stress/strain revealed by the IR-T can be related to stiffness/damage distribution. Thermoelastic stress analysis (TSA) techniques can be used to analyze the measured IR images and provide a more sophisticated methodology by which engineers can predict sudden and catastrophic failure in FRP structures. Therefore, new IR-TSA based techniques can be used in the future to monitor full-scale composite structures. The TSA techniques can be also applied to assess the fatigue damage and develop applicable damage metrics to evaluate the fatigue life utilizing the S-N curve. This introductory chapter reviews a number of significant studies that contributed to the development of TSA techniques. In addition, fracture mechanics and stochastic fatigue studies using cumulative damage models are reviewed. The advantages and limitations of previous models are highlighted. The objective and research approach of this study will be outlined in the last section of this chapter.

1.1 Infrared Thermography and Thermoelastic Stress Analysis (TSA)

Infrared (IR) thermography can be used to measure temperature changes on the surface of materials due to stress generated thermal fields or externally applied thermal fields. In order to detect temperature changes due to applied mechanical loads, a sensitive infrared camera is needed. Sensitivities commonly reported during the 1980's were 0.1K, and troubles with data measurements were reported due to ambient conditions in many cases. Since that time, electronic hardware and enhanced computer software methods have been introduced to process and measure thermal data. Stress Pattern Analysis by Thermal Emission (SPATE) is a tool that was introduced in 1970's, where points are scanned in a point-by-point manner under adjustable computer control. This tool has been developed into fast and accurate full-field Thermoelastic Stress Analysis (TSA) methods. While the SPATE type methods required 1-2 hours to obtain a single image scanning 50 points per second, thermoelasticity measurement systems today have a thermal resolution of approximately 1 mK for full-field image integration time of one minute or less. This temperature sensitivity and increased hardware sophistication allow for wide application of remote sensing capabilities for materials and structural components to exploit damage detection and assessment.

Thermography can be used to detect anomalies spatially because imperfections disrupt heat and energy transfer. Excitation sources can be applied externally using thermal or mechanical sources to generate coupled stress and thermal fields. These excitation sources can be in the form of mechanical loads, direct heat, and ultrasonic stress waves, etc. The overall goal is to subject the structures or the materials to thermo-mechanical

deformation that produce spatial variations in the surface temperatures and allow correlation between measured IR field and the stress or strain on the surface. Under adiabatic and reversible conditions in isotropic materials, the application of a small cyclic load will induce small and repeated variations in temperature that are proportional to the sum of principle stresses. Lord Kelvin (1878) was the first to propose this thermoelastic principal. He used thermodynamics-based derivations to obtain a linear relation between the temperature change and the first stress invariant. The recent advances and affordability of charged-coupled-device (CCD) cameras, with fast acquisition systems, have led to a powerful and quantitative thermoelastic stress analysis (TSA) measurement technique. The first invariant of the stress can be measured on the surface of cyclically loaded coupons made of homogeneous materials. The sum of in-plane stresses or strains obtained by the quantitative TSA techniques can be used to evaluate the material behaviors due to non-mechanical or mechanical loadings.

The TSA method has been also applied in isotropic materials to measure stresses with and without damage. Limited attention has been given to quantitative TSA applied to FRP composite materials. Several difficulties may arise in the use of TSA in composites, such as the effects of anisotropic substrates and surface coating. Temperature diffusion and non-adiabatic approaches have been proposed to model the thermoelastic effect in composites. Dunn (1993) used a two-dimensional heat equation and finite-difference method to account for the thermal conduction in the aluminum double overlap joint region. The TSA, finite difference, and FE methods were utilized to investigate phase changes due to different load frequencies and sizes of specimens. It was shown that the thermal conduction was significantly reduced for the increasing sizes of specimens under

loading frequency of 10 Hz. The TSA technique was also used for qualitative and limited quantitative studies. For example, Zhang et al. (1989, 1990) studied stress concentrations in the knit-yarn fiber intersections in a unidirectional carbon/epoxy laminate. They also addressed the effect of the surface resin thickness. They observed via TSA techniques that the two-parameter Weibull distribution function can describe the distribution of stress concentration factors on the laminate surface. They stated that the adiabatic condition was more difficult to achieve due to the non-uniformly distributed fibers. The absolute temperature and surface emissivity were shown to affect the TSA signal in their study. Dulieu-Smith et al. (1997) reported test results of a full-field stress characterization on a woven tee-joint with GFRP laminated fillets. They used Schapery's formulation (1968) to calculate the coefficients of thermal expansion (CTE) in composites, and then applied the CTE to simulated the infrared signal with FE methods. The experimental TSA field was in good agreement with FE simulations.

Adding a thick resin surface layer was found to stabilize the TSA signal and attenuate the heat transfer from the carbon/epoxy inner layers. Mackenzie (1989) and Welch and Zickel (1993) investigated the characteristics of the thermal radiation signal emitted from different surface coatings. The formulation of Mackenzie for the thermal wave problem characterized the IR flux amplitude from the surface as a function of IR reflection and thermal material properties of the considered substrate-coat-air system. Using material properties of a typical paint coating, a range of thicknesses and applied thermal frequencies was identified to allow the coat to act as a witness layer for strains. Barone and Patterson (1998) proposed using a polymeric coating to extract the strain field from TSA measurements of isotropic materials. Their method was applied for iso-

tropic substrates. Good correlation between analytical solutions and measured TSA responses was obtained for aluminum plates with circular holes. El-Hajjar and Haj-Ali (2003, 2004a, 2004b, 2005) proposed a technique to quantify the thermoelastic stress signal of thick-section orthotropic-layered composites. They showed that the sum of the in-plane strains in a transversely isotropic top layer (or a coat) is proportional to the thermoelastic signal. One proportionality coefficient was needed with the measured thermoelastic signals in order to determine the sum of the in-plane surface strains experimentally. Haj-Ali et al. (2008) later expanded the quantitative TSA for the composites with orthotropic surface coat. Two separate thermo-mechanical calibrations were required in the longitudinal and transverse material orientations. They compared their method with several tests and FE analytical solutions. Their method showed good agreement between TSA experiments and FE simulations.

The TSA techniques together with thermal dynamics theory have been shown to be capable of obtaining the sum of in-plane stresses/strains on the surface of cyclically loaded materials. The TSA techniques can also differentiate the anomalies or detect stress redistribution due to localized damages in materials. These obtained full-field thermal images can then be applied to investigate the material properties or be metrics in damage models. The following sections introduce the history and TSA applications in fracture and fatigue mechanics of composite materials.

1.2 Fracture in Composite Materials

Linear elastic fracture mechanics (LEFM) emerged from linear elasticity to solve for the stress and deformation fields around cracks in continuous media. These solutions and fracture-based material properties are used in design problems of materials and struc-

tures with defects. Two methodologies have developed together over the past century. Inglis (1913) analyzed elliptical holes in flat plates subjected to stresses from which the solution for the special case of a crack could be derived. The stress concentration factor was defined the ratio of the local maximum stress and the remote stress. It can be used to measure how the remote stress is amplified at the crack tip. Griffith (1920) was the first to develop a quantitative connection between fracture stress and flaw size in an elliptical hole. His fracture mechanics model was based on the first law of thermodynamics that relates the change in the total energy of a system due to the formation and growth of a crack. He proposed the idea that a crack growth reduced the stored elastic strain energy. Griffith's work was limited to the fracture of brittle materials, and his model assumed that the work of fracture was related only to crack surface energy. Irwin (1948) extended Griffith's theory to ductile materials, and introduced a concept of strain energy release rate (ERR), G, which was the rate of change in potential energy due to crack growth in a linear elastic material. The strain energy release rate, G, can be equated to a critical ERR value, G_c, that defined when a crack starts to propagate. By using Westgaard's elasticity solution (1939), Irwin (1957) showed that the stress field expansion near the crack tip was related to a constant multiplied by the coefficient of the square root of the distance from crack tip. This constant was called the stress intensity factor (SIF), K. The SIF was shown to be directly related to the strain energy release rate. Sih, Paris, and Irwin (1965) employed Lekhnitskii's (1963) solution to relate strain energy release rate to the SIFs for anisotropic materials. The mixed-mode case in absence of the tearing mode was also presented. They showed that for anisotropic materials where the crack was aligned with one of the material symmetries, the SIF in mode-I and II were not coupled. In the case where

the crack was not aligned with material symmetry, the SIFs were both coupled and needed to be solved simultaneously.

In the area of elasto-plastic fracture mechanics (EPFM), Dugdale (1960) introduced strip-yield cohesive models for crack-tip plasticity. He stated that the LEFM stress was bound by a material limit and not an infinite value at the crack tip due to plasticity. He developed a center crack model considering a state with constant distributed stresses applied in the crack so that the stresses tended to close the crack and removed the stress singularity at the crack tip. For a thin elastic-perfectly plastic material loaded in tension, yielding was confined to a narrow band along the crack line. In fact, if the plastic zone was much smaller in comparison to the length of the crack, the stress intensity factor was still a reliable factor for fracture mechanism. Independent developments by Wells (1963) introduced a concept for modeling the plastic zone at crack tips. The idea was based on a critical displacement at the crack tip, known as the crack opening displacement (COD), which could be used to characterize crack extension. He evaluated the COD for a center crack in an infinite elastic body. Wells believed that the COD criterion was consistent with LEFM and was applicable even beyond general yielding. The development by Wells was now known as the crack-tip opening displacement (CTOD) criterion. Another approach in EPFM was proposed by Rice (1968), called the J-integral, which was widely used in the U.S. He generalized the energy release rate concept to elastic-plastic materials and showed that this energy release rate was equivalent to a path independent line integral expression. Begley and Landes (1972) applied the J-integral to characterize fracture toughness of reactor steels, and developed a standard procedure that is now reflected in ASTM standard E813-81. Hutchinson (1968) and Rice and Rosengren (1968) inde-

pendently related the J-integral to the crack tip stress fields in non-linear elastic materials. By using the power law for the material properties, they derived the so-called HRR (Hutchinson-Rice-Rosengren) fields by assuming small strains and deformation plasticity. Later, Shih (1981) used the HRR singularity to relate J and CTOD for a given material. Hence, the fracture toughness can be quantified in terms of a critical value of either J or CTOD.

Dally and Sanford (1987) proposed an experimental method to determine the mode-I SIF in isotropic materials using a strain gauge. The Westergaard stress function was used to calculate the mode-I SIF based on strain gauge measurements. To obtain an accurate SIF, they determined the optimal location and orientation of the strain gauge needed to eliminate the effect of non-dominant terms and increase the contribution of the mode-I SIF. Shukla et al. (1989) extended Dally and Sanford's method to orthotropic materials. They used Airy's function for a two-dimensional orthotropic body and solved for the strain field equations. The study of radial position and size of the strain gauge were also included in their work. Maleski, Kirugulige, and Tippur (2004) also extended Dally and Sanford's method to calculate the mode-I SIF and T-stress which was a constant stress acting parallel to the crack and related to one of the coefficients in the stress expansion terms of the radius, which was a non-singular term. They applied a bi-axial strain gauge to calculate the stain difference. The strain difference can be used in the strain expansion, and then the T-stress was determined by the coefficient of the expansion term. The optimal angular position of the strain gauges was also discussed.

Rybicki and Kanninen (1977) developed a virtual crack closure technique (VCCT) to evaluate the SIFs. The technique was based on the crack closure integral, which can

be used in a finite element analysis (FEA) with a coarse mesh. Tong et al. (1973) were among the first to introduce a super element to determine the mode-I and mode-II SIFs near the crack tip in isotropic materials. The super element was based on the hybrid-element concept. The stress and deformation fields within the element were complex expansion polynomials in terms of the element spatial variables. The hybrid element was connected to the displacement-based elements through compatibility constraints. By the comparison with conventional triangular and quadrilateral elements, the super element can achieve a higher accuracy with lower degrees of freedom. Tong (1975) extended his previous work and adopted Lekhnitskii's solution (1963) to develop a super element which can be used for orthotropic materials in which the principal directions of the material properties were in coincidence with the geometrical axes of the plate. Khalil et al. (1986) followed Tong's idea and developed a super element in which the material orthotropy can have some angle with respect to the geometrical axes of the plate.

Ju and Rowlands (2003) applied the stress field solution expansion from Khalil et al. (1986) together with a thermoelastic stress analysis approach to determine the SIFs of off-axis crack orthotropic composites. The thermoelastic stress signal was assumed to relate to the in-plane direct stresses through two separate coefficients. They used finite element analysis to calibrate the two thermo-mechanical coefficients to correlate the thermoelastic signals to the direct stresses. The SIFs from Lekhnitskii's solution via thermoelastic stress signals were calculated and compared with those obtained from FE models. Diaz et al. (2004) employed Muskhelishvili's (1977) complex variable elasticity solution method in isotropic materials and the TSA technique to determine the SIFs of welded steel plates under fatigue loading. They found a suitable region of TSA values for

calculating SIFs, and found that the SIFs were affected by residual stress. Tomlinson, and Marsavina (2004), Diaz et al. (2004), and Diaz, Yates, and Patterson (2004) used Muskhelishvili's solution (1977) to calculate the SIFs in metallic materials using TSA techniques. They provided methods to determine the location of the crack tip and studied the crack closure and residual stress in their research. The SIFs were also determined from the fatigue crack in their work. Cavaliere et al. (2007) applied TSA techniques to investigate the fatigue behavior of metal matrix composite sheets joined by friction stir welding process. They stated that the infrared signal relating the sum of principal stresses can exhibit the stress concentration by showing higher IR signal, and the stress intensity factors can be calculated for a notched specimen. Haj-Ali et al. (2008) developed two methods for quantitative TSA measurement of surface strains on FRP orthotropic composites. They showed the mixed-mode SIFs can be calculated using their method and Lekhnitskii's solution for the stress field ahead of a crack tip in an anisotropic medium.

1.3 Fatigue in Composite Materials

Fiber-reinforced composite materials are employed extensively in higher load-bearing structures for their enhanced thermo-mechanical, electromagnetic, stiffness/strength-to-weight ratio and fatigue performance benefits. Different experimental methods and techniques, such as radiography, photoelasticity, acoustic emission, and thermography have been applied to investigate the fatigue life of fiber reinforced polymers. A common notation for the stacking sequences of laminated composite can be expressed (Gibson, 1994) as $[(\theta_1)_{k1}/(\theta_2)_{k2}/\ldots/(\theta_n)_{kn}]_{ms}$ where the (θ_n) is the fiber orientation for each ply; (kn) represents the number of plies; (m) is the number of the repeated stack, and the (s) represents symmetry if any. Several researchers have conducted fatigue stud-

ies in composite laminates. Bakis et al. (1989) related the residual strength, stiffness, and fatigue life to their corresponding damage states obtained from photoelastic coating and thermal emission experiments for circular notched graphite/epoxy laminates subjected to fully reversed fatigue loads. They observed the damage initiated around the hole for quasi-isotropic and orthotropic laminates. Matrix cracking and delamination patterns were different in both cases due to the interaction between adjacent plies. Compared with photoelastic data, the thermal emission was more sensitive to the minute deformations near fracture paths in surface plies. Swain et al. (1993) investigated the effect of interleaves on the damage mechanisms and residual strength of notched composite laminates subjected to axial fatigue loading. Interleaving is the act of adding adhesive layers between plies, locally strengthening ply interface by reducing interlaminar stresses. Thus, more energy is required to propagate a delamination crack. They chose AS4/985 and AS4/1808 carbon epoxy laminates with an open-hole in $[0/45/90/-45]_{2s}$ and $[0/45/90/-45]_{4s}$ stacking, respectively. They described the effect of interleaving with normalized stiffness versus normalized life curves and by looking at residual strength and evaluated delamination using X-ray radiography and dye-penetration. Fatigue loading of the laminates was performed at 10 Hz with an R-ratio ($\sigma_{min}/\sigma_{max}$) of 0.1, and at specific intervals the test was stopped and a stiffness value was obtained by measuring the strain with a one-inch gauge-length extensometer centered over the open hole. Delamination originated from the hole and linked with edge damage. Although the authors were able to use traditional methods such as stiffness and strength in a quantitative measure of cumulative damage, their X-ray radiography showed matrix cracking, delamination, and other damage mechanisms only in a qualitative manner. O'Brien (1993) and O'Brien and Hooper

(1993) investigated damage and failure of angle ply laminated composites at or near the free edge using X-ray radiography and optical methods. They investigated laminates using 3D FEA for each configuration looking at in-plane shear and transverse normal stresses as indicators of matrix cracks in off-axis plies and local delaminations. Microscopes and X-ray radiography on straight coupons of AS4/350-6 graphite epoxy prepreg with $[\theta_2/\theta_2/-\theta_2]_s$ lay-ups where $\theta = (15°, 20°, 25°, 30°)$ were used qualitatively in order to gauge the initiation of matrix cracking and delamination providing some measure of validation for 3D FEA. They developed delamination models to describe the load-life fatigue behavior of angle-ply laminates. Tamuzs et al. (2004a, 2004b) conducted fatigue tests on woven orthotropic composite laminates in off-axis loadings. They developed a quadratic master curve function to describe the strength, deformation, and degradation of the stiffness. This master curve was obtained by the best fit of the experimental data through the fatigue life of the laminates, and showed that the reduction of the stiffness before fatigue failure did not depend on the loading angles with respect to the material angles. An S-N master curve was also developed by replacing the applied stresses in the conventional S-N curve with a modified stress function. The S-N master curve was an innovative alternative way of representing damage accumulation using a stochastic approach. However, the variability in composite fatigue data was not fully taken into account.

1.4 Cumulative Damage Modeling using Markov Chain Theories

Spatial damage distributions during fatigue experiments of uniform samples are usually scattered due to the material heterogeneity. A probabilistic damage approach is therefore advantageous over a deterministic method in order to account for the relatively

wide variability of material test results. Bogdanoff et al. (1978a, 1978b, 1978c, 1980a, 1980b) were among the first to introduce a new cumulative damage model using stochastic processes. A Markov chain model was used to take into account the variability (e.g., manufacturing and service loads). They further pointed out that the life testing in which time to failure was recorded does not provide enough information for the member function (mf) which is defined as damage state/index as a function of time or fatigue cycles. Thus, they divided the probability transition matrix into different segment numbers to improve the accuracy. Results of different probabilities in the transition matrix of the Markov chain model were investigated analytically. They compared previous experimental work done by other researchers with Markov chain models. Bogdanoff and Kozin (1982) called the cumulative damage model the "B-model" and converted it to a nonstationary model using a time transformation condensation method. Polynomial equations were used for mapping the time in different domains. To maintain the definition of the transition matrix, a condensation method was used in their models. This allows the stationary Markov chain to become a nonstationary model. Kozin and Bogdanoff (1983) employed the B-model together with the Paris law to describe the fatigue process. Rowatt and Spanos (1998) applied a cumulative damage model to laminated composite materials. The time transformation condensation method was also employed in their work. They investigated the evolution of compliance in composite materials subjected to a constant amplitude fatigue loading. The change in compliance was related to the individual damage mechanisms of a critical element within the laminate to achieve a life prediction of the material system. Their experimental data was based on a single mid-specimen axial extensometer measured in a straight composite coupon. Xi et al. (1997, 2000) used a

cumulative damage model together with the R-curve[1] to predict the damage evolution of a three-point bend concrete beam. They used a geometric series to generalize transition probabilities in Bogdanoff and Kozin's approach. A recursive expression was proposed to obtain the probabilities in the transition matrix. The R-curve was obtained in order to provide the crack extension, which was required in the recursion, for a specific specimen geometry and given loading conditions. Wu and Ni (2004) studied three different damage approaches: Markov chain model, Yang's power law model, and a polynomial model for fatigue crack growth. They performed constant and random amplitude loadings on aluminum-alloy compact tension (C(T)) specimens, and they used the three models to predict the fatigue behavior of the specimens. For their case of random loading, the polynomial model fitted the experiments better than the Yang's model. They pointed out that the nonstationary Markov chain model was sufficient to describe the fatigue process and also suitable for random loading. Tanimoto (2006) applied different stress levels to carbon/epoxy laminates and observed that the fatigue life had more scatter in the 10^5-10^6 cycle range. He used a Weibull probability model to construct the probability of failure at different stress amplitudes through the fatigue life. The dominant failure mode in his experiments was delamination. Liu and Mahadevan (2005) utilized Monte Carlo simulations combined with Miner's rule that took into account the coefficients in Tsai-Hill failure criterion in order to estimate the fatigue life of composite laminates. They assumed the random variable such as ply thickness, elastic modulus, and ply angle as normal distribution for Monte Carlo simulations. Their numerical method had good agreement with

[1] A classical term in fracture mechanics (e.g., Anderson, 2005), defined as the plot of material resistance to crack extension, R, versus crack extension, is called R-curve. It is often used to determine the stability of the crack growth.

the experiments conduced by Mandell and Samborsky (1997). Liu and Mahadevan (2007) later employed a nonlinear fatigue damage accumulation method with a stochastic S-N curve technique to predict the fatigue life of metallic materials under various stress levels. The fatigue data was obtained from the literature for different materials with variable or constant amplitude loadings. A required coefficient for formulating the nonlinear damage accumulation rule was calibrated with the experimental fatigue data. The coefficient accounted for material properties and applied stress levels, which were not usually considered in a typical linear damage accumulation rule. The Karhunen-Loeve expansion method (1977) was conducted to generate their stochastic S-N curves. Numerical simulations using their proposed damage method yielded satisfactory agreement with the experimental fatigue life.

Cumulative damage models were proposed to evaluate material behavior under fatigue processes using traditional contact-based measurements, including strain gauges and extensometers. Rowatt and Spanos (1998) used extensometer data gathered from 17 coupons to investigate changes in compliance that was related to the stochastic evolution of fatigue damage in composite materials. Wu and Ni (2004) used dial gages to measure fatigue crack growth in metallic C(T) specimens. Relatively new differential infrared thermography was proposed and used to track the fatigue damage in composite materials. The graphite/epoxy laminates with [±45] and [0/90^{o}] ply configuration were investigated by Lohr et al (1987). In their experiment, the measured temperature was seen to decrease as the number of cycles increased due to cracking in the epoxy surface layer. This effect was more pronounced under higher frequencies and made quantitative TSA difficult for these composite material systems. Zhang and Sandor (1990) used TSA techniques and

extensometer measurement to investigate the fatigue damage in a glass fiber/epoxy laminate. They obtained an effective density parameter from TSA method and used it in a TSA damage index formulation. The stiffness damage index formulation from an extensometer was also defined. They linearly equated the two damage index formulations and thus transformed the TSA measurement into effective stiffness at a certain fatigue cycle. They stated the stiffness obtained from the TSA method extensometer was in good agreement. However, the assumption used to equate the two different damage indices was based on a linear one-to-one mapping and was not validated. The TSA techniques were applied by Johnson et. al. (2004, 2006) to investigate fatigue behavior of pultruded materials. In their study, TSA data was gathered to obtain a mean thermal effect that was related to fatigue damage and damage evolution. The elastic modulus in pultruded materials was measured by an extensometer, and showed lower sensitivity under the fatigue loading than TSA measurements. They showed that the TSA can capture the damage in the full-field center areas of coupons. They observed the departure of IR signal from a normal distribution was attributed to localization and damage. Cavaliere et al. (2007) applied TSA techniques to investigate the fatigue behavior of metal matrix composite sheets joined by a friction stir welding process. They stated that the infrared signal relating the sum of principal stresses can be used to investigate stress concentration and the stress intensity factors for notched metal matrix composite specimens.

1.5 Present Study

The applications of stress/strain analysis and damage detection are mostly limited to isotropic metallic materials. This study expands past TSA applications to anisotropic composites. Towards that goal, two new TSA methods are developed to provide the sum

of in-plane strain field for orthotropic materials via two experimental thermo-mechanical calibrations. The measured surface strain field can be used for calculating the mixed-mode SIFs in orthotropic composite materials subjected to off-axis loadings. This study also employs the full-field infrared images from the surface of fatigue composite laminates. The Markov chain theory is then used to incorporate the fatigue damage metrics from TSA and stiffness and construct stochastic S-N curves.

The chapters in this thesis are organized as follows. Chapter 2 deals with the derivation of the new quantitative TSA methods for the composites with transversely-isotropic or orthotropic surface layers. The thermo-mechanical formulations are first derived for the transversely-isotropic layer. In this derivation, one experimental calibration is required in order to map the TSA signal into sum of in-plane strains. Subsequently, the formulations for the transversely isotropic layer are proposed. Two calibration coefficients are required for the second TSA method with orthotropic materials. Experimental calibration for the two proposed quantitative TSA methods are carried out on both E-glass pultruded thick-section and S2-glass laminated composites. Test results for different composite coupons with open-hole and edge-cracks are then compared with FE simulations and anisotropic elastic solutions.

Chapter 3 employs the TSA experimental methods developed in Chapter 2 together with the Lekhnitskii's anisotropic elasticity solution in order to obtain the mixed-mode SIFs of a crack in orthotropic composites. Eccentrically loaded single-edge-notch tension (ESE(T)) specimens with four different material angles are investigated for the new mixed-mode SIFs. This investigation also examines a preferable region near the crack tip for the best least-squares fit in order to obtain the coefficients of the polynomial

expansions in Lekhnitskii's complex variable solution. Finite element simulations are carried out for the cracked composites. The VCCT computational method for energy release rate is also used from the FE solutions along with the FE direct strain field in order to compare with the TSA-calibrated strain fields.

Chapter 4 proposes a new stochastic S-N curve model utilizing Markov chain theory for composite laminates. The stochastic S-N curve can account for the variability from limited fatigue tests. Two stress levels are applied to a total of twenty-one S2-glass laminates in order to provide statistical data for the calibrations in the stochastic S-N curve model. The stiffness and TSA measurements are taken during the fatigue cycles until the serviceability failure when the specimen stiffness measured by an extensometer reduces to its 60% initial value. In addition to the fatigue experiments performed in this study, three available fatigue data sets of different E-glass composite laminates in the literature are also used to construct the stochastic S-N curves.

Finally, conclusions and future research follow in Chapter 5.

CHAPTER 2

NEW QUANTITATIVE THERMOELASTIC STRESS ANALYSIS TECHNIQUES

This chapter presents quantitative thermoelastic stress analysis techniques that can obtain the full-field sum of the in-plane strains in cyclically loaded composite materials using a highly sensitive infrared (IR) camera. This IR camera can detect the minute changes in temperature emitted from a surface in a solid material subjected to cyclic stresses. The changes in temperature are related to the applied stresses that can be transformed into strains. Therefore, the infrared signal acquired from the IR camera can be mapped into the strain field via experimentally calibrated constants. The proposed quantitative TSA techniques use one calibrated constant for composite materials with a transversely isotropic coat, whereas two constants are required for those without a transversely isotropic coat. Two composite material systems, pultruded materials and laminated composites, with different geometries, eccentrically loaded single-edge-notch tension (ESE(T)) and open-hole geometries, are investigated. The results obtained from quantitative TSA techniques are verified with finite element (FE) analyses and anisotropic elasticity solutions.

2.1 Proposed Derivations for Composite Materials with Transversely Isotropic and Orthotropic Surface Layer

The basis for quantitative TSA is formulated in this section by extending the work of Wong et al. (1987) and El-Hajjar and Haj-Ali (2003, 2004). The thermodynamic governing energy equation is written as:

$$Q_{i,i} = T\frac{\partial \sigma_{ij}}{\partial T}\dot{\varepsilon}_{ij} - \rho_0 C_\varepsilon \dot{T} + \rho_0 \dot{R} \tag{2.1}$$

where Q_i is the heat flux through the surface whose outward directed normal is n_i; T is the temperature; σ_{ij} is the stress tensor; $\dot{\varepsilon}_{ij}$ is the rate of strain tensor; ρ_0 is the mass density; C_ε is the specific heat coefficient at constant strain; $\dot{R}$ is the heat production rate of the internal heat sources per unit mass. Hooke's thermo-mechanical constitutive law for a linear anisotropic material is expressed as:

$$\sigma_{ij} = C_{ijkl}\left(\varepsilon_{kl} - \alpha_{kl}\left(T - T_0\right)\right) \tag{2.2}$$

where C_{ijkl} is the fourth rank tensor of the material constants; α_{kl} are the coefficients of thermal expansion; T is the current temperature; T_0 is the reference/initial temperature. If the thermo-mechanical material properties are assumed to remain constant with change in temperature, then the stress change with temperature is simply

$$\frac{d\sigma_{ij}}{dT} = -C_{ijkl}\alpha_{kl} \tag{2.3}$$

Combining Eqs. (2.1) and (2.3) and assuming adiabatic conditions with no internal heat sources ($Q_{i,i} = 0$, and $\dot{R} = 0$) yield:

$$\rho_0 C_\varepsilon \frac{\dot{T}}{T} = -C_{ijkl}\alpha_{kl}\dot{\varepsilon}_{ij} \tag{2.4}$$

Next, assuming small strain theory, and using the incremental form of Hooke's Law, Eq. (2.2), to express $C_{ijmn}d\varepsilon_{ij}$ in Eq. (2.4) yield:

$$\rho_0 C_\varepsilon \frac{dT}{T} = -\alpha_{kl}\left(d\sigma_{kl} + C_{klpq}\alpha_{pq}dT\right) \tag{2.5}$$

For the special case of an in-plane transversely isotropic coat top layer under a

state of plane stress, the in-plane material properties are equal: $\alpha_{11} = \alpha_{22} = \alpha$; $C_{11pq} = C_{22pq}$; $d\sigma_{33} = 0$. Using these conditions in Eq. (2.5), it can be seen that the thermoelastic effect is dependent only on the in-plane properties:

$$\left(\frac{\rho_0 C_\varepsilon}{T} + C_{klpq}\alpha_{mn}\alpha_{pq}\right)dT = -\left(\alpha_{11}d\sigma_{11} + \alpha_{22}d\sigma_{22}\right) = -\alpha\left(d\sigma_{11} + d\sigma_{22}\right) \tag{2.6}$$

The general stress-strain relation for the in-plane isotropic coat is:

$$\begin{Bmatrix}\sigma_{11}\\ \sigma_{22}\\ \sigma_{33}\\ \tau_{23}\\ \tau_{13}\\ \tau_{12}\end{Bmatrix} = \begin{bmatrix} C_{11} & C_{12} & C_{13} & 0 & 0 & 0 \\ C_{12} & C_{11} & C_{13} & 0 & 0 & 0 \\ C_{13} & C_{13} & C_{33} & 0 & 0 & 0 \\ 0 & 0 & 0 & C_{44} & 0 & 0 \\ 0 & 0 & 0 & 0 & C_{44} & 0 \\ 0 & 0 & 0 & 0 & 0 & \left(C_{11} - C_{12}\right)/2 \end{bmatrix} \begin{Bmatrix}\varepsilon_{11}\\ \varepsilon_{22}\\ \varepsilon_{33}\\ \gamma_{23}\\ \gamma_{13}\\ \gamma_{12}\end{Bmatrix} \tag{2.7}$$

The plane stress assumption in this coat layer enables expressing the out-of-plane strain ε_{33} in terms of the in-plane strain components:

$$\varepsilon_{33} = -\frac{C_{13}}{C_{33}}\varepsilon_{\alpha\alpha} \quad , \quad \alpha = 1, 2 \tag{2.8}$$

Therefore, the first stress invariant can be expressed as:

$$\Delta\sigma = \sigma_{\alpha\alpha} = \sigma_{11} + \sigma_{22} = \frac{\left(C_{11}C_{33} + C_{12}C_{33} - 2C_{13}{}^2\right)}{C_{33}}\left(\varepsilon_{11} + \varepsilon_{22}\right) \tag{2.9}$$

From an experimental perspective, the infrared detector measures an un-calibrated TSA signal, *S*, that is linearly related to the radiant photons emitted due to a surface temperature change ($S \propto \Delta T / T \propto \Delta\sigma$). Equation (2.6) can be used to relate the TSA signal to the incremental change of the first stress invariant through a parameter, k_σ :

$$\Delta\sigma = k_\sigma S \tag{2.10}$$

Substituting Eq. (2.9) into (2.10) yields:

$$\frac{\left(C_{11}C_{33}+C_{12}C_{33}-2C_{13}^{\ 2}\right)}{C_{33}}\left(\Delta\varepsilon_{11}+\Delta\varepsilon_{22}\right)=k_{\sigma}S \tag{2.11}$$

Next, the above elastic constants of the surface layer are used to relate the TSA signal to the in-plane strains instead of the stress invariant. This is important since all orthotropic layers have the same in-plane strains in a medium subjected to in-plane loading. A new constant, k_{ε}, can then be defined as:

$$k_{\varepsilon}=\frac{C_{33}}{(C_{11}C_{33}+C_{12}C_{33}-2C_{13}^{\ 2})}k_{\sigma} \tag{2.12}$$

This enables formulating a new thermoelastic equation, similar to Eq. (2.10), in terms of the in-plane strains using the new relationship:

$$\Delta\varepsilon_{\alpha\alpha}=k_{\varepsilon}\cdot S \quad , \quad \alpha=1,2 \tag{2.13}$$

For a composite material with an orthotropic top surface and no coat, Eq. (2.6) cannot be used (i.e., no scalar relation exists between the sum of stresses and the temperature gradients). Two separate material coefficients are now needed. Therefore, Eq. (2.6) can be rewritten for an orthotropic case in the form:

$$dT=A_1\cdot d\sigma_{11}+A_2\cdot d\sigma_{22} \tag{2.14}$$

In order to calibrate the above two constants, the stresses can be replaced by strains.

$$dT=A_1\cdot d\left(C_{11}\varepsilon_{11}+C_{12}\varepsilon_{22}+C_{13}\varepsilon_{33}\right)+A_2\cdot d\left(C_{12}\varepsilon_{11}+C_{22}\varepsilon_{22}+C_{23}\varepsilon_{33}\right) \tag{2.15}$$

where the C_{ij} is the material orthotropic stiffness. Imposing a state of plane stress state, the stress-strain relations of an orthotropic material can be expressed as:

$$\begin{Bmatrix}\sigma_{11}\\ \sigma_{22}\\ \tau_{12}\end{Bmatrix}=\begin{bmatrix}Q_{11} & Q_{12} & 0\\ Q_{12} & Q_{22} & 0\\ 0 & 0 & Q_{66}\end{bmatrix}\begin{Bmatrix}\varepsilon_{11}\\ \varepsilon_{22}\\ \gamma_{12}\end{Bmatrix} \tag{2.16}$$

The out-of-plane strain ε_{33} can be expressed as:

$$\varepsilon_{33} = -\frac{\nu_{13}}{E_{11}}\sigma_{11} - \frac{\nu_{23}}{E_{22}}\sigma_{22} = -\left(\frac{\nu_{13}}{E_{11}}Q_{11} + \frac{\nu_{23}}{E_{22}}Q_{12}\right)\varepsilon_{11} - \left(\frac{\nu_{13}}{E_{11}}Q_{12} + \frac{\nu_{23}}{E_{22}}Q_{22}\right)\varepsilon_{22} \tag{2.17}$$

Therefore,

$$\varepsilon_{33} = B_1\varepsilon_{11} + B_2\varepsilon_{22}; \quad B_1 = -\left(\frac{\nu_{13} + \nu_{12}\nu_{23}}{1 - \nu_{12}\nu_{21}}\right); \quad B_2 = -\left(\frac{\nu_{13}\nu_{21} + \nu_{23}}{1 - \nu_{12}\nu_{21}}\right) \tag{2.18}$$

Substituting Eq. (2.18) into Eq. (2.15) yields:

$$dT \equiv S = H_1 \cdot d\varepsilon_{11} + H_2 \cdot d\varepsilon_{22} \tag{2.19}$$

where

$$H_1 = \left(A_1 \cdot C_{11} + A_2 \cdot C_{12} + A_1 \cdot B_1 \cdot C_{13} + A_2 \cdot B_1 \cdot C_{23}\right) \tag{2.20a}$$

$$H_2 = \left(A_1 \cdot C_{12} + A_2 \cdot C_{22} + A_1 \cdot B_2 \cdot C_{13} + A_2 \cdot B_2 \cdot C_{23}\right) \tag{2.20b}$$

Equation (2.19) implies that one can calibrate the coefficients, H_1 and H_2, separately and apply superposition, assuming the material lies in the linear range.

Figure 2.1 shows a schematic of calibration curve of unidirectional specimens. In the case of 0° material angle, Eq. (2.19) can be expressed in terms direct strains:

$$S = \left(H_1 - \nu_{21}H_2\right) \cdot d\varepsilon_{11} = k_1 \cdot d\varepsilon_{11} \tag{2.21a}$$

Likewise, in the case of 90° material angle,

$$S = \left(-\nu_{12}H_1 + H_2\right) \cdot d\varepsilon_{22} = k_2 \cdot d\varepsilon_{22} \tag{2.21b}$$

Solving Eq. (2.21) yields:

$$H_1 = \frac{\nu_{21}k_2 + k_1}{1 - \nu_{12}\nu_{21}} \tag{2.22a}$$

$$H_2 = \frac{k_2 + \nu_{12}k_1}{1 - \nu_{12}\nu_{21}} \tag{2.22b}$$

where k_1 and k_2 are the slope of experimental calibration curves as shown in Fig. 2.1. For a general plane stress case, the TSA signal can be expressed as the general case in Eq. (2.19).

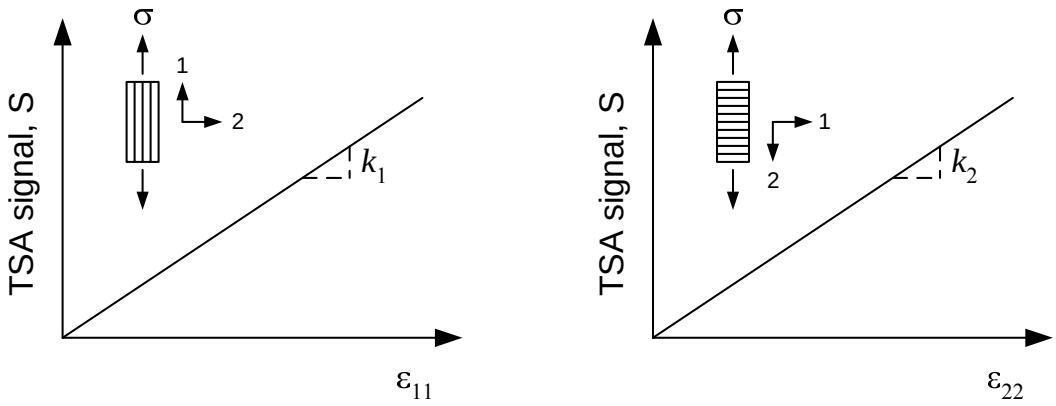

(a) Uniaxial case of 0 degree (b) Uniaxial case of 90 degree

Fig. 2.1. Schematics for thermo-mechanical calibration curves of the TSA coefficients in a unidirectional specimen

2.2 Composites Calibrations for Homogeneous Straight Coupons with and without Coated Layers

Two composite materials are investigated for the quantitative TSA techniques. The first is thick-section E-glass/polyester pultruded composite with a transversely isotropic layer. This pultruded composite material consists of polyester layers reinforced with E-glass unidirectional roving and continuous filament mats (CFM). The cross-section of the pultruded composite material is shown in Fig. 2.2.

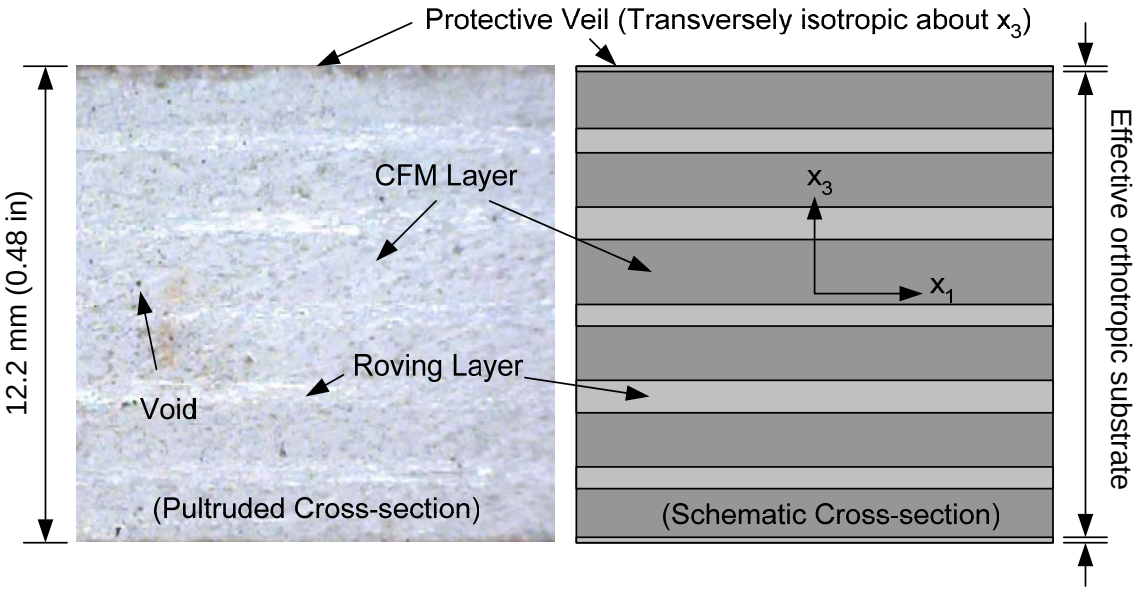

Fig. 2.2. Cross-section of E-glass/polyester pultruded composite

The surface coating (veil) are normally added to the pultruded composites. This surface coat can provide surface smoothing and resistance to environmental hazards, such as corrosion and inadvertent handling. The most commonly used materials for the surface finishing are A-glass/polyester or pure polyester resin veils (Creative Pultrusions, 2000). The short fibers on the coating layer are randomly oriented in the plane. Therefore, this surface layer is transversely isotropic, and one thermo-mechanical constant, k_ε in Eq. (2.13), is required to calibrate the sum of in-plane strain field via infrared signal.

Another composite material system for investigation is S2-glass/E773FR composite laminates with a $[0_5/90/0_5]$ lay-up sequence. The composite laminates used in this study are manufactured in-house using vacuum bagging and autoclave. The lay-up sequence of the laminates provides an orthotropic property and no surface coat is applied. Therefore, two thermo-mechanical constants, H_1 and H_2 in Eq. (2.19), are required to map the infrared signal into the sum of in-plane strain field. Note the added 90° layer is inserted in the mid-layer in order to provide for stiffness normal to the 0° fibers. This

prevents early cracking in the matrix especially for the cases where the loading is normal to the 0° layers. Figures 2.3 and 2.4 show the actual cross-section and schematic lay-up configuration of the tested S2-glass/E773FR composite laminate, respectively.

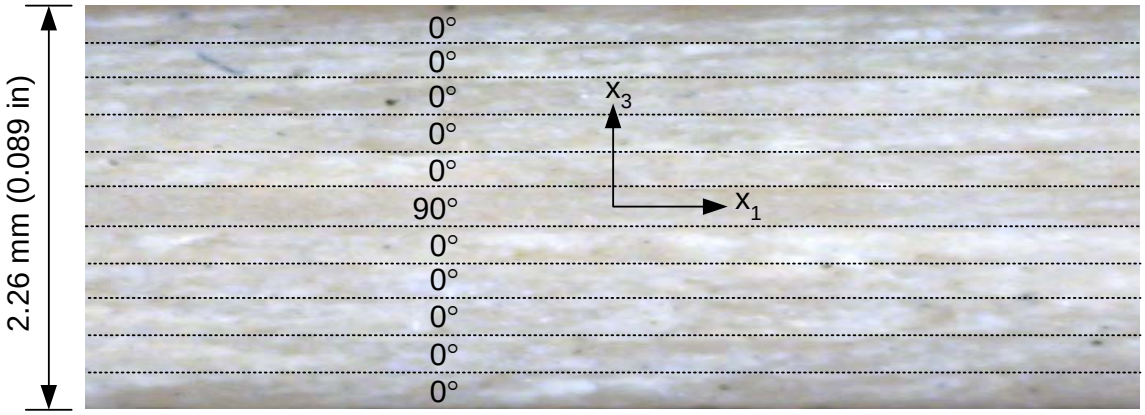

Fig. 2.3. Cross-section of S2-glass/E773FR composite laminate

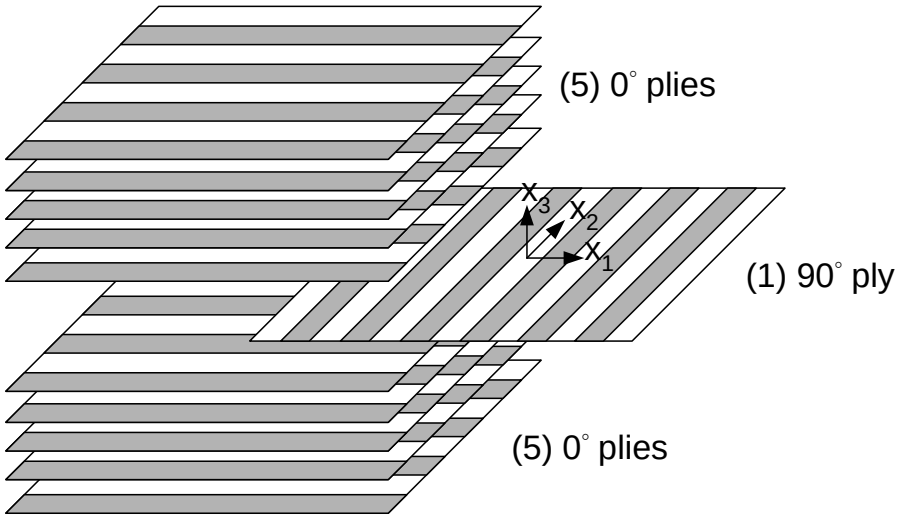

Fig. 2.4. Schematic lay-up configuration of S2-glass/E773FR composite laminate

A DeltaTherm DT1500 IR camera is used to acquire the full-field thermal measurements in this study. This DT1500 IR camera uses 320×256 staring photon detector arrays to detect the thermal emissivity with a resolution of less than 10mK. Those photon detectors require cooling by liquid nitrogen in order to achieve this resolution. The Del-

taTherm's photon array detectors synchronize with the applied cyclic loading with a sufficient frequency to maintain the adiabatic state in the tested material. Only the thermal emissivity that responds to the applied frequency will be integrated. Therefore, the applied cyclic loading can not only avoid the transient thermoelastic effect but also reject any non-relevant thermal emissivity from the background. Figure 2.5 shows the testing setup along with a schematic of the TSA data acquisition.

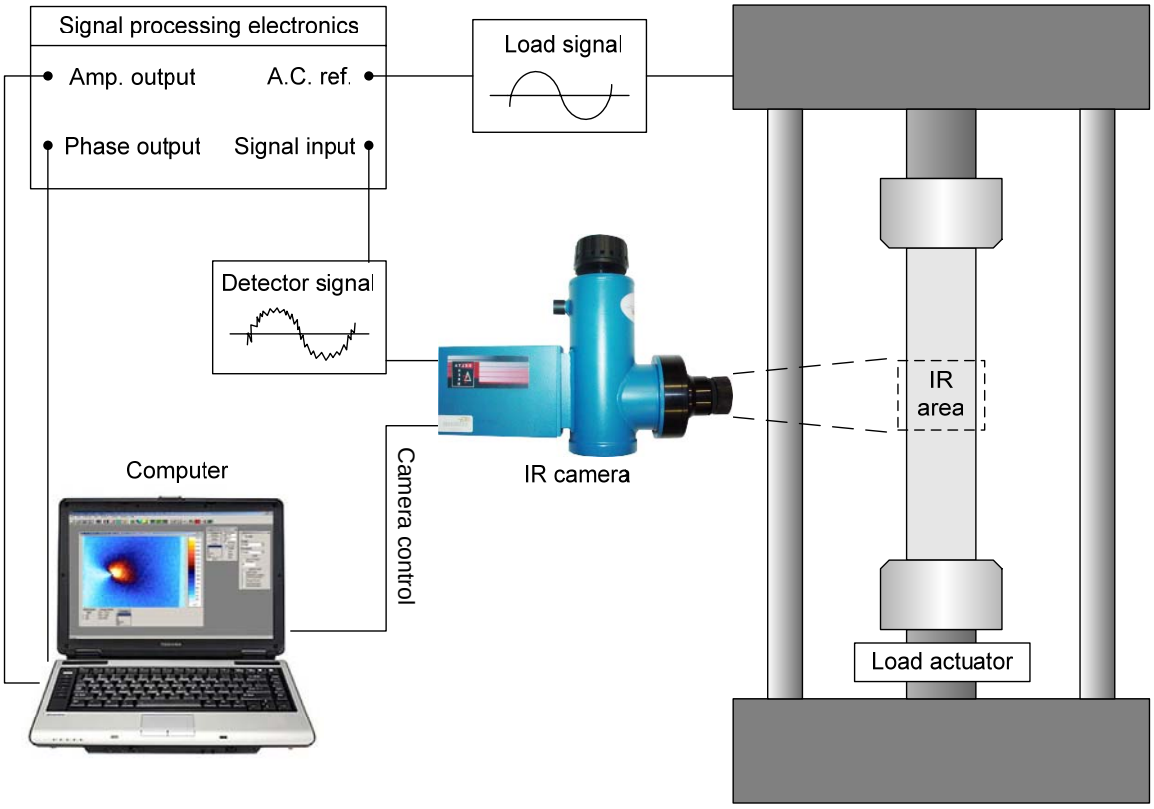

Fig. 2.5. Schematic of a typical TSA experimental setup

The cyclic loading is applied using an MTS 810 servo-hydraulic test system with a 22.2 kN (50 kip) capacity. The resolution accuracy of the recorded strains is within 50 micro-strain and the loading is within 0.22 kN (50lb). The tested specimens are coated with black paint (Krylon Ultra Flat) to improve the surface emissivity. The strains are

assumed the same through the thickness of the specimen because of the symmetry and material continuity. Therefore, biaxial strain gauges or orthogonal uni-axial strain gauges mounted on the backside of the specimen can be used to correlate with the IR signal on the camera side. The IR camera was synchronized with the cyclic loading that is applied by the MTS 810 servo-hydraulic system. The reference signal provided by the MTS synchronized the peaks of the loading with the maximum or minimum material response using the TSA post processing software. A sine function cyclic loading was applied to the specimens at a frequency of 5 Hz. This frequency is shown later in this study to map the average TSA response with relatively more accuracy compared to other higher range frequencies. Figure 2.6 illustrates the IR camera observing the infrared emissivity from the front surface of a straight coupon with uni-axial strain gauges mounted on the backside.

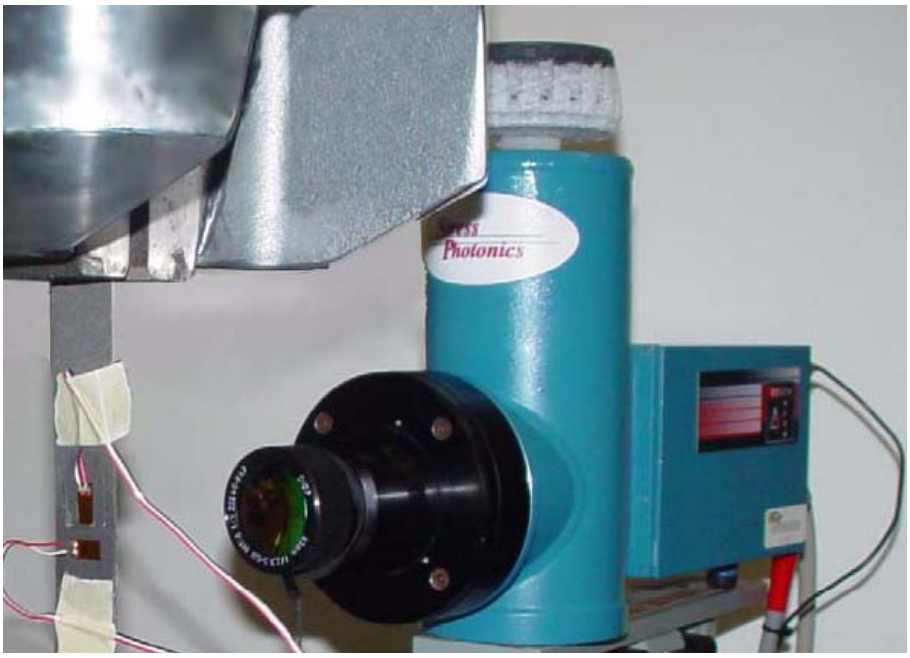

Fig. 2.6. Thermo-mechanical constant calibration using a straight coupon observed by an IR camera

The proposed quantitative TSA method is calibrated for E-glass/polyester pultruded composites and S2-glass/E773FR composite laminates. The in-plane elastic properties for E-glass/polyester pultruded composites are taken from El-Hajjar and Haj-Ali (2003). The S2-glass/E773FR coupons were cut from a monolithic plate and tested with the tensile load applied parallel and transverse to the major stiffness axis. The S2-glass/E773FR coupons are 25.4 mm (1 inch) wide with a 152.4 mm (6 inches) un-gripped length. A uniform thickness of 2.26 mm (0.089 inches) is achieved for the $[0_5/90/0_5]$ laminate system using an autoclave. Biaxial strain gages were oriented in the material directions to measure the surface strains in order to account for the Poisson's effect. The TSA effect was calibrated in the 0.25% strain range to ensure the materials remain linear elastic. The in-plane elastic properties and the ultimate tensile stresses of the pultruded composites and tested S2-glass/E773FR coupons are listed in Table 2.1.

Table 2.1. Tested composite in-plane material properties and tensile strength

	E_{11}	E_{22}	G_{12}	ν_{12}	ν_{21}	σ_{uts} (axial)	σ_{uts} (transverse)
	ksi (GPa)					ksi (GPa)	
E-glass/polyester (El-Hajjar and Haj-Ali, 2003)	1,444 (10)	2,484 (17.1)	507 (3.5)	0.217	0.283	27 (0.186)	12 (0.083)
S2-glass/E773FR	2,830 (20)	7,127 (49.2)	1,976 (13.6)	0.084	0.222	186 (1.283)	23 (0.159)

The TSA thermo-mechanical coefficients are then calibrated using the proposed methods for uniform (homogeneous) coupons. Figure 2.7 shows the TSA calibration curve which expresses the average TSA signal over the mid-section of a uniform E-glass/polyester pultruded composite sample under uniaxial loading. This average TSA signal is plotted against the sum of in-plane strains measured from two uniaxial strain

gauges placed on the back of the specimen, and the thermal response can be related to the sum of in-plane strains by one thermo-mechanical coefficient. The thermo-mechanical coefficient of the tested pultruded composites is 51,443 camera-units/in/in. Once the coefficient is known, one can map the IR images to the sum of in-plane strain fields.

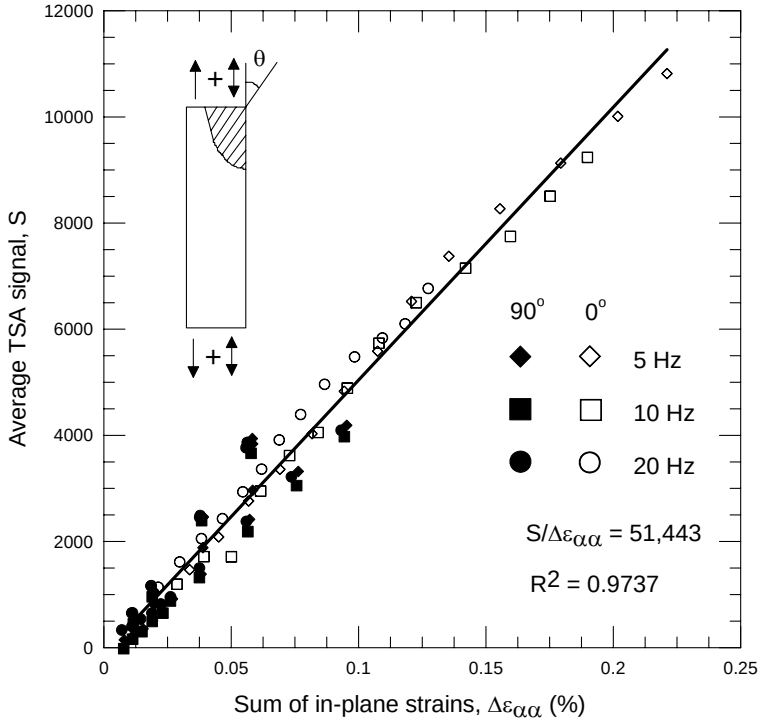

Fig. 2.7. Thermo-mechanical TSA coefficient calibration for E-glass/polyester pultruded coupon

Figure 2.8 shows the TSA calibration curve of the S2-glass/E773FR laminate. The calibration procedure outlined previously is repeated here for the S2-glass/E773FR laminate. It can be seen that the 0° and 90° calibrations have different thermo-mechanical coefficients due to the material orthotropy of the surface layer. The thermo-mechanical coefficient of the 0° and 90° material direction were 29,624 and 88,669 camera-unit/in/in, respectively. More experimental data points (values of average surface strains) are gener-

ated for the 0° plate orientation due to its stiffness and lack of damage. The noise in the calibration experiments could be due to several reasons such as the variability of manufacture processes, specimen alignment, and IR camera positioning. It is also interesting to note that a wider scatter exists in the transverse pultruded measurements compared to the axial direction. This can be explained due to the lower fiber volume fraction (less than 40%) which adds nonlinear effects on relatively lower strains. In addition, cracks are exited in the tensile transverse modes. The lower scatter in the S2-glass/E773FR composites is attributed to the high fiber volume fraction (around 60%) and the advanced autoclave manufacturing.

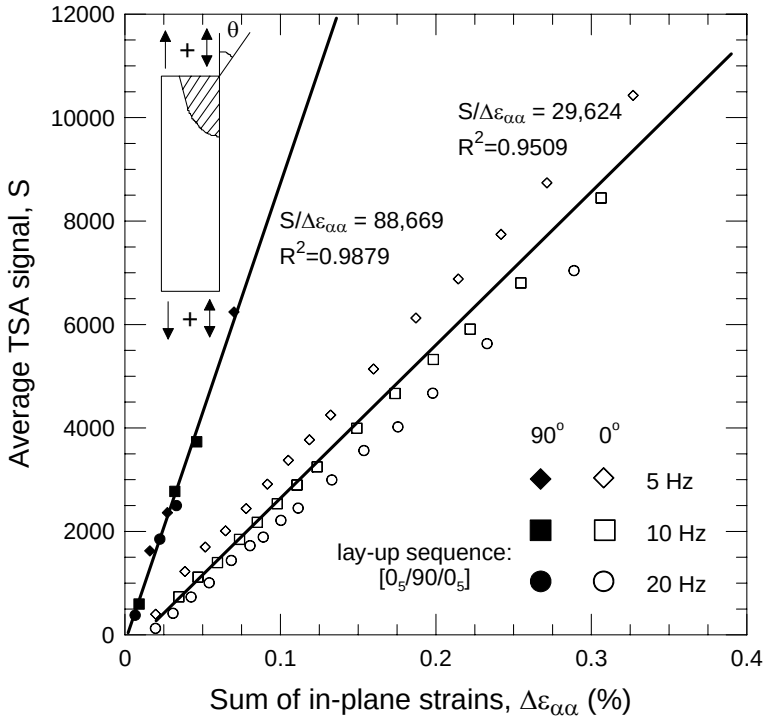

Fig. 2.8. Thermo-mechanical coefficient calibration for S2-glass/E773FR laminate

2.3 Full-field TSA Experiments and FE Verifications for ESE(T) Composites with and without Coated Layers

This study applies an ESE(T) FE fracture geometry, shown in Fig. 2.9, to verify the proposed quantitative TSA techniques for the pultruded composites and S2-glass/E773FR laminates. The length and width of the specimens were 10 and 2.5 inches, respectively. The thickness of the pultruded and laminate composites are 0.48 and 0.089 inches, respectively. The notch length was 0.75 inches ($a/W = 0.3$). The notch is created by a diamond edge saw blade with a thickness of 0.025 inches. The root radius is 0.0086 inches shown in Fig. 2.9.

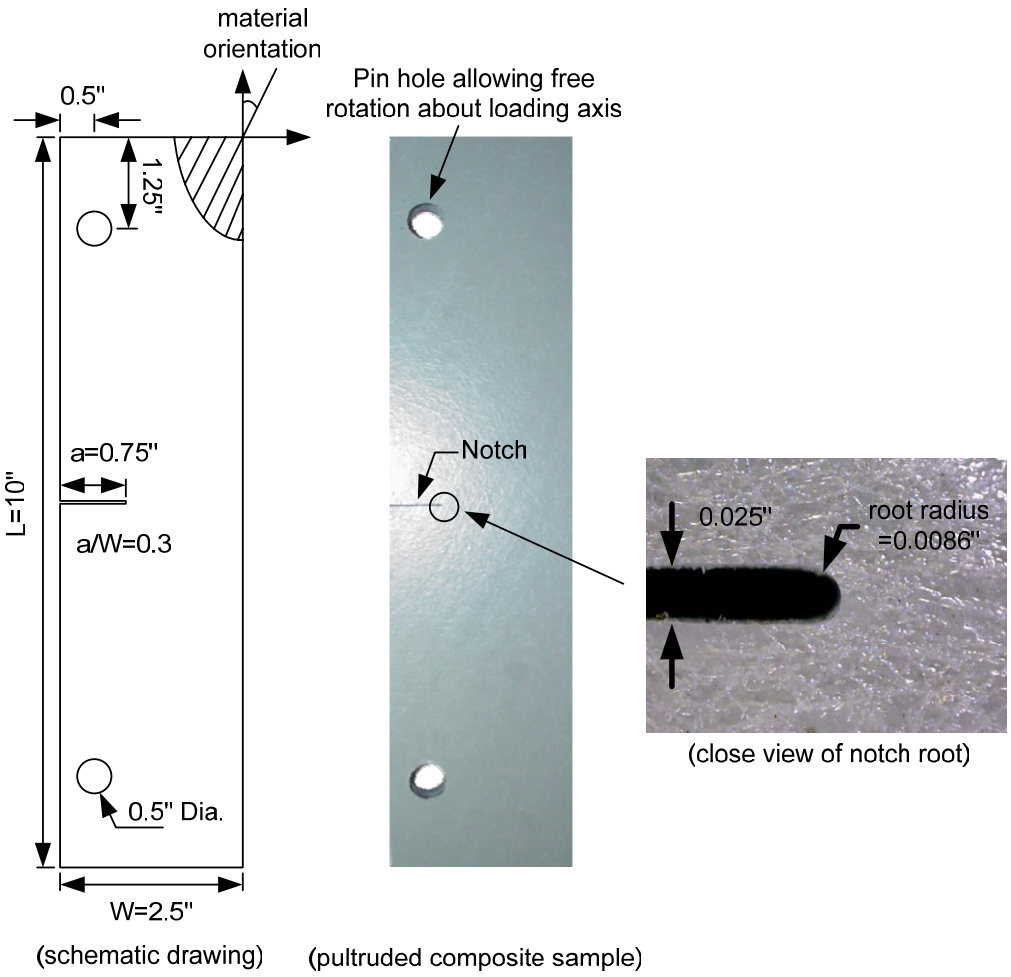

Fig. 2.9. The ESE(T) composite specimen and its dimensions

The experimental setup included the DeltaTherm DT1500 IR camera, shown in Fig. 2.10, used to take full-field IR images. Each image was taken from frames integrated from captured TSA signal over one minute duration. The ESE(T) specimen is subjected to a tension-tension cyclic loading of 5 Hz, and this frequency is synchronized with IR camera to match the maximum and minimum material response. The ESE(T) specimen is also coated with flat black paint to improve the surface emissivity as described previously.

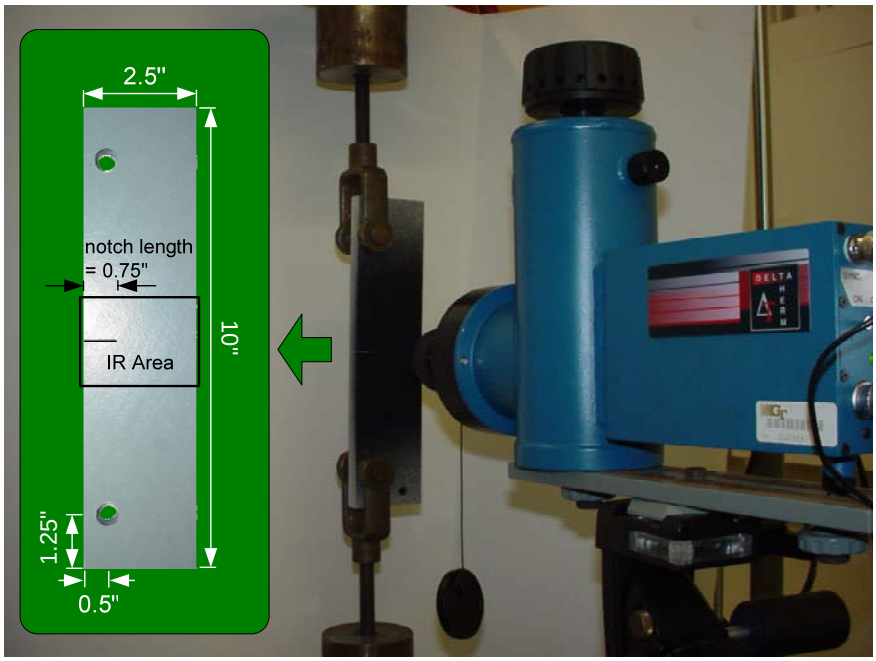

Fig. 2.10. Experiment setup of an infrared camera and ESE(T) pultruded composite specimen

In order to verify the accuracy of the calibrated thermo-mechanical constant, an ABAQUS general purpose FE model, shown in Fig. 2.11, is generated to simulate the strain field of the tested composite specimens. The FE model uses 8-node continuum plane stress elements (CPS8R) and has 10,754 elements. The elements in the crack tip

vicinity are finely meshed as 0.01×0.01 square inches per element in order to account for the stress singularity in the crack tip. The selected size of the finely-meshed region is 0.8×0.8 square inches. The area around the crack tip is finely meshed in a uniform fashion in order to allow comparing the Lekhnitskii's expansion solution around the crack tip using the least-squares method to calibrate the coefficients. These refined meshes can provide considerable strain values (around 3,000 nodes) for the least-squares method. The specialized singular FE meshes are not used because a sharp crack tip is assume and may not provide enough strain values for the least-squares fit. This element size is selected based on a parametric study for stress intensity factors discussed in Chapter 3.

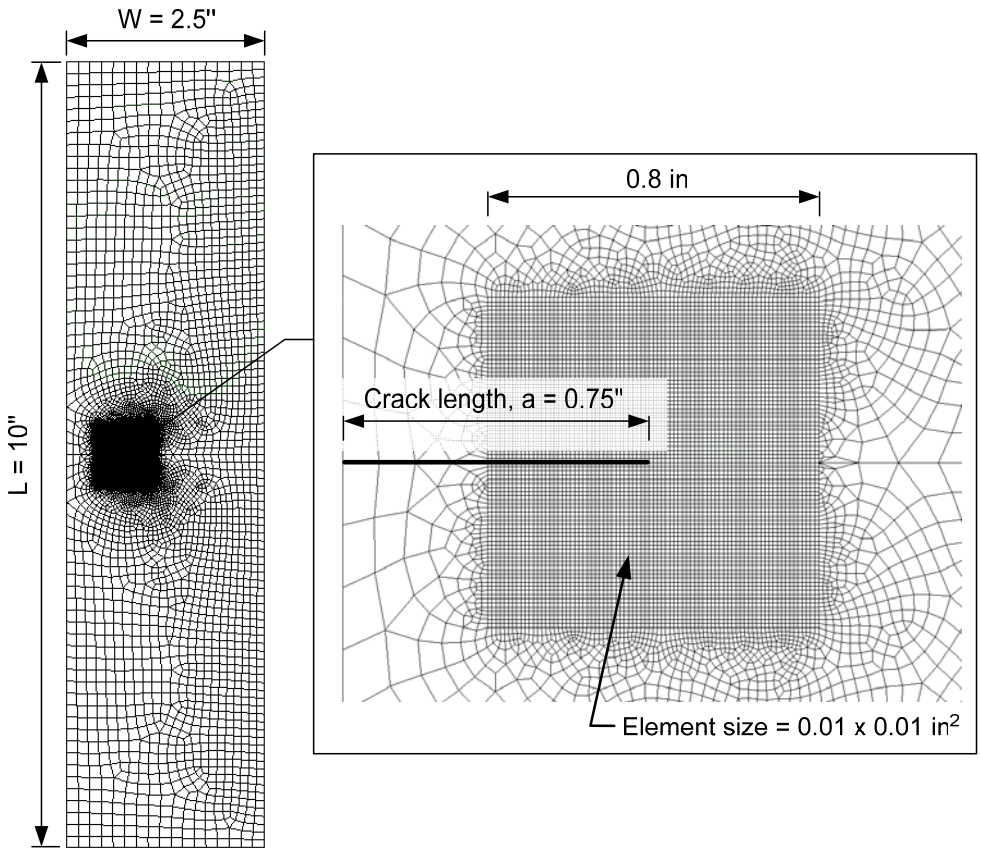

Fig. 2.11. Finite element mesh and geometry of single-edge-notch fractured specimens

The calibration for E-glass/polyester pultruded composites is first verified. The thermo-mechanical coefficient, 51,443 camera-units/in/in, calibrated in Section 2.2 is employed. Then the infrared signal from the TSA techniques can be transformed into the sum of in-plane strains using the relationship described in Eq. 2.13. The ESE(T) specimens are subjected to a stress amplitude of 0.5 ksi to ensure the materials remain in linear elastic range. Figures 2.12 and 2.13 illustrate the FE simulations and the ESE(T) composite specimens loaded axially and transversely to the major stiffness axis. Good agreement is shown between the experimental and FE sum of in-plane strains along the *x* and *y* directions.

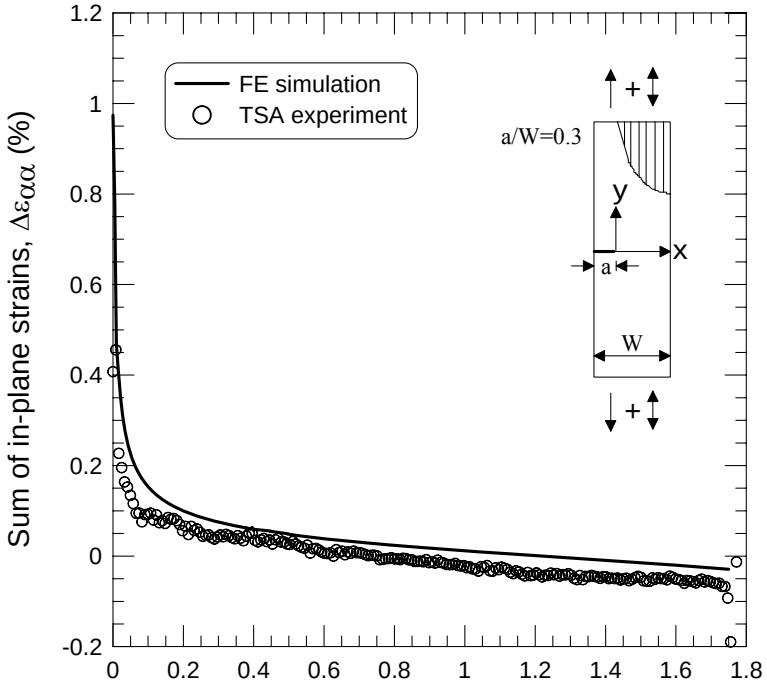

(a) Line interrogation along x-axis

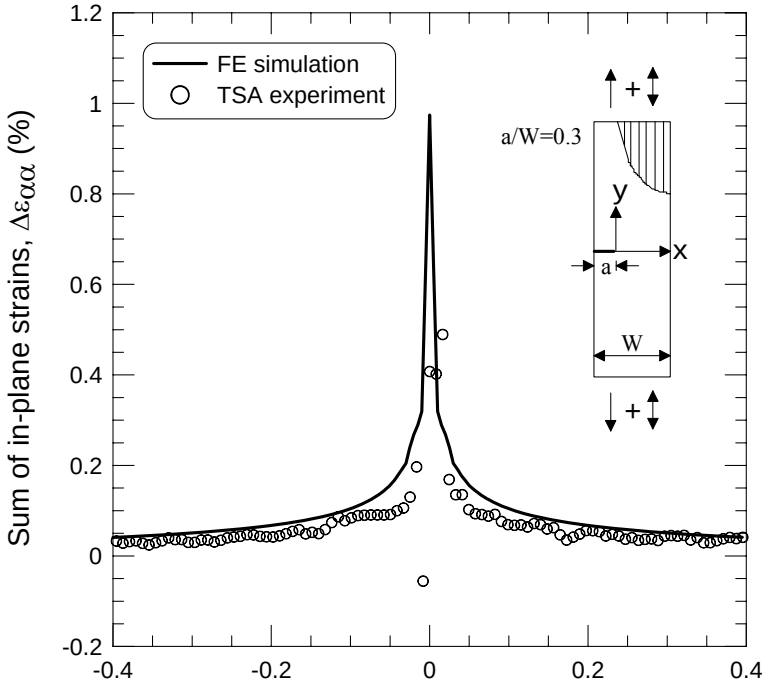

(b) Line interrogation along y-axis

Fig. 2.12. Line interrogation of ESE(T) geometry for 0° material angle E-glass/polyester thick-section pultruded coupon

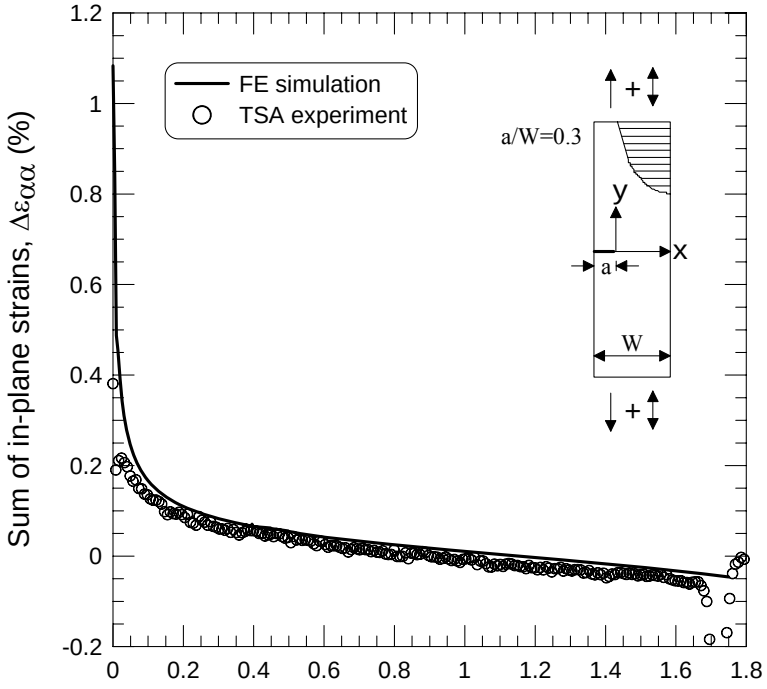

(a) Line interrogation along x-axis

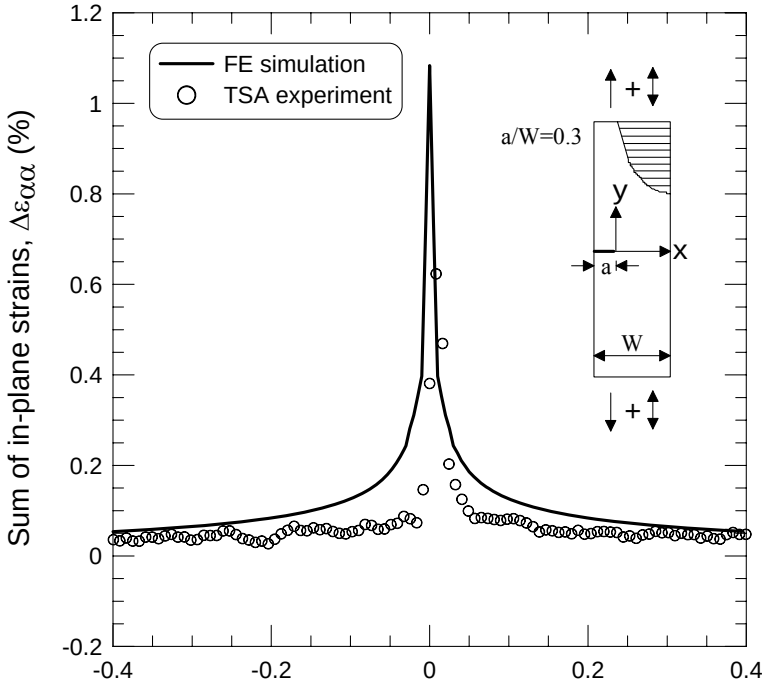

(b) Line interrogation along y-axis

Fig. 2.13. Line interrogation of ESE(T) geometry for 90° material angle E-glass/polyester thick-section pultruded coupon

Four E-glass/polyester pultruded composite samples are cut from their monolithic plates with four different fiber orientations (0°, 30°, 45°, and 90°) with respect to the loading direction. These orientations are used in order to verify the calibrations for materials with and without the transversely isotropic coat. These samples with different fiber orientations will be also used for generating different material anisotropy and coupling in the mixed-mode SIFs. Figure 2.14 shows the contours of TSA images with 320×256 pixels taken for four different off-axis material orientations of fractured pultruded composites. The direct TSA test results show relatively wide scatters and are not smooth. This is expected, and a typical representation of the many sources of noise or error is presented. The TSA results from the integrated IR images can be reported as one integrated and averaged values for each pixel. This "raw" test image result was then smoothed and presented with less discontinuity in 2-D contour plots. The smooth method using a simple averaging technique which a continuous value is generated by a weighted average of pixel values from the nearest 3×3 pixels array in the original images (Surfer 7, 1999). Figures 2.15 to 2.18 show the smoothed TSA strain invariant compared with the corresponding FE models. Good correlations are shown between the FE sum of in-plane strains and those obtained from the TSA measurements.

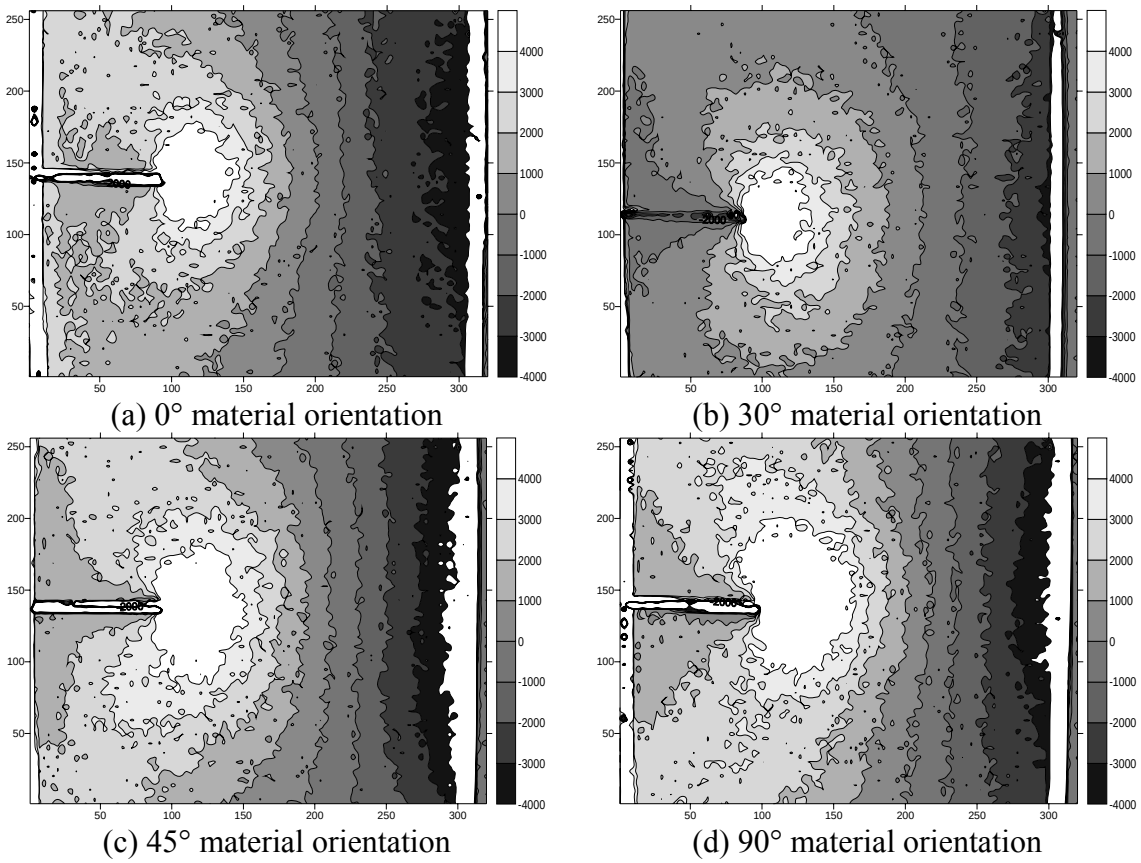

Fig. 2.14. Thermographic integrated test images (320×256 pixels) with different material orientations of E-glass/polyester pultruded composites (without smoothing)

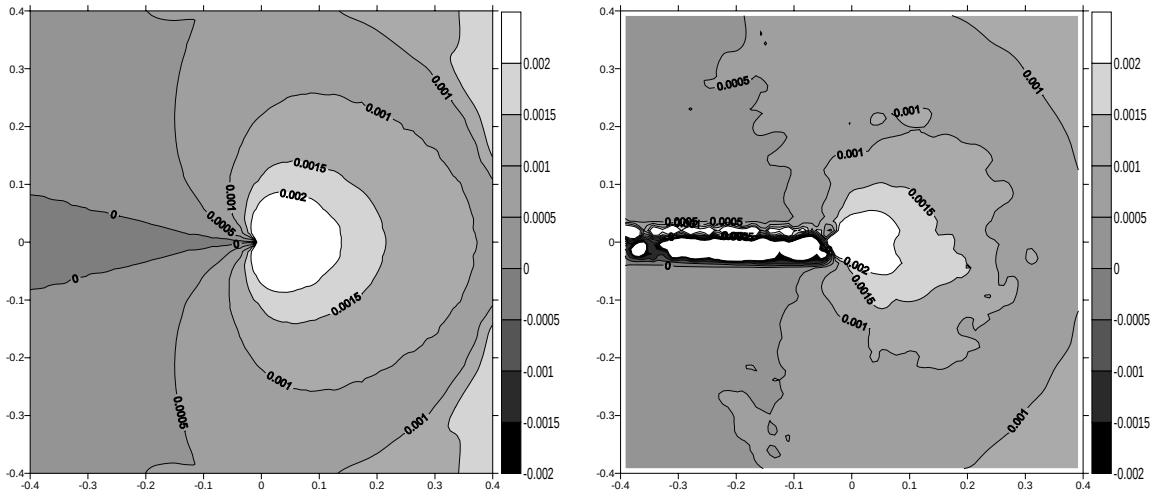

(a) Finite element simulation (b) Smoothed experimental TSA signal

Fig. 2.15. Contours of finite element simulations and TSA experiments of a fractured E-glass/polyester ESE(T) pultruded composites with 0° material orientation (dimensions are in inches)

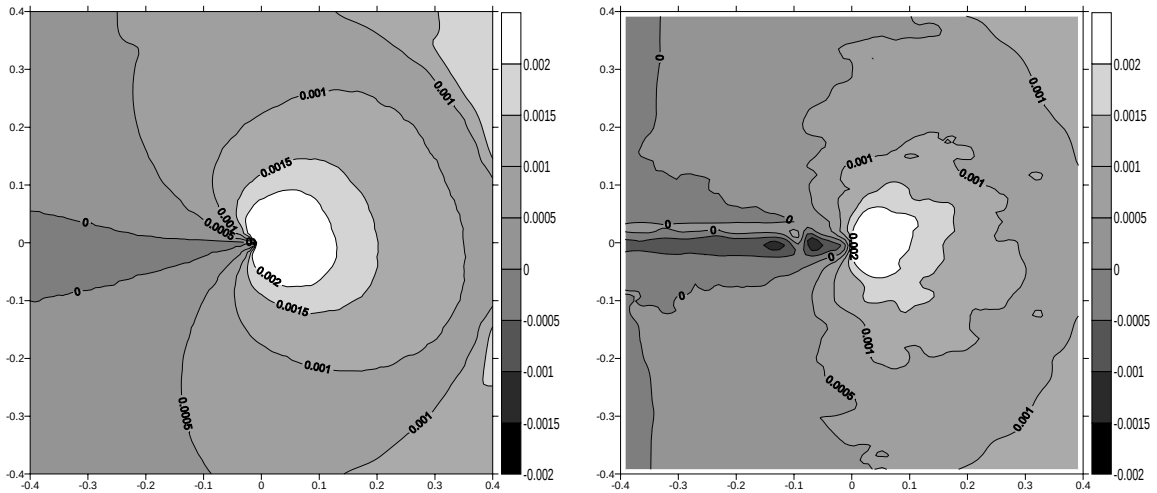

(a) Finite element simulation (b) Smoothed experimental TSA signal

Fig. 2.16. Contours of finite element simulations and TSA experiments of a fractured E-glass/polyester ESE(T) pultruded composites with 30° material orientation (dimensions are in inches)

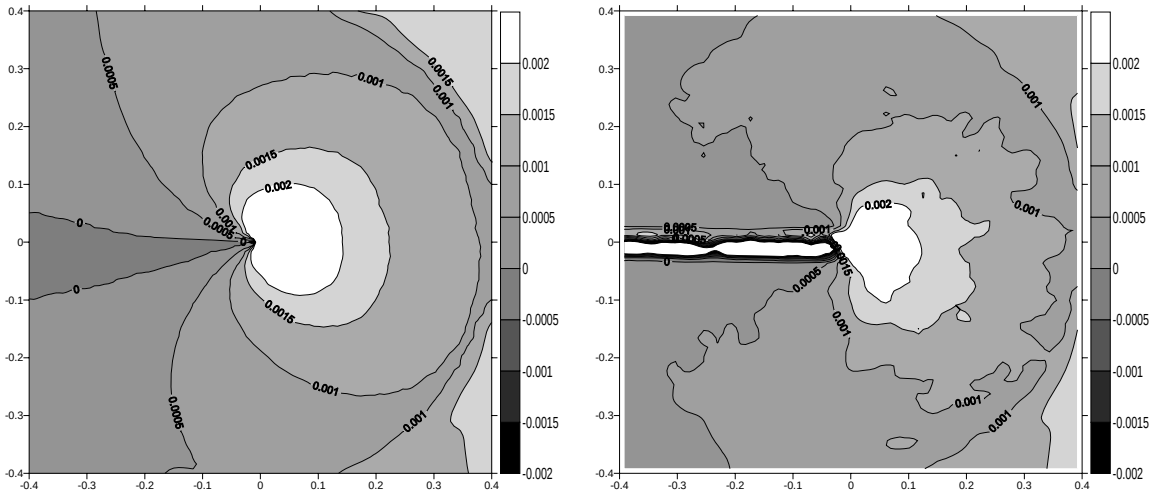

(a) Finite element simulation (b) Smoothed experimental TSA signal

Fig. 2.17. Contours of finite element simulations and TSA experiments of a fractured E-glass/polyester ESE(T) pultruded composites with 45° material orientation (dimensions are in inches)

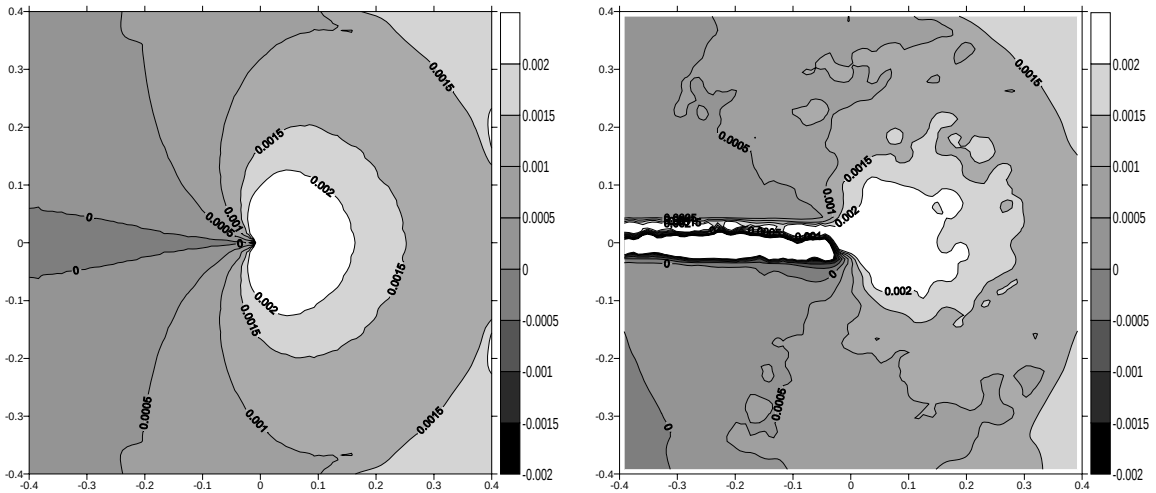

(a) Finite element simulation (b) Smoothed experimental TSA signal

Fig. 2.18. Contours of finite element simulations and TSA experiments of a fractured E-glass/polyester ESE(T) pultruded composites with 90° material orientation (dimensions are in inches)

The uncoated S2-glass/E773FR fractured laminates are also cut from their monolithic plate with four material orientations (0°, 30°, 45°, and 90°) with respect to the loading direction. The uncoated S2-glass/E773FR laminates use the two thermo-mechanical coefficients calibrated in Section 2.2 due to the material anisotropy. In order to verify the calibration coefficients, the FE simulations were performed to generate the strain fields and then converted to an equivalent TSA signal in the fractured specimens. The simulated infrared signal is calculated via the summation of the individual multiplication of the direct strains obtained from the FE models and the two calibrated thermo-mechanical constants. This calculation can be implemented using Eq. 2.19. The comparisons between the simulated infrared signal and the smoothed experimental TSA results are shown in Figs. 2.19 to 2.22.

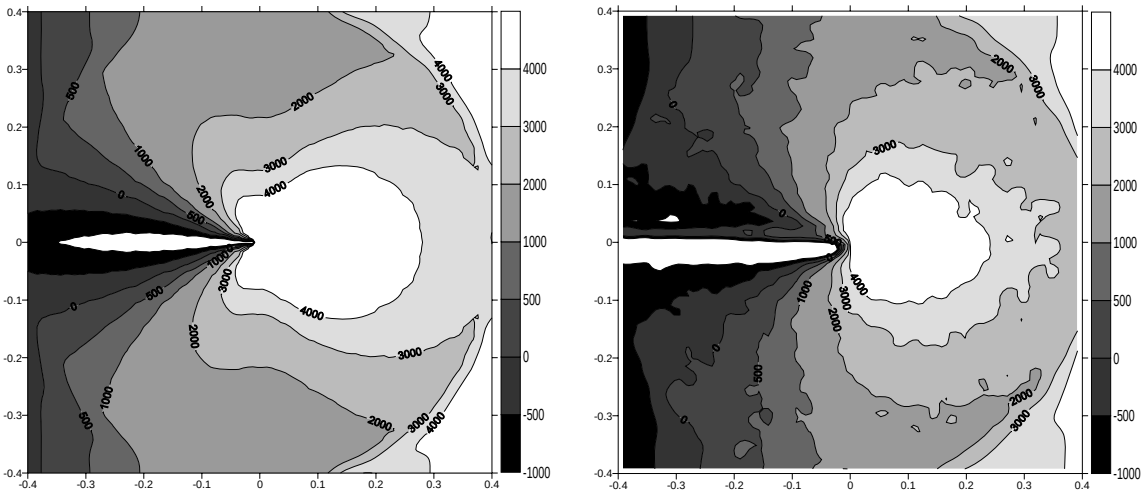

(a) Finite element simulation (b) Smoothed experimental TSA signal

Fig.2.19. Contours of finite element simulations and TSA experiments of S2-glass/E773FR ESE(T) laminates with 0° material orientation (dimensions are in inches)

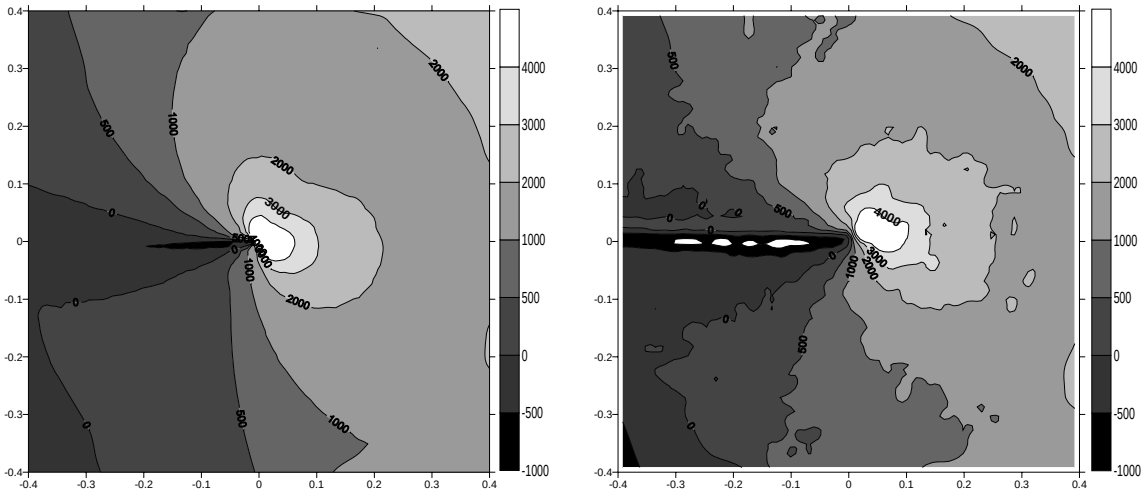

(a) Finite element simulation (b) Smoothed experimental TSA signal

Fig.2.20. Contours of finite element simulations and TSA experiments of S2-glass/E773FR ESE(T) laminates with 30° material orientation (dimensions are in inches)

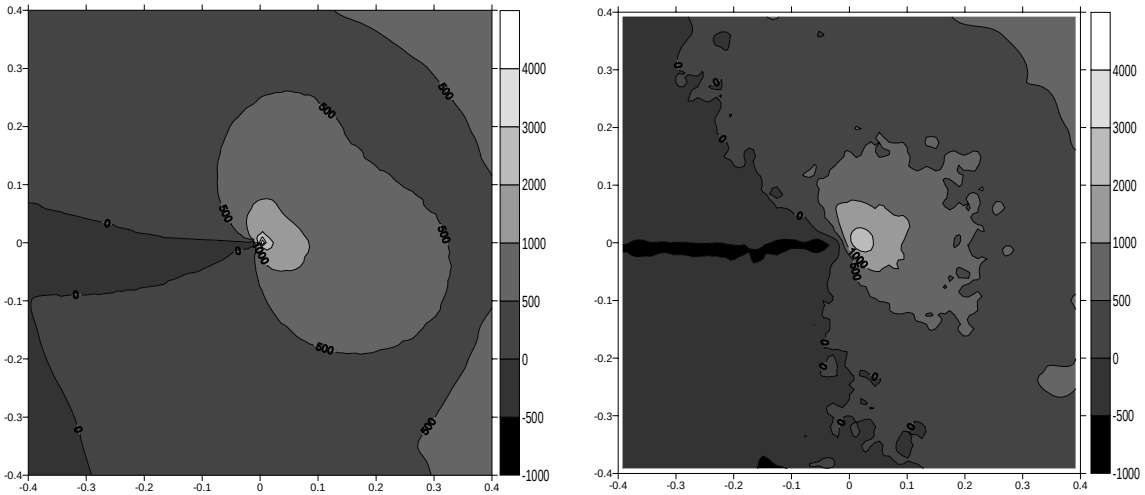

(a) Finite element simulation (b) Smoothed experimental TSA signal

Fig.2.21. Contours of finite element simulations and TSA experiments of S2-glass/E773FR ESE(T) laminates with 45° material orientation (dimensions are in inches)

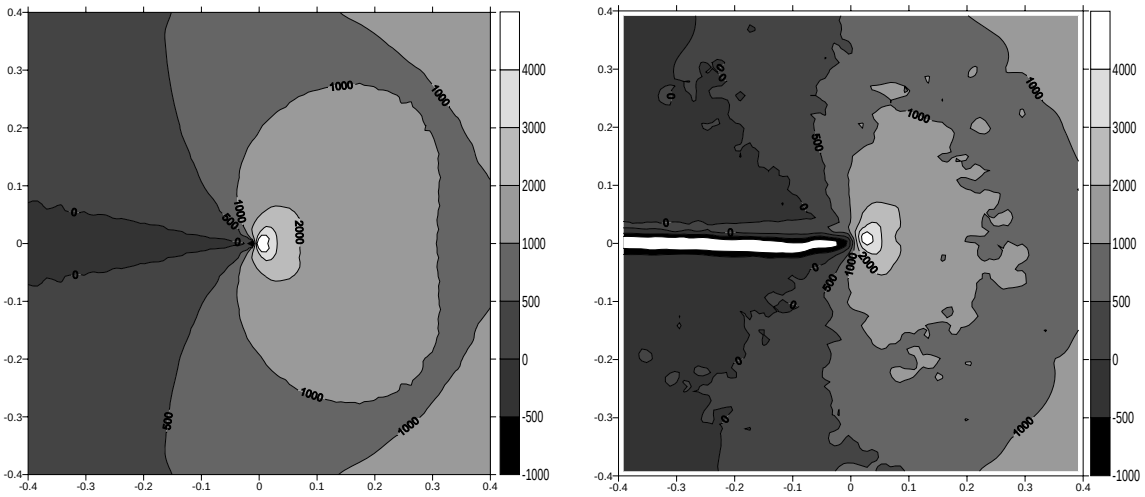

(a) Finite element simulation (b) Smoothed experimental TSA signal

Fig.2.22. Contours of finite element simulations and TSA experiments of S2-glass/E773FR ESE(T) laminates with 90° material orientation (dimensions are in inches)

2.4 Full-field TSA Experiments, FE Analyses, and Savin's Solution Verifications for Open-hole Composites without Coated Layers

In addition to the previous edge fracture TSA verifications, the TSA result of an open-hole S2-glass/E773FR laminated coupon, which is 1.5 inches wide and 10 inches long with a 0.25-inch diameter circular hole, is investigated. This section employs the same lay-up sequence $[0_5/90/0_5]$ used in Section 2.3. The coupon with a 30° material direction was chosen to generate the material anisotropy. Therefore, the lay-up can be taken as $[30_5/-60/30_5]$. The TSA experiments follow the same procedure described in Section 2.3. Finite element simulation using Abaqus' 8-node continuum plane stress elements (CPS8R) is used for verification. Figure 2.23 illustrates the dimensions and the FE meshes for the open-hole laminate used in this study.

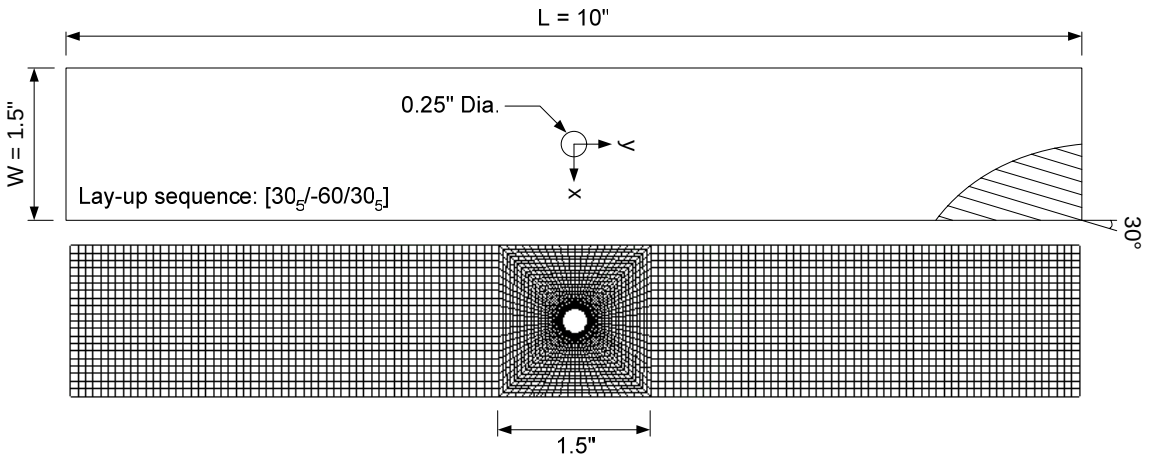

Fig. 2.23. Finite element mesh and geometry of open-hole specimens

Savin's elasticity solution (1961) for anisotropic materials is also used to compare with the experimental TSA signal. A more comprehensive derivation of Savin's solution can be found in the Appendix A. Here are the highlights of the equations employed in this study. Suppose that an infinitely large anisotropic plate, shown in Fig. 2.24, with an elliptical hole is subjected to remote stresses, *p*, acting at an angle α with respect to the x-axis. Consequently, the stresses applied in the infinite distance can be expressed as:

$$\sigma_x^{(\infty)} = p \cdot \cos^2 \alpha \tag{2.23a}$$

$$\sigma_y^{(\infty)} = p \cdot \sin^2 \alpha \tag{2.23b}$$

$$\tau_{xy}^{(\infty)} = p \cdot \sin \alpha \cdot \cos \alpha \tag{2.23c}$$

The stress state at each point in the anisotropic plate due to the remote stresses can be expressed as:

$$\sigma_x = p \cdot \cos^2 \alpha + 2\,\mathrm{Re}[\mu_1^2 \varphi_0'(z_1) + \mu_2^2 \psi_0'(z_2)] \tag{2.24a}$$

$$\sigma_y = p \cdot \sin^2 \alpha + 2\,\mathrm{Re}[\varphi_0'(z_1) + \psi_0'(z_2)] \tag{2.24b}$$

$$\tau_{xy} = p \cdot \sin \alpha \cdot \cos \alpha - 2\,\mathrm{Re}[\mu_1 \varphi_0'(z_1) + \mu_2 \psi_0'(z_2)] \tag{2.24c}$$

where the potential functions, φ_0 and ψ_0, are in terms of complex variables, z_1 and z_2.

φ_0' and ψ_0' are the derivatives with respect to their individual variables. The potential functions can be expressed as:

$$\varphi_0(z_1) = -\frac{ip(a - i\mu_1 b)}{4(\mu_1 - \mu_2)}\left\{\frac{b(\mu_2 \sin 2\alpha + 2\cos^2\alpha) + ia(2\mu_2 \sin^2\alpha + \sin 2\alpha)}{z_1 + \sqrt{z_1^2 - (a^2 + \mu_1^2 b^2)}}\right\} \tag{2.25a}$$

$$\psi_0(z_2) = \frac{ip(a - i\mu_2 b)}{4(\mu_1 - \mu_2)}\left\{\frac{b(\mu_1 \sin 2\alpha - 2\cos^2\alpha) + ia(2\mu_1 \sin^2\alpha + \sin 2\alpha)}{z_2 + \sqrt{z_2^2 - (a^2 + \mu_2^2 b^2)}}\right\} \tag{2.25b}$$

where *i* is the imaginary unit; *a* and *b* are the two major axes of the elliptical hole; μ_1 and μ_2 are the roots of the following characteristic equation of the anisotropic medium having the material orientation, θ, with respect to the y-axis.

$$a_{11}\mu^4 - 2a_{16}\mu^3 + (2a_{12} + a_{66})\mu^2 - 2a_{26}\mu + a_{22} = 0 \tag{2.26}$$

where the a_{ij} are material compliances. It can be seen that Eq. (2.26) is general and not limited to any material system.

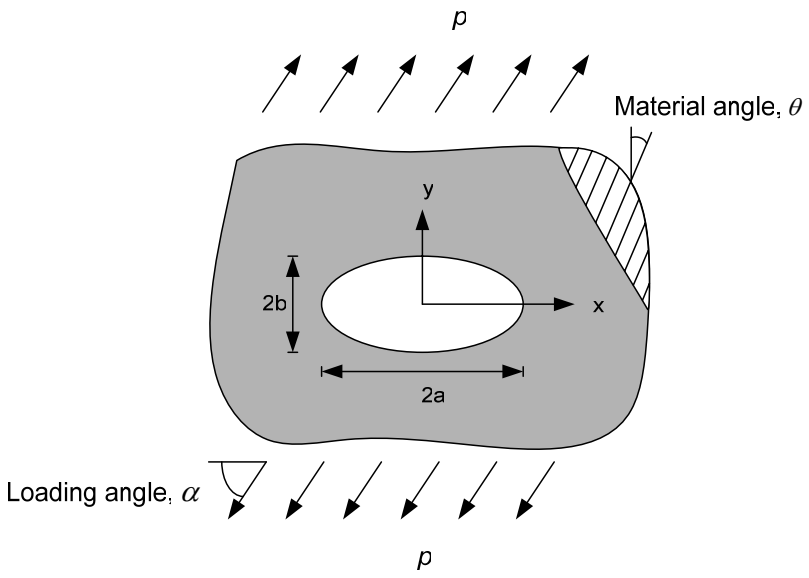

Fig. 2.24. Infinitely large anisotropic plate subjected to remote stresses

The loading angle used in this study is 90°. Therefore, the potential functions reduce as follows:

$$\varphi_0(z_1) = \frac{pa(1-i\mu_1)}{2(\mu_1-\mu_2)} \frac{a\mu_2}{z_1 + \sqrt{z_1^2 - a^2(1+\mu_1^2)}} \tag{2.27a}$$

$$\psi_0(z_2) = -\frac{pa(1-i\mu_2)}{2(\mu_1-\mu_2)} \frac{a\mu_1}{z_2 + \sqrt{z_2^2 - (a^2+\mu_2^2 b^2)}} \tag{2.27b}$$

Figure 2.25 shows the line interrogation of the IR signal along x-axis from the center of the hole to the edge of the specimen. The IR signal from the TSA method shows scatters due to the variability in the experiments. The FE analysis and Savin's solution match well with the overall TSA signal. The Savin's solution is derived from an infinite plate subjected to remote stresses, whereas the FE analysis uses a finite geometry in this study. Therefore, a slight difference between Savin's solution and FE analysis is shown close to the edge of the specimen.

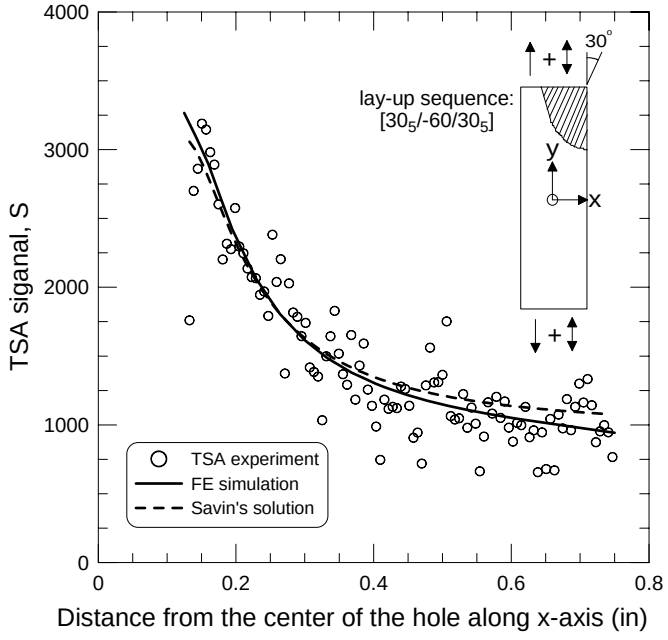

Fig. 2.25. Finite element and Savin's elasticity solution simulation for TSA signal of S2-glass/E773FR notched laminate with an open-hole

CHAPTER 3

A TSA METHOD FOR MIXED-MODE STRESS INTENSITY FACTORS (SIFS) IN COMPOSITES

This chapter introduces Lekhnitskii's solution for calculating the mixed-mode SIFs in anisotropic materials. The proposed quantitative TSA techniques are used together with Lekhnitskii's solution to investigate the mixed-mode SIFs for the crack tip in two composite material systems with and without a surface coat. The first material system is E-glass/polyester pultruded composite with a transversely isotropic coat. The second material system is S2-glass/E773FR orthotropic composite laminate without a surface coat. The quantitative TSA techniques applied to the two composite systems can obtain the full-field sum of in-plane strains by mapping the captured infrared signal via the pre-calibrated thermo-mechanical coefficients. The least-squares method is employed to fit the sum of in-plane strains with a polynomial expansion composed of complex variables in order to calculate the coefficients required for mixed-mode SIFs. The simulated sum of in-plane strains from FE and the VCCT technique using FE also provide comparisons with the TSA sum of in-plane strain field for mixed-mode SIFs.

3.1 Lekhnitskii's Anisotropic Elasticity Solution

Hooke's law for linear stress-strain relationship material under plane-stress can be expressed as:

$$\{\varepsilon\}_{xy} = [\,a\,]_{xy}\{\sigma\}_{xy} \tag{3.1}$$

where $[a]$ is the material compliance matrix. To solve the stress and strain field near the crack tip, Lekhnitskii (1963) employed a special coordinate transformation in the form of

conformal mapping using complex variables.

In the physical plane (Z-plane),

$$z_j = x + \mu_j y, \quad j = 1,2 \tag{3.2a}$$

In the complex plane (ξ-plane),

$$\xi_j = \varsigma + \mu_j \eta, \quad j = 1,2 \tag{3.2b}$$

where μ_1 and μ_2 are roots of the equation:

$$a_{11}\mu^4 - 2a_{16}\mu^3 + (2a_{12} + a_{66})\mu^2 - 2a_{26}\mu + a_{22} = 0 \tag{3.3}$$

Equation (3.3) has four complex roots and they are the two conjugate pairs shown in Eqs. (3.4). Only the positive imaginary parts or the negative imaginary parts are usually used in the expansion of the deformation fields. The order of the roots is not important. Numerical results, shown later in this study, yield the same SIFs for both pairs of roots. In this study, the selected roots are with the positive imaginary parts denoted by μ_1 and μ_2. Therefore, the roots of Eq. (3.3) are written as follows:

$$\mu_1 = \alpha_1^* + i\beta_1^* \tag{3.4a}$$
$$\mu_2 = \alpha_2^* + i\beta_2^* \tag{3.4b}$$
$$\mu_3 = \overline{\mu}_1 \tag{3.4c}$$
$$\mu_4 = \overline{\mu}_2 \tag{3.4d}$$

For isotropic materials, the material compliance, a_{ij}, becomes $a_{16} = a_{26} = 0$, and $a_{11} = a_{22} = 2a_{12} + a_{66}$. The two independent roots become: $\mu_1 = \mu_2 = \pm i$. For orthotropic case, $a_{16} = a_{26} = 0$, and these roots become: $\mu_1 = i \cdot \beta_1^*$, $\mu_2 = i \cdot \beta_2^*$, $\mu_3 = -i \cdot \beta_1^*$, and $\mu_4 = -i \cdot \beta_2^*$. It can be seen that Eq. (3.1) is general and not limited to any material system.

The displacement components in the Z-plane can be expressed by a general polynomial

using the expansion form:

$$u = \sum_{j=1}^{2n} D_j(z_1, z_2)\beta_j \tag{3.5}$$

$$\mathrm{v} = \sum_{j=1}^{2n} E_j(z_1, z_2)\beta_j \tag{3.6}$$

where β_j are determined by known remote boundary conditions using the FE approach described in Khalil et al. (1986). The tractions and the displacements, in the form of a series expansion as a function of β_j, are used to express the potential energy. Then the β_j can be obtained in an equilibrium state by differentiating the potential energy with respect to β_j. In this study, the β_j are coefficients to be determined by thermoelastic data as described in the previous section. The functions D and E in Eqs. (3.5) and (3.6) can be expressed as:

$$D_j(z_1, z_2) = 2\,\mathrm{Re}\left\{ p_1 z_1^{j/2} + p_2 M_{1j} z_2^{j/2} \right\} \tag{3.7a}$$

$$D_{j+n}(z_1, z_2) = 2\,\mathrm{Re}\left\{ i \cdot p_1 z_1^{j/2} + p_2 M_{2j} z_2^{j/2} \right\} \tag{3.7b}$$

$$E_j(z_1, z_2) = 2\,\mathrm{Re}\left\{ q_1 z_1^{j/2} + q_2 M_{1j} z_2^{j/2} \right\} \tag{3.8a}$$

$$E_{j+n}(z_1, z_2) = 2\,\mathrm{Re}\left\{ i \cdot q_1 z_1^{j/2} + q_2 M_{2j} z_2^{j/2} \right\} \tag{3.8b}$$

$$p_j = a_{11}\mu_j^2 + a_{12} - a_{16}\mu_j, \quad j = 1, 2 \tag{3.9a}$$

$$q_j = \frac{a_{12}\mu_j^2 + a_{22} - a_{26}\mu_j}{\mu_j}, \quad j = 1, 2 \tag{3.9b}$$

$$M_{1j} = \frac{-\beta_1^*}{\beta_2^*} \quad \text{and} \quad M_{2j} = \frac{\alpha_2^* - \alpha_1^*}{\beta_2^*} - i \quad \text{for odd } j \tag{3.9c}$$

$$M_{1j} = -1 + i\frac{\alpha_1^* - \alpha_2^*}{\beta_2^*} \quad \text{and} \quad M_{2j} = -i\frac{\beta_1^*}{\beta_2^*} \quad \text{for even } j \tag{3.9d}$$

The proposed method is developed by differentiating Eqs. (3.5) and (3.6) to obtain the strain components.

$$\varepsilon_x = \frac{\partial u}{\partial x} = \sum_{j=1}^{2n} F_j(z_1, z_2) \cdot \beta_j \tag{3.10}$$

$$\varepsilon_y = \frac{\partial \mathrm{v}}{\partial y} = \sum_{j=1}^{2n} G_j(z_1, z_2) \cdot \beta_j \tag{3.11}$$

where

$$F_j = j \cdot \mathrm{Re}\left\{ p_1 [x + \mu_1 y]^{\frac{j-2}{2}} + p_2 M_{1j} [x + \mu_2 y]^{\frac{j-2}{2}} \right\} \tag{3.12a}$$

$$F_{j+n} = j \cdot \mathrm{Re}\left\{ i \cdot p_1 [x + \mu_1 y]^{\frac{j-2}{2}} + p_2 M_{2j} [x + \mu_2 y]^{\frac{j-2}{2}} \right\} \tag{3.12b}$$

$$G_j = j \cdot \mathrm{Re}\left\{ q_1 \mu_1 [x + \mu_1 y]^{\frac{j-2}{2}} + q_2 \mu_2 M_{1j} [x + \mu_2 y]^{\frac{j-2}{2}} \right\} \tag{3.13a}$$

$$G_{j+n} = j \cdot \mathrm{Re}\left\{ i \cdot q_1 \mu_1 [x + \mu_1 y]^{\frac{j-2}{2}} + q_2 \mu_2 M_{2j} [x + \mu_2 y]^{\frac{j-2}{2}} \right\} \tag{3.13b}$$

In order to calculate the β_j terms, the least-squares method can be employed to fit the Lekhnitskii's solution with the experimental infrared signal. For the composites with a transversely isotropic surface layer, the residual of the error is defined as:

$$R = \sum_{i=1}^{m} \left(\sum_{j=1}^{2n} (F_j + G_j) \cdot \beta_j - k_\varepsilon S \right)^2 \tag{3.14}$$

For the composite with an orthotropic surface layer, the residual of the error is defined as:

$$R = \sum_{i=1}^{m} \left(S - (H_1 \, d\varepsilon_{11} + H_2 \, d\varepsilon_{22}) \right)^2 \tag{3.15}$$

Minimizing R with respect to the analytical expansion coefficients requires the solution of

$$\frac{\partial R}{\partial \beta} = 0 \tag{3.16}$$

for the set of expansion coefficients β_j. Once the β's are known, the stress intensity factors near the crack tip are evaluated from the two coefficients, β_1 and β_{n+1}, by:

$$K_I = \sqrt{2\pi}\left[\left(1-\frac{\beta_1^*}{\beta_2^*}\right)\beta_1 + \frac{\left(\alpha_2^*-\alpha_1^*\right)\beta_{n+1}}{\beta_2^*}\right] \tag{3.17}$$

$$K_{II} = -\sqrt{2\pi}\left\{\left(a_1^* - \frac{\alpha_2^*\beta_1^*}{\beta_2^*}\right)\beta_1 + \left[\beta_2^* - \beta_1^* + \frac{\alpha_2^*\left(\alpha_2^*-\alpha_1^*\right)}{\beta_2^*}\right]\beta_{n+1}\right\} \tag{3.18}$$

3.2 Validation of Theoretical and Numerical Methods

An ESE(T) FE fracture model is used in this section to verify the Lekhnitskii's solution. The single-edge-notch specimen is subjected to a tension loading applied to the eccentric holes on the notched side. Figure 3.1 illustrates the FE mesh and the geometry. To compare with the Lekhnitskii's solution, FE analysis together with the virtual crack closure technique (VCCT) is employed. A comprehensive discussion on the VCCT technique can be found in Krueger (2002). The ABAQUS general purpose FE code is used with 8-node continuum plane stress elements (CPS8R). Figures 3.2 and 3.3 show the schematics of the VCCT spring configurations used to generate the needed crack-tip forces and displacements along with the 8-node elements. The spring stiffness, k_s and k_h, are chosen as 1×10^{-8} and 1×10^{8} kip/in, respectively (El-Hajjar, 2004). The mode-I and mode-II energy release rate (ERR) can be expressed by:

$$G_I = \frac{1}{2B\Delta}\left(F_3\cdot\delta_1 + F_4\cdot\delta_2\right) \tag{3.19}$$

$$G_{II} = \frac{1}{2B\Delta}\left(F_3\cdot\delta_1 + F_4\cdot\delta_2\right) \tag{3.20}$$

where Eq. (3.19) corresponds to Fig. 3.2, and Eq. (3.20) corresponds to Fig. 3.3; the B is the thickness; the Δ is the element size; the δ_1 and δ_2 are displacements in the soft springs; the F_3 and F_4 are reactions in the hard springs.

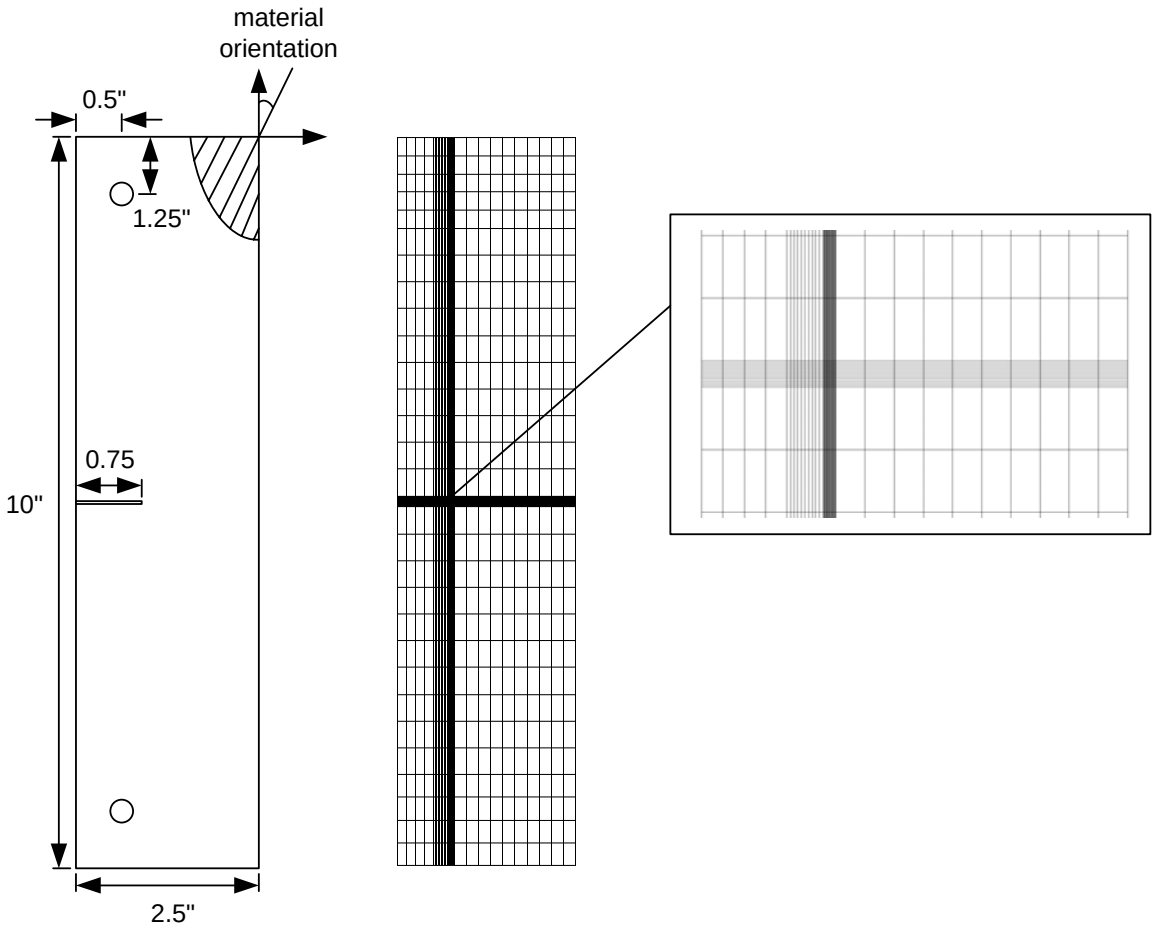

Fig. 3.1. Finite element mesh and geometry of ESE(T) fracture specimen

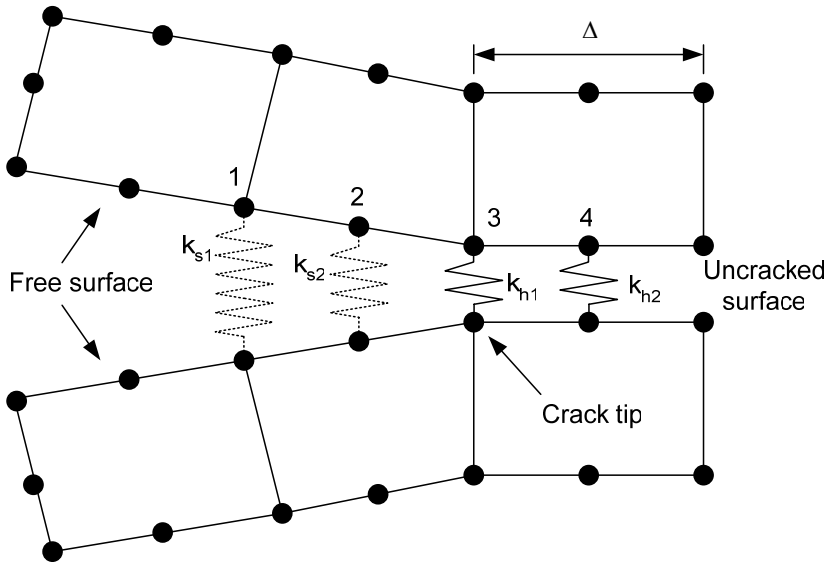

Fig. 3.2. 8-node FE element schematic for mode-I VCCT spring configuration

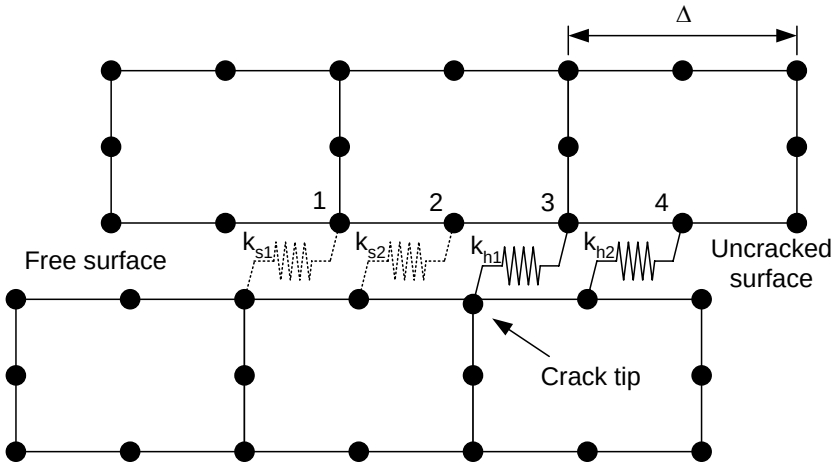

Fig. 3.3. 8-node FE element schematic for mode-II VCCT spring configuration

The fracture relations of Sih et al. (1965) are employed with the ERRs, G_I and G_{II}, from the FE solution in order to determine the mixed-mode SIFs for anisotropic coupons. Two coupled equations are used to relate the SIFs and ERR under a mixed-mode condition:

$$G_I = -\frac{K_I}{2} a_{22} \operatorname{Im}\left[\frac{K_I(\mu_1+\mu_2)+K_{II}}{\mu_1\mu_2}\right] \tag{3.21}$$

$$G_{II} = \frac{K_{II}}{2} a_{11} \operatorname{Im}\left[K_{II}(\mu_1+\mu_2)+K_I\mu_1\mu_2\right] \tag{3.22}$$

where μ_1 and μ_2 are the roots of Eq. (3.3); a_{11} and a_{22} are the material compliances. The SIFs solved by the FE solutions and Sih's equations are herein termed VCCT-Sih.

The FE solution for the displacement or strain fields can be also used to solve for the coefficients in Lekhnitskii's solution. This is used to directly compare for the VCCT and experimental TSA. Once Lekhnitskii's coefficients are determined for the FE models, the SIFs can be determined directly using the appropriate calibrated polynomial expansion coefficients. These are referred herein as the numerical Lekhnitskii-FE. The ABAQUS general purpose FE code was previously described in Section 2.3, and the mesh configuration was illustrated in Fig. 2.11. Strain values are evaluated at the nodes within a ring-shaped region shown in Fig. 3.4. The ring-shaped region is used for selecting the nodes needed to calculating the β's and obtain the SIFs. To avoid the free edge effect, a region of 30° from the free crack surface is not included in the analysis. In addition, the crack tip usually exhibits damage and plasticity that are not accounted for in the Lekhnitskii's solution. Thus, a minimum ring radius is used to exclude the crack tip effects. For the least-squares method, more nodes in a large radius can increase the accuracy of the best fit. However, the Lekhnitskii's solution is valid only in the near crack tip vicinity, so a region with a large maximum ring radius can reduce the accuracy. As a result, a maximum ring radius is to be determined.

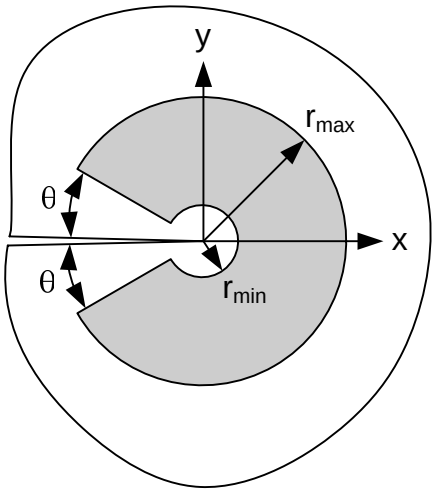

Fig. 3.4. Selected region for Lekhnitskii's solution

A parametric study for minimum and maximum radii of the ring-shaped region is investigated using Lekhnitskii-FE approach. The results are compared with VCCT-Sih to determine the radii used in this study. The mode-I SIF obtained form VCCT-Sih approach is 1.68 $ksi\sqrt{in}$. Figures 3.5 to 3.7 represent the relative error of mode-I SIF with varied expansion number. Each curve in one figure represents different inner radii with various ring width normalized by the length of ligament, 1.75 inches, in the ESE(T) specimen. It can be observed that the curve with expansion number of 6, minimum radius of 0.1 inches, and maximum radius of 0.4 converges to the VCCT result.

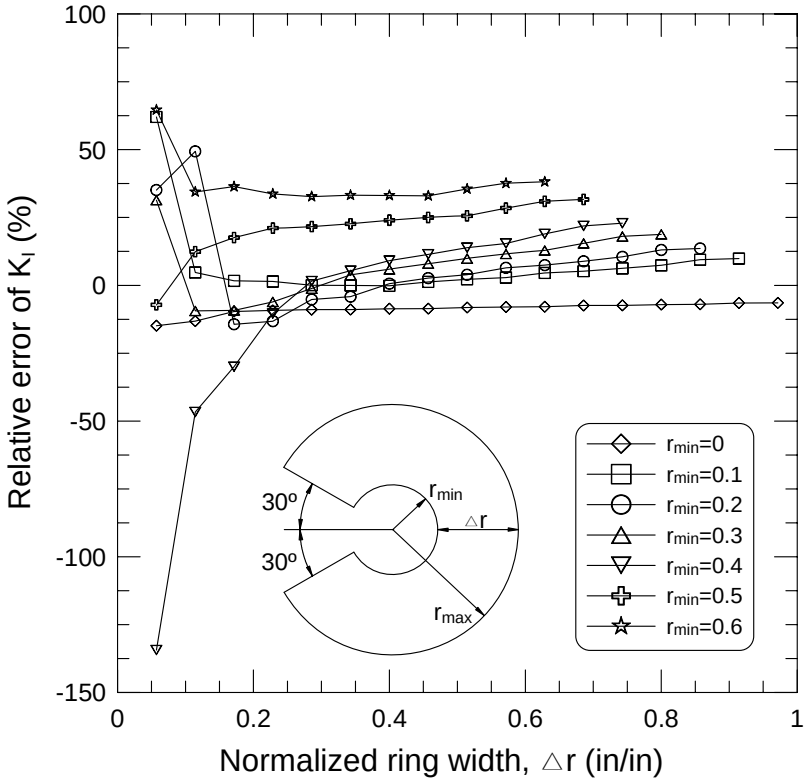

Fig. 3.5. Ring radii parametric study for expansion number of 4

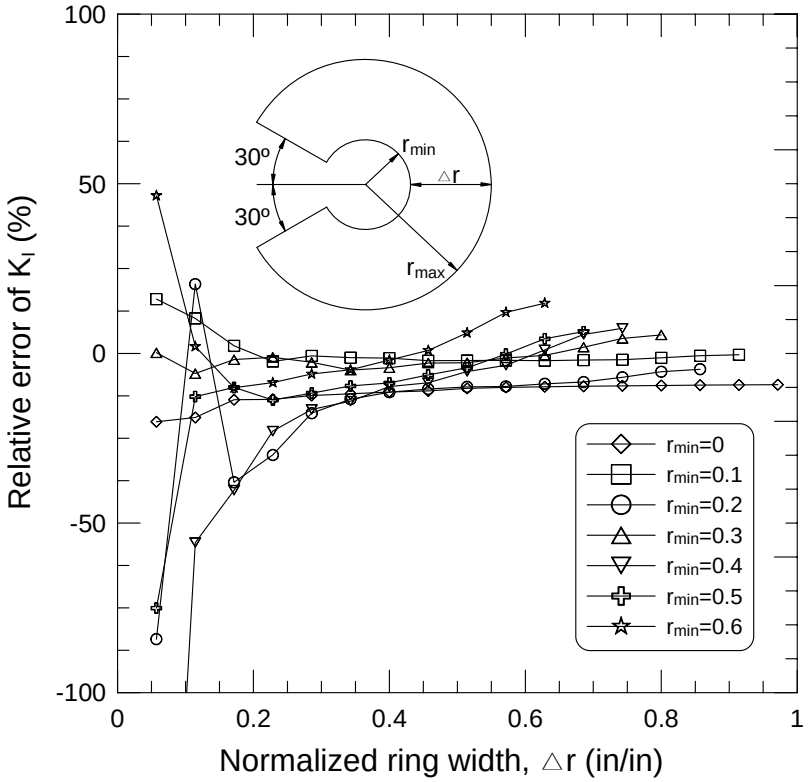

Fig. 3.6. Ring radii parametric study for expansion number of 6

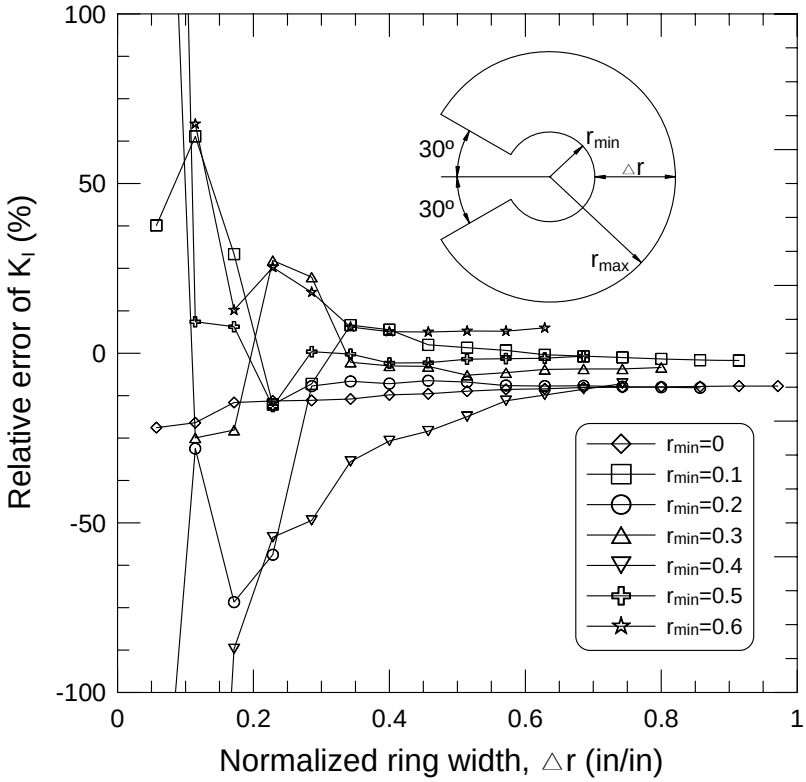

Fig. 3.7. Ring radius parametric study for expansion number of 8

The mesh size can also affect the convergence of the FE solution, especially in the crack tip vicinity. Various mesh sizes are investigated for the Lekhnitskii-FE approach. Based on previous results, the section uses 6 expansion terms for the sum of in-plane strains and 0.1 and 0.4 inches for minimum and maximum radius, respectively. Table 3.1 shows the results of different mesh sizes of Lekhnitskii-FE analysis compared to the results of VCCT-Sih.

Table 3.1. Convergence study for stress intensity factor of pultruded ESE(T) material

Material Angle	SIFs $ksi\sqrt{in}$	VCCT-Sih	Lekhnitskii-FE					
			0.1*	0.08*	0.05*	0.03*	0.02*	0.01*
0°	K_I	1.68	1.35	1.60	1.64	1.67	1.69	1.68
	K_{II}	0.00	0.00	0.00	0.00	0.00	0.00	0.00
30°	K_I	1.52	1.12	1.41	1.28	1.31	1.32	1.31
	K_{II}	0.25	0.05	0.15	0.07	0.07	0.07	0.07
45°	K_I	1.61	0.97	1.11	1.12	1.14	1.15	1.14
	K_{II}	0.39	0.04	0.05	0.05	0.05	0.05	0.05
90°	K_I	1.35	1.09	1.28	1.32	1.35	1.36	1.35
	K_{II}	0.00	0.00	0.00	0.00	0.00	0.00	0.00

* Denote element size in inches.

3.3 Experimental Setup, Test Procedure for Cracked Specimens, and Results

Anisotropic ESE(T) specimens are used to apply the proposed TSA methods and to quantify the coupled mode-I and mode-II SIFs (K_I and K_{II}). The geometry of the specimens is described in Fig. 2.9. Four pultruded and S2-glass/E773FR $[0_5/90/0_5]$ laminated samples are cut from their monolithic plates with four different fiber orientations (0°, 30°, 45°, and 90°) with respect to loading direction. These orientations are used in order to generate different material anisotropy and coupling in the mixed-mode SIFs. The in-plane elastic properties of the monolithic plates are listed in Table 2.1. Note the added 90° layer in the laminated coupons is inserted in the mid-layer to provide for stiffness normal to the 0° fibers. This prevents early cracking in the matrix especially for the cases where the loading is normal to the 0° layers. The cracked samples are tested under the cyclic loading applied by the MTS 810 servo-hydraulic system. The DT1500 IR camera takes the full-field IR images integrated over one minute duration. The IR camera is synchronized with the frequency of the cyclic loading in order to match the maximum and minimum material response. This study uses the frequency of 5Hz for the

cyclic loading. Section 2.3 has proved this loading frequency is sufficient for the materials to achieve the adiabatic condition.

The acquired IR images need to be transformed to the sum of in-plane field in order to be applied to the Lekhnitskii's solution. For the pultruded composites with a transversely isotropic coat, the obtained IR filed around the crack tip is converted to the sum of in-plane strains via one thermo-mechanical coefficient calibrated in Section 2.2. Equation (2.13) describes the relation converting the IR signal to the sum of in-plane strains with the thermo-mechanical coefficient. Figures 2.15(b) to 2.18(b) show the converted sum of in-plane strain fields in the crack tip vicinity (0.8×0.8 square inches) for different material orientations. For the S2-glass/E773FR laminates without the coat, the calibrated coefficients in Section 2.2 is used in Eq. (2.19). Figures 2.19(b) to 2.22(b) show the IR images near the tip vicinity (0.8×0.8 square inches) for different material orientations. The least-squares method is then used to experimentally determine the elasticity coefficients and corresponding SIFs. The ring-shaped region described in Section 3.2 is utilized for selecting the required nodes to perform the least-squares fit.

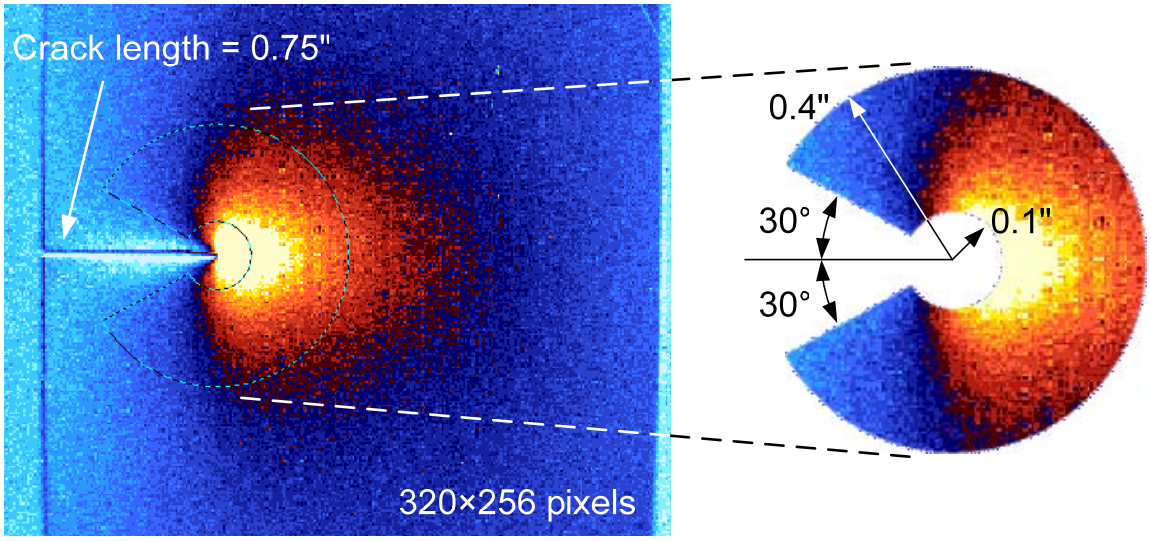

Fig. 3.8. Ring-shaped region used for the least squires fit in a typical IR image

Tables 3.2 and 3.3 show the obtained SIFs for the two material systems using different techniques for composite materials with and without coat, respectively. The number of sample points in the prescribed ring-shaped region for FE analysis coupled with Lekhnitskii's solution and for the experimental TSA techniques are 11,820 and approximately 5,000, respectively. It is shown that the mode-I SIF has a good agreement, whereas the mode-II SIF has larger relative errors for most cases. The errors could be attributed to the following four main sources. First, the K_{II} values are small such that the scatters in the experiments could contaminate the accuracy. Second, the K_{II} is sensitive to the crack tip location, and the inelastic or damage zone around the crack tip in composite materials is not well-defined. Therefore, the actual location of the crack tip is unknown. Third, the friction generated by the mode-II loading at the crack tip may also affect the accuracy of the mode-II SIF. Fourth, the SIFs are derivatives and the proposed method is for the sum and therefore this can explain the poor approximation of the SIFs. Consequently, the main focus of this study was on the general method of interpreting the strain invariants of the TSA images and their application to the SIFs.

Table 3.2. Stress intensity factors in the pultruded composite system

Material Angle	SIFs ($ksi\sqrt{in}$)	VCCT-Sih	Lekh-FE	Lekh-TSA
0°	K_I	2.10	2.05 (-2.38)	1.74 (-17.14)
	K_{II}	0.00	0.00 (-)	0.18 (-)
30°	K_I	1.76	1.71 (-2.84)	1.57 (-10.80)
	K_{II}	0.05	0.08 (60)	0.26 (420)
45°	K_I	1.79	1.75 (-2.23)	1.67 (-6.70)
	K_{II}	0.09	0.10 (11.11)	0.49 (444)
90°	K_I	1.73	1.69 (-2.31)	1.30 (-24.86)
	K_{II}	0.00	0.00 (0.00)	0.00 (-)

Numbers in parentheses denote relative percent error.

Table 3.3. Stress intensity factors in the S2-glass/E773FR composite system

Material Angle	SIFs ($ksi\sqrt{in}$)	VCCT-Sih	Lekh-FE	Lekh-TSA
0°	K_I	2.25	2.27 (0.89)	2.22(-1.33)
	K_{II}	0.00	0.00 (-)	0.01 (-)
30°	K_I	1.43	1.46 (2.10)	1.54 (7.69)
	K_{II}	0.08	0.15 (87.5)	0.02 (-75.00)
45°	K_I	0.67	0.68 (1.49)	0.53 (-20.90)
	K_{II}	0.06	0.09 (50.00)	0.06 (0.00)
90°	K_I	0.66	0.66 (0.00)	0.53 (-19.70)
	K_{II}	0.00	0.00 (-)	0.00 (-)

Numbers in parentheses denote relative percent error.

CHAPTER 4

MARKOV CHAIN MODELS USING TSA MEASUREMENTS FOR FATIGUE DAMAGE IN COMPOSITE LAMINATES

Markov chain methods are applied to model the stochastic fatigue damage evolution in composite materials subjected to cyclic mechanical loadings and monitored by infrared thermography (IR-T) techniques. The IR signal from the surface of open-hole S2-glass/E733FR laminates is captured concurrently during constant amplitude fatigue loadings. The IR testing has high thermal sensitivity below 10mK and the image integration is synchronized with the mechanical loading. A thermoelastic stress analysis (TSA) technique using thermomechanics is used to process the IR fields and relate them to surface stresses and strains. A damage metric is developed for the composite samples based on area stress reduction threshold. The applicability and validity of the proposed TSA damage index is evaluated by comparing it to stiffness reduction measured at select fatigue intervals using a traditional extensometer. The IR-TSA damage index at the last fatigue cycle is used to calibrate the Markov chain models (MCMs). The damage predictions of the MCMs are then examined at different fatigue cycles. A new method is proposed to construct a stochastic S-N curve utilizing the MCMs. The proposed IR-TSA with MCM is shown to be very effective in predicting the damage evolution and allows constructing a wide-range of stochastic S-N curves for several composite material systems.

4.1 A Cumulative Damage Model using Markov Chain Theory

This section introduces a stochastic cumulative damage (CD) method to describe fatigue damage progression. Previously developed IR-TSA test methods (El-Hajjar and Haj-Ali, 2003, 2004a, 2004b, 2005, and Haj-Ali et al., 2008) have been used in this study. The Markov chain consists of a probability transition matrix (PTM) and distribution. Let π_0 be a row vector representing an assumed initial distribution for the Markov chain. The distribution at step *n* can be expressed as:

$$\pi_n = \pi_0 P^n \tag{4.1}$$

where the *P* is the PTM. For a CD model, with *b*+1 damage states, the PTM can be expressed as:

$$P = \begin{bmatrix} p_0 & q_0 & 0 & 0 & 0 \\ 0 & p_1 & q_1 & 0 & 0 \\ 0 & 0 & \ddots & \ddots & 0 \\ 0 & 0 & 0 & p_{b-1} & q_{b-1} \\ 0 & 0 & 0 & 0 & 1 \end{bmatrix} \tag{4.2}$$

where the *p*'s and *q*'s are conditional probabilities that determine if the current damage state remains or proceeds to the next state, respectively. They can be written as:

$$\begin{aligned} p_j &= P\left\{\text{remain in state } j \mid \text{previously in state } j\right\} \\ q_j &= P\left\{\text{go to state } j+1 \mid \text{previously in state } j\right\} \end{aligned} \tag{4.3}$$

The PTM only has the diagonal terms consisting of p's and *q*'s. This can be explained by the cumulative damage process such that the probability for each damage state going back to the previous state is zero. In addition, each damage state is assumed to proceed within one state. Therefore, the probability for each state proceeding beyond one state is zero.

The following example expands one of the multiplications in Equation (4.1). Suppose the damage state distribution at the n-th cycle is expressed as:

$$\pi_n = \begin{bmatrix} \pi_n(0) & \pi_n(1) & \pi_n(2) & \pi_n(3) & \cdots & \pi_n(b) \end{bmatrix} \tag{4.4}$$

The PTM is expressed as:

$$P = \begin{bmatrix} P(0,0) & P(0,1) & 0 & 0 & 0 \\ 0 & P(1,1) & P(1,2) & 0 & 0 \\ 0 & 0 & \ddots & \ddots & 0 \\ 0 & 0 & 0 & P(b-1,b-1) & P(b-1,b) \\ 0 & 0 & 0 & 0 & 1 \end{bmatrix} \tag{4.5}$$

where the $P(s, t)$ is the conditional probability that the current state, s, stays in the current state, s, (i.e., $t = s$) or proceeds to the next state, t. (i.e., $t = s + 1$)

By multiplying Eq. (4.4) by Eq. (4.5), the state distribution at the (n+1)-th cycle can expressed as:

$$\begin{aligned} \pi_{n+1} &= \pi_n P \\ &= [\pi_n(0)P(0,0) \quad \pi_n(0)P(0,1) + \pi_n(1)P(1,1) \quad \cdots \quad \pi_n(b-1)P(b-1,b) + \pi_n(b)] \\ &= [\pi_{n+1}(0) \quad \pi_{n+1}(1) \quad \cdots \quad \pi_{n+1}(b)] \end{aligned} \tag{4.6}$$

It can be seen that the probability in each state consists of partial probability from previous state and partial probability of current state. Figure 4.1 illustrates the evolution of the damage state distribution described in Eq. (4.1). All the tested specimens are assumed undamaged at the initial state (state 0). Therefore, the initial distribution concentrates at state 0. As the fatigue cycle increases, the distribution spreads over the damage states via the multiplication of PTM. Finally, all the specimens reach the failure state b, which is an "absorbing" state of the Markov chain.

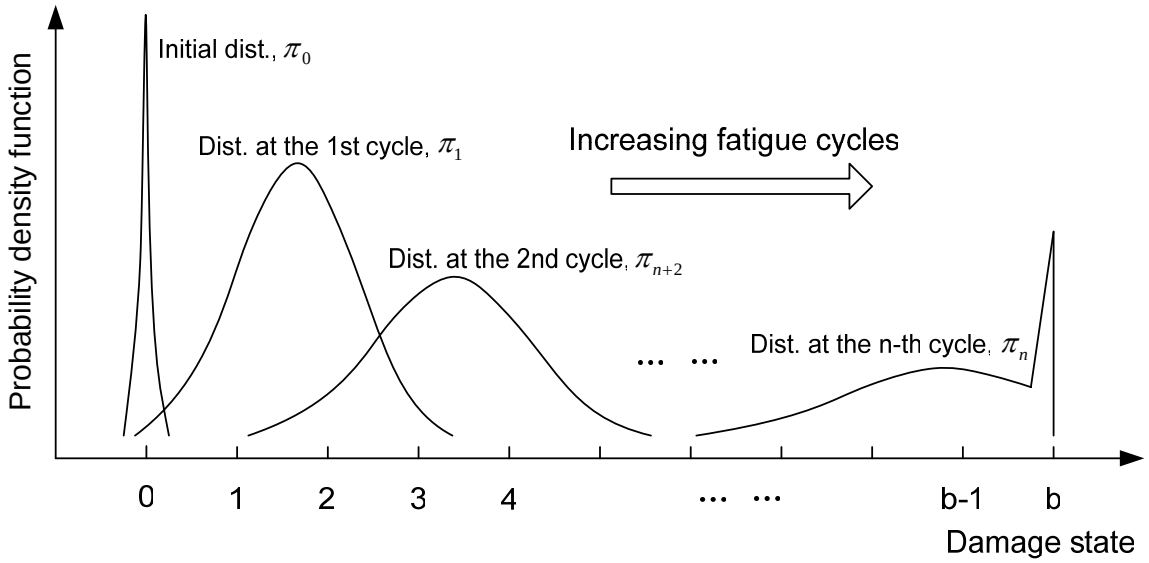

Fig. 4.1. Evolution of probability density function at increasing fatigue cycles

The probability for the first damage state to occur at the y-th trial is given by:

$$f(y) = p^{y-1} \cdot q \tag{4.7}$$

which is a geometric distribution. The mean and variance can be obtained using a moment generating function.

$$G(s) = \sum_{y=1}^{\infty} e^{s \cdot y} p^{(y-1)} q \tag{4.8}$$

which can be simplified as

$$G(s) = \frac{q}{p} \cdot \frac{1}{1 - e^s p} \tag{4.9}$$

The first derivative of Eq. (4.9) yields:

$$G'(s) = \frac{e^s q}{\left(1 - e^s p\right)^2} \tag{4.10}$$

The mean is given by:

$$\mu = G'(0) = \frac{1}{q} \tag{4.11}$$

The second derivative of Eq. (4.9) yields:

$$G''(s) = \frac{e^s q}{(1 - e^t p)^2} + \frac{2 \cdot e^{2s} p \cdot q}{(1 - e^t p)^3} \tag{4.12}$$

Therefore, the variance is given by:

$$\sigma^2 = G''(0) - G'(0)^2 = \frac{p}{q^2} \tag{4.13}$$

Hence, the probabilities can be evaluated by equating Eqs. (4.11) and (4.13). Let

$$r = \frac{\sigma^2}{\mu} = \frac{VAR}{EX} = \frac{p}{q}; \quad p + q = 1 \tag{4.14}$$

If the mean and variance of an arbitrary time of interest are given, the PTM can be determined. Since the PTM is assumed constant through the entire damage process, and the probabilities for each damage state remains or proceeds are *p* or *q*, respectively, the PTM can be expressed as:

$$P = \begin{bmatrix} p & q & 0 & 0 & 0 \\ 0 & p & q & 0 & 0 \\ 0 & 0 & \ddots & \ddots & 0 \\ 0 & 0 & 0 & p & q \\ 0 & 0 & 0 & 0 & 1 \end{bmatrix} \tag{4.15}$$

In this study, the fatigue damage evolution is equally divided by the number of damage states. This number of damage states is to be calibrated to provide suitable MCM predictions for the initially input mean and variance of the cycles to failure.

Figure 4.2 illustrates a schematic showing the upper and lower bounds of cycles to failure predicted by the Markov chain theory. The damage index distributions along the increasing fatigue cycles can be converted from the damage state distributions shown in Fig. 4.1. (i.e., set damage state 0 and b as damage index 0 and 1; other damage states are linearly interpolated)

Up to this point, the Markov theory for stochastic processes has been introduced, and therefore, the fatigue damage evolution through cycles can be constructed once the required parameters, *p* and *q*, in the Markov chain are calibrated form experiments. The variance and mean value of the fatigue cycles for a specific damage state or index (e.g., failure when the damage index equals one) can be defined. Then, the Markov chain model shown in Eq. (4.1) can be constructed and used for describing the fatigue damage evolution.

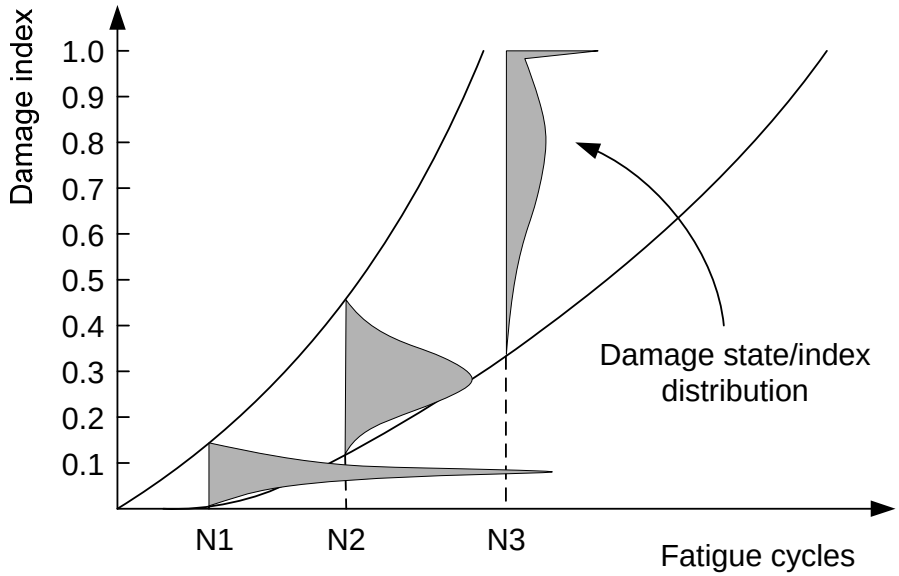

Fig. 4.2. Construction of Markov chain predictions via evolution of damage distribution

4.2 Proposed Fatigue Damage Monitoring using IR-TSA Technique

Infrared TSA (IR-TSA) thermography measurements can be used to describe fatigue damage degradation in laminated composites. The proposed IR-TSA technique provides a high resolution full-field thermal map on the surface of a cyclically loaded material. Fatigue damage, such as delamination, matrix cracking, fiber debonding, and fiber breaking, can cause a reduction in the stiffness and a spatial stress redistribution on the

surface and between the layers. Thus, the surface thermoelastic response changes. Thermoelastic stress analysis of undamaged material relies on reversibility of the load to obtain adiabatic conditions and increase the accuracy by integrating the IR images. However, during fatigue testing, the accumulation of damage, even for relatively low applied stresses, will cause a loss in the adiabatic conditions usually localized within the material. For the case of monitoring fatigue damage using TSA, it is desired to strike a balance between accuracy achieved through long integration periods and obtaining TSA integrated images associated with changing damage states. The full-field thermal data can then be applied to characterize damage evolution.

In this study, fatigue experiments are conducted under two different applied maximum stresses. First series of sixteen laminated composite specimens with an open-hole is tested under the fatigue loading of 50% of their ultimate stress. Second series of tests consists of five specimens with the same geometry, tested under fatigue loadings of 40% of the ultimate stress. The MCMs are used to provide the damage evolution during fatigue for these two sets of experiments.

The twenty-one FRP specimens were cut with a diamond abrasive wet saw from two monolithic 12 inch by 16 inch quasi-isotropic S2-glass/E733FR thin panels cut into 1.5 inch by 10 inch coupons. The panels were manufactured using an autoclave following the prepreg's manufacturer specifications (curing cycles) to achieve a uniform thickness of 1.78 mm (0.070 in) for the quasi-isotropic system. The lay-up sequence of the specimens is $[-45/0/45/90]_s$ and the average (5 repeated tests) elastic properties are listed in Table 4.1.

Table 4.1. In-plane elastic properties of un-notched S2-glass/E733FR laminates

E_{11}	E_{22}	G_{12}	ν_{12}	σ_{uts} (notched)
GPa (Msi)				MPa (ksi)
26.7 (3.879)	26.7 (3.879)	17.5 (2.536)	0.307	322 (46.7)

Each specimen was then notched with a 0.25 inch diameter brad-point drill-bit in its center. A typical specimen and dimensions are illustrated in Fig. 4.3. The ultimate remote tensile stress of a monotonically loaded open-hole laminate tested is given in Table 4.1. The specimens are sprayed with flat black paint and cyclically loaded with a constant amplitude in tension-tension load control with a maximum load corresponding to 50% of their ultimate strength (322 MPa or 46.7 ksi). The applied cyclic maximum stress is 161 MPa (23.4 ksi) with a stress ratio of 0.1 and a frequency of 5Hz. The second set of five specimens follows the same test procedure at 40% of ultimate stress. The number of specimens and their test methods are listed in Table 4.2.

Table 4.2. Number of test specimens and applied stresses

Applied stress level	Number of specimens (Labeled number)	σ_{max}	σ_{min}
		MPa (ksi)	
50%	16 (1 to 16)	161 (23.4)	16.1 (2.4)
40%	5 (17 to 21)	129 (18.7)	12.9 (1.9)

Integrated TSA images of the specimens are obtained every minute (300 cycles) during the fatigue loading. The tests are stopped periodically to take stiffness measurements with a two-inch gauge-length extensometer centered over the open-hole specimens. The infrared camera and extensometer setup is shown in Fig. 4.4. A serviceability failure is defined when the coupon stiffness measured by the extensometer decreases to 60% of the initial stiffness. At this point, the fatigue test is stopped and this state is herein referred to as the final damage state.

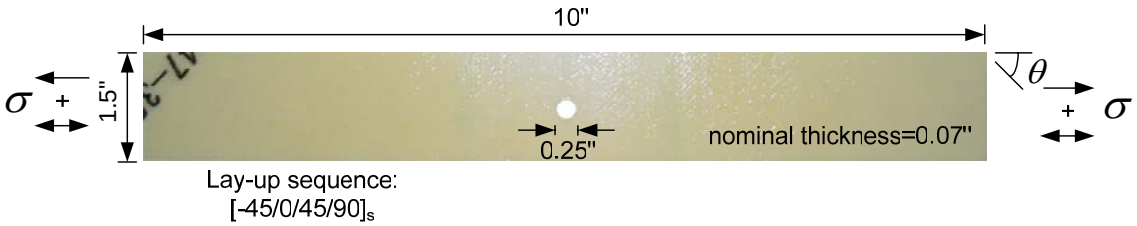

Fig. 4.3. Open-hole S2-glass/E733FR specimen geometry and lay-up sequence

Fig. 4.4. Infrared camera and extensometer experimental setup

One of the major failure modes observed on the surface of the quasi-isotropic laminates is delamination emanating from edges and the stress concentration regions around the hole. Matrix cracking and fiber splitting follow until serviceability failure. The thermal surface field is complicated during damage, especially after delamination because additional thermal excitations are induced by friction and other non-adiabatic source due to localized stress concentrations while stress is reduced in other damaged areas. Areas of delaminated plies that experience little or no mechanical dilatational strains begin to exhibit a thermal response at their edges. These edges can saturate the camera sensors because of the relatively large temperature changes. Data collected from satu-

rated camera sensors is of no value, and the overall spatial average values of temperature change on the surface plies are meaningless after significant delamination has occurred. To represent the effects of delaminations and matrix cracking in the surface ply, other metrics may be applied to the TSA data. In addition to the overall average measures of the TSA response, the spatial data can be reduced by measurements of areas with a specified threshold on TSA or within critical TSA value ranges. However, once damage occurs, it is manifested by a reduction in the TSA field.

In the current study, an accumulation of damage on the surface is defined by an increase of TSA measurement below a critical threshold (set to 5,000 IR relative camera units). Once an area (pixel) has experienced this TSA reduction, it is accumulated within the growing damage zone. This damage area, however, may experiences higher thermal emissions at a later stage due to load redistribution and non-adiabatic sources. The threshold is selected based on the fact that the delaminated areas have little or no stresses (TSA) and do not emit significant infrared. Therefore, the regions with TSA signal below 5,000 IR camera unit are considered damaged. The window of a TSA image is one inch above and below the open-hole to provide a better correlation with stiffness data measurements.

The shaded area shown in Fig. 4.5 represents the accumulated TSA value below 5,000 IR camera units. The area increases as the fatigue cycle increases. The damaged area is the damage metric (variable) that is defined by $A(N_i)$, where N_i is the fatigue cycle. After an area has been identified as damaged for a set of few consecutive images, this area would be accumulated within the irreversible damage zone as shown in Fig. 4.5. Future increases in the TSA signal are assumed to be due to non-adiabatic effects. The

twenty-one open-hole specimens show similar fatigue damage evolution with various service cycles to failure. Thus, the damage evolution metric of the specimens can be used with the Markov chain theory, and their fatigue behaviors are stochastically constructed.

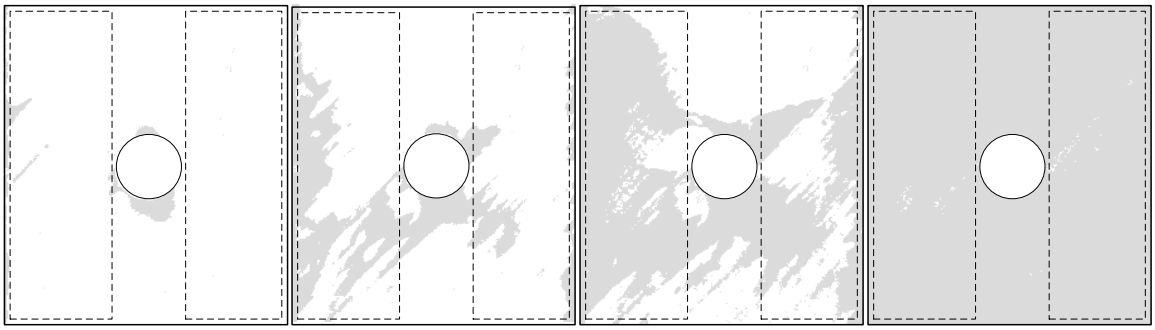

(a) 300 cycles (b) 10,210 cycles (c) 39, 890 cycles (d) 178,830 cycles

Fig. 4.5. Typical evolution of IR-TSA cumulative damage zone under increasing fatigue cycles

4.3 Fatigue Tests for Calibrating Markov Chain Models

Markov chain theory is utilized for both TSA and extensometer measurements. This study defines the final damage state as the state at which the specimen stiffness is reduced to 60% of its initial value. The number of cycles to failure of the specimens is obtained by linear interpolation of the values in Tables 4.3 and 4.4. The normalized damage function, $D^{(S)}(N_i)$, of the damage metric, defined by the stiffness measurements obtained from the extensometer, is defined by:

$$D^{(S)}(N_i) = \frac{S(N_0) - S(N_i)}{0.4 \times S(N_0)} \tag{4.16}$$

where $S(N_0)$ is the initial stiffness, and $S(N_i)$ is a stiffness measurement for a specific fatigue cycle. The damage function is zero for specimens with no damage, and reaches one if the stiffness decreases to 60% of $S(N_0)$.

Once the numbers of cycles to failure, N_f (i.e., $D(N_f)=1$) for each specimen are determined, the TSA images corresponding to those N_f cycles are determined. Recall the damage area, $A(N_i)$, calculated from the TSA images for each failed specimen is $A(N_f)$. The TSA metric or variable can be defined as:

$$D^{(TSA)}(N_i)=\frac{A(N_i)}{A(N_f)} \tag{4.17}$$

Similar to the stiffness damage function, $D^{(S)}$, the TSA damage function ranges from zero to unity corresponding to the initial and final damage limits, respectively. Tables 4.3 and 4.4 show the damage indices calculated from stiffness and TSA measurements for 50% and 40% stress levels, respectively. The first row describes the coupon or test number. The second row lists the initial stiffness and the third row includes the TSA damage area at the last fatigue cycle. The rest of each table includes different fatigue cycles and current fractions of the above two measurements (initial stiffness and final TSA damage area).

Table 4.3. Stiffness and TSA damage indices of 16 quasi-isotropic specimens subjected to 50% stress level measured at different fatigue cycles (stiffness units are in ksi; TSA area units are in pixels)

	1	2	3	4	5	6	7	8
$S(N_0)$ ($A(N_f)$)	3302 (42104)	2922 (32586)	3116 (35493)	3335 (35800)	3400 (33892)	3626 (47041)	3666 (37322)	3404 (32625)
cycles	Damage Indices, $D^{(S)}$ and ($D^{(TSA)}$)							
0	0.00 (0.00)	0.00 (0.00)	0.00 (0.00)	0.00 (0.00)	0.00 (0.00)	0.00 (0.00)	0.00 (0.00)	0.00 (0.00)
6200	0.11 (0.15)	0.03 (0.22)	0.03 (0.04)	0.21 (0.20)	0.08 (0.15)	0.10 (0.17)	0.08 (0.23)	0.26 (0.09)
9300	0.19 (0.22)	0.11 (0.27)	0.06 (0.07)	0.26 (0.28)	0.09 (0.21)	0.11 (0.21)	0.11 (0.28)	0.30 (0.14)
12400	0.21 (0.27)	0.16 (0.30)	0.12 (0.10)	0.30 (0.33)	0.09 (0.26)	0.13 (0.26)	0.13 (0.31)	0.34 (0.17)
15500	0.26 (0.32)	0.18 (0.35)	0.13 (0.13)	0.34 (0.38)	0.10 (0.29)	0.14 (0.28)	0.13 (0.35)	0.37 (0.21)
18600	0.30 (0.35)	0.19 (0.38)	0.15 (0.16)	0.35 (0.44)	0.11 (0.32)	0.18 (0.30)	0.14 (0.41)	0.40 (0.25)
21700	0.33 (0.43)	0.20 (0.41)	0.16 (0.18)	0.36 (0.46)	0.12 (0.33)	0.19 (0.33)	0.14 (0.45)	0.40 (0.29)
27900	0.39 (0.53)	0.23 (0.45)	0.20 (0.23)	0.38 (0.49)	0.14 (0.37)	0.22 (0.37)	0.18 (0.57)	0.43 (0.35)
34100	0.44 (0.61)	0.26 (0.49)	0.23 (0.27)	0.40 (0.53)	0.17 (0.39)	0.25 (0.41)	0.28 (0.71)	0.46 (0.43)
40300	0.47 (0.65)	0.27 (0.52)	0.25 (0.32)	0.42 (0.56)	0.22 (0.46)	0.26 (0.46)	0.34 (0.73)	0.49 (0.52)
46500	0.51 (0.70)	0.31 (0.56)	0.27 (0.35)	0.43 (0.58)	0.26 (0.50)	0.28 (0.50)	0.43 (0.74)	0.50 (0.59)
52700	0.60 (0.78)	0.34 (0.62)	0.30 (0.41)	0.44 (0.60)	0.29 (0.53)	0.30 (0.57)	0.63 (0.75)	0.50 (0.63)
65100	0.66 (0.88)	0.36 (0.70)	0.43 (0.52)	0.46 (0.63)	0.38 (0.66)	0.35 (0.64)	1.04 (1.03)	0.54 (0.69)
77500	0.91 (0.97)	0.39 (0.76)	0.56 (0.76)	0.47 (0.66)	0.46 (0.77)	0.37 (0.76)	-	0.59 (0.76)
89900	1.16 (1.03)	0.48 (0.81)	0.75 (0.96)	0.49 (0.69)	0.56 (0.83)	0.41 (0.81)	-	0.61 (0.78)
102300	-	0.58 (0.85)	0.95 (0.98)	0.52 (0.73)	0.93 (0.98)	0.50 (0.84)	-	0.65 (0.79)
114700	-	0.73 (0.86)	1.14 (1.04)	0.55 (0.76)	1.33 (1.06)	0.58 (0.90)	-	0.68 (0.81)
127100	-	0.81 (0.90)	-	0.59 (0.78)	-	0.67 (0.92)	-	0.72 (0.84)
139500	-	0.98 (0.98)	-	0.62 (0.80)	-	0.79 (0.95)	-	0.84 (0.90)
151900	-	1.01 (1.00)	-	0.64 (0.82)	-	0.95 (0.99)	-	0.98 (0.99)
154986	-	-	-	0.67 (0.84)	-	0.98 (1.00)	-	0.98 (1.00)
164300	-	-	-	0.71 (0.85)	-	1.10 (1.00)	-	1.09 (1.02)
176700	-	-	-	0.74 (0.85)	-	-	-	-
189100	-	-	-	0.83 (0.96)	-	-	-	-
201500	-	-	-	0.94 (0.98)	-	-	-	-
213900	-	-	-	1.15 (1.06)	-	-	-	-

Table 4.3. (Continued) Stiffness and TSA damage indices of 16 quasi-isotropic specimens subjected to 50% stress level measured at different fatigue cycles (stiffness units are in ksi; TSA area units are in pixels)

	9	10	11	12	13	14	15	16
$S(N_0)$ ($A(N_f)$)	3274 (38291)	2799 (39484)	3240 (36680)	3219 (33649)	3334 (35145)	3442 (23953)	3251 (33302)	2743 (37748)
cycles	Damage Indices, $D^{(S)}$ and ($D^{(TSA)}$)							
0	0.00 (0.00)	0.00 (0.00)	0.00 (0.00)	0.00 (0.00)	0.00 (0.00)	0.00 (0.00)	0.00 (0.00)	0.00 (0.00)
6200	0.09 (0.08)	0.10 (0.20)	0.06 (0.19)	0.06 (0.19)	0.06 (0.11)	0.06 (0.26)	0.10 (0.10)	0.15 (0.18)
9300	0.10 (0.12)	0.12 (0.28)	0.10 (0.24)	0.06 (0.29)	0.13 (0.13)	0.09 (0.34)	0.16 (0.13)	0.19 (0.25)
12400	0.15 (0.16)	0.13 (0.35)	0.15 (0.30)	0.11 (0.37)	0.16 (0.17)	0.11 (0.38)	0.18 (0.16)	0.22 (0.31)
15500	0.18 (0.20)	0.13 (0.39)	0.17 (0.34)	0.14 (0.43)	0.18 (0.21)	0.17 (0.43)	0.20 (0.19)	0.25 (0.36)
18600	0.19 (0.25)	0.14 (0.43)	0.21 (0.38)	0.16 (0.48)	0.21 (0.23)	0.18 (0.47)	0.22 (0.22)	0.31 (0.41)
21700	0.21 (0.29)	0.17 (0.45)	0.21 (0.41)	0.17 (0.51)	0.21 (0.28)	0.19 (0.50)	0.25 (0.24)	0.35 (0.45)
27900	0.24 (0.39)	0.18 (0.51)	0.21 (0.46)	0.20 (0.58)	0.25 (0.36)	0.25 (0.54)	0.26 (0.29)	0.41 (0.53)
34100	0.27 (0.46)	0.25 (0.55)	0.25 (0.50)	0.22 (0.63)	0.28 (0.43)	0.26 (0.58)	0.27 (0.33)	0.43 (0.59)
40300	0.27 (0.54)	0.26 (0.58)	0.26 (0.54)	0.25 (0.66)	0.30 (0.47)	0.29 (0.60)	0.28 (0.37)	0.45 (0.64)
46500	0.34 (0.59)	0.27 (0.60)	0.29 (0.58)	0.27 (0.69)	0.33 (0.51)	0.36 (0.71)	0.30 (0.40)	0.46 (0.67)
52700	0.41 (0.66)	0.30 (0.63)	0.32 (0.63)	0.30 (0.70)	0.33 (0.55)	0.38 (0.85)	0.31 (0.44)	0.47 (0.70)
65100	0.42 (0.77)	0.38 (0.72)	0.35 (0.73)	0.34 (0.74)	0.41 (0.61)	0.91 (0.98)	0.38 (0.54)	0.48 (0.74)
77500	0.47 (0.82)	0.48 (0.79)	0.44 (0.84)	0.40 (0.78)	0.45 (0.67)	1.50 (1.10)	0.44 (0.65)	0.50 (0.76)
89900	0.53 (0.87)	0.56 (0.89)	0.47 (0.87)	0.65 (0.92)	0.49 (0.76)	-	0.45 (0.78)	0.52 (0.78)
102300	0.69 (0.90)	0.63 (0.97)	0.80 (0.96)	0.90 (0.98)	0.82 (0.97)	-	0.54 (0.81)	0.55 (0.79)
114700	0.92 (0.98)	1.07 (1.00)	1.23 (1.09)	1.10 (1.00)	1.10 (1.00)	-	0.79 (0.92)	0.56 (0.80)
127100	1.25 (1.02)	-	-	-	-	-	1.09 (1.03)	0.57 (0.81)
139500	-	-	-	-	-	-	-	0.60 (0.83)
151900	-	-	-	-	-	-	-	0.62 (0.84)
154986	-	-	-	-	-	-	-	0.63 (0.85)
164300	-	-	-	-	-	-	-	0.65 (0.86)
176700	-	-	-	-	-	-	-	0.72 (0.88)
189100	-	-	-	-	-	-	-	1.00 (1.00)

Table 4.4. Stiffness and TSA damage indices of 5 quasi-isotropic specimens subjected to 40% stress level measured at different fatigue cycles (stiffness units are in ksi; TSA area units are in pixels)

	17	18	19	20	21
$S(N_0)$	3441	3062	3108	2789	2958
$(A(N_f))$	(18380)	(34603)	(30601)	(24932)	(32616)
cycles	Damage Indices, $D^{(S)}$ and ($D^{(TSA)}$)				
0	0.00 (0.00)	0.00 (0.00)	0.00 (0.00)	0.00 (0.00)	0.00 (0.00)
9000	0.48 (0.00)	0.15 (0.06)	0.27 (0.17)	0.26 (0.09)	0.26 (0.08)
18000	0.54 (0.06)	0.23 (0.06)	0.32 (0.18)	0.32 (0.13)	0.32 (0.12)
36000	0.58 (0.09)	0.34 (0.09)	0.38 (0.20)	0.40 (0.20)	0.37 (0.25)
72000	0.66 (0.17)	0.39 (0.14)	0.43 (0.36)	0.43 (0.34)	0.40 (0.48)
144000	0.70 (0.29)	0.42 (0.21)	0.49 (0.49)	0.49 (0.52)	0.45 (0.74)
216000	0.71 (0.35)	0.43 (0.35)	0.52 (0.59)	0.56 (0.72)	0.51 (0.75)
288000	0.71 (0.42)	0.47 (0.43)	0.53 (0.66)	0.75 (0.96)	0.56 (0.76)
360000	0.72 (0.48)	0.50 (0.50)	0.60 (0.77)	0.89 (0.99)	0.60 (0.78)
432000	0.74 (0.50)	0.53 (0.54)	0.65 (0.88)	0.98 (1.00)	0.63 (0.85)
504000	0.76 (0.53)	0.55 (0.71)	0.75 (0.93)	1.05 (1.00)	0.76 (0.92)
576000	0.78 (0.57)	0.56 (0.75)	0.82 (0.96)	-	0.86 (0.98)
648000	0.80 (0.60)	0.58 (0.79)	0.84 (0.98)	-	0.93 (1.00)
720000	0.81 (0.65)	0.61 (0.81)	0.99 (0.98)	-	1.01 (1.00)
792000	0.82 (0.66)	0.65 (0.84)	1.03 (1.12)	-	-
864000	0.83 (0.70)	0.66 (0.91)	-	-	-
936000	0.83 (0.79)	0.69 (0.93)	-	-	-
1008000	0.85 (0.82)	0.74 (0.94)	-	-	-
1080000	0.87 (0.86)	0.79 (0.95)	-	-	-
1152000	0.89 (0.87)	0.81 (0.95)	-	-	-
1224000	0.90 (0.89)	0.83 (0.99)	-	-	-
1296000	0.92 (0.92)	0.97 (0.99)	-	-	-
1368000	0.94 (0.94)	1.08 (1.08)	-	-	-
1440000	0.96 (0.97)	-	-	-	-
1512000	0.99 (1.00)	-	-	-	-
1584000	1.01 (1.02)	-	-	-	-

Figures 4.6 and 4.7 show the evolution of the average damage curves for the two damage metrics, from the stiffness and TSA experiments of the 16 and 5 specimen sets and subjected to 50% and 40% of their ultimate stress, respectively. Figures 4.6 and 4.7

include maximum 26 direct mechanical stiffness measurements using an extensometer. However, the IR-TSA damage metric curves are composed from hundreds (approximately 600 and 1200 for Figures 4.6 and 4.7, respectively) of full-field IR-TSA images. This demonstrates the advantage of the proposed IR-TSA approach in part because it can be used without interruption of the fatigue testing. In addition to the average values, solid and dashed lines, Figs. 4.6 and 4.7 include the upper and lower cycles to failure bounds plotted horizontally in order to avoid clustering at higher damage values. The bars spanning the fatigue cycles in Fig. 4.6 represent the distributed intervals of the experimental results plotted at the measured stiffness values. The TSA experiments have smaller distributed intervals and thus show less variability along the entire fatigue process. Figure 4.7 shows the damage index from stiffness and TSA experimental results of the second set of 5 specimens subjected to the maximum fatigue loading of its 40% stress loading. The experimental results for the second set exhibit larger scatter than those of the first set due to the nature of fatigue processes having more variability at lower stress levels. Figures 4.8 and 4.9 show the stiffness damage index versus TSA damage index for 50% and 40% stress level, respectively. A function consisting of power and logarithmic functions, shown in Figs. 4.8 and 4.9, is used to least-squares fit the experimental data. One of the specimens in the 40% stress level is excluded in the least-squares fit since its stiffness damage increases dramatically in the first 9,000 fatigue cycles while other specimens perform in a more similar fatigue damage fashion. Overall, the stiffness measurements show more sensitivity to the fatigue damage in the beginning of fatigue life. The TSA damage metric is more capable of capturing the fatigue damage for specimens subjected to more fatigue cycles.

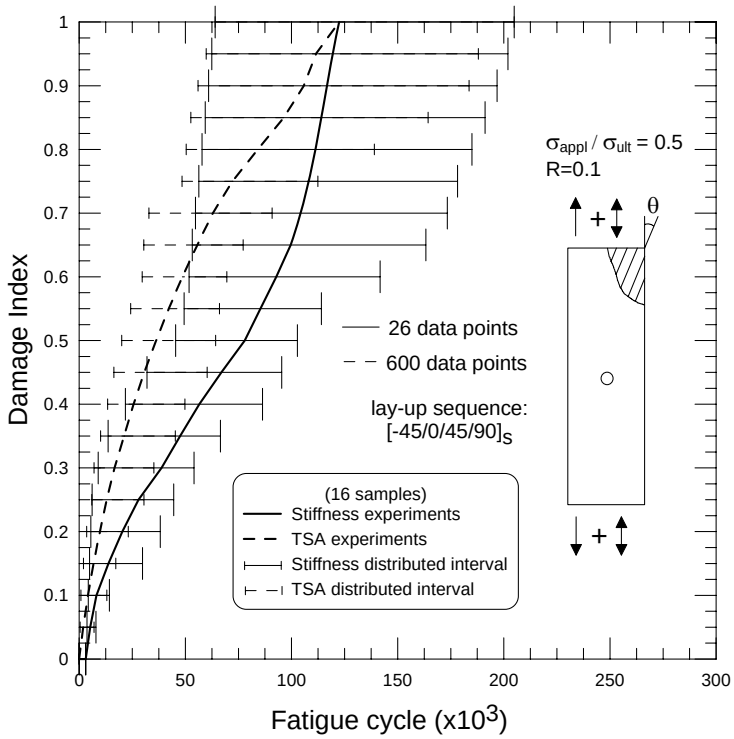

Fig. 4.6. Damage metrics/indices from stiffness and TSA measurements and their distributed intervals as a function of fatigue cycles for 50% stress level

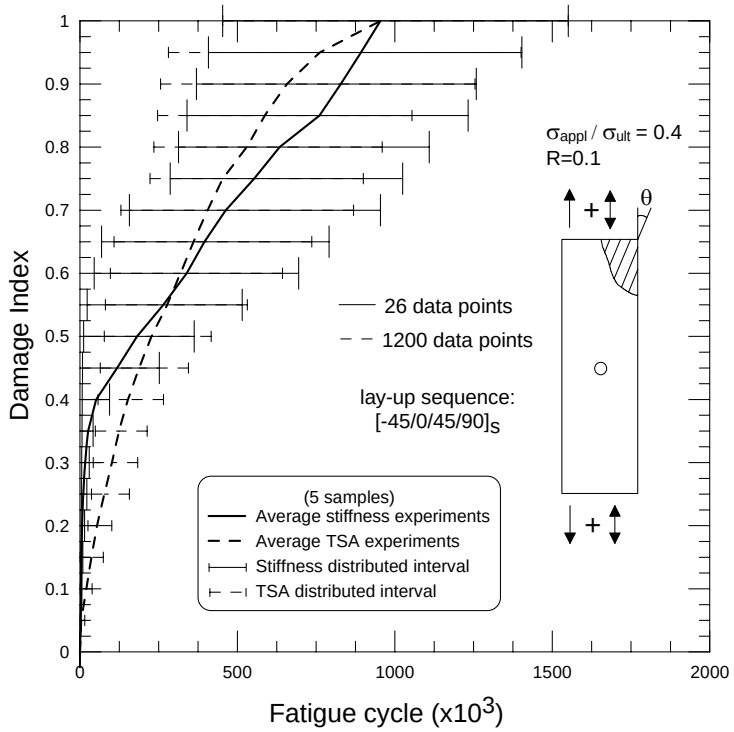

Fig. 4.7. Damage metrics/indices from stiffness and TSA measurements and their distributed intervals as a function of fatigue cycles for 40% stress level

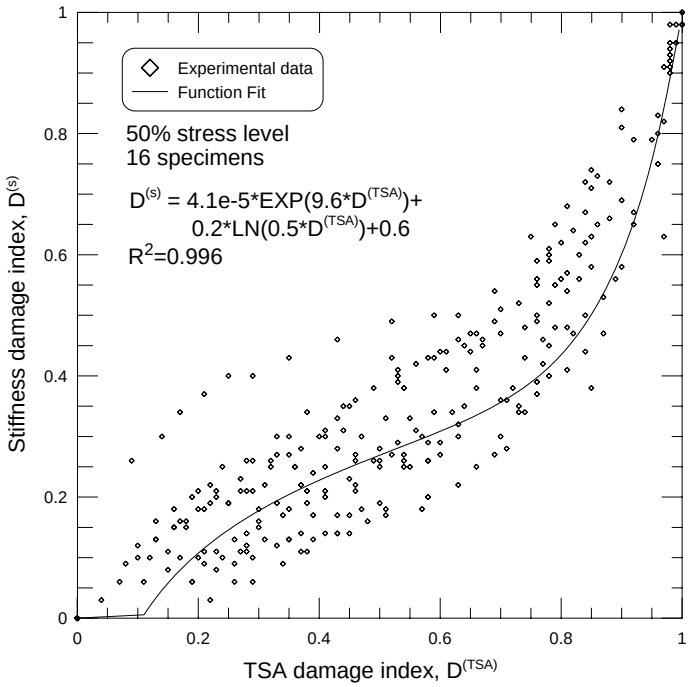

Fig. 4.8. Stiffness damage index versus TSA damage index for 50% stress level

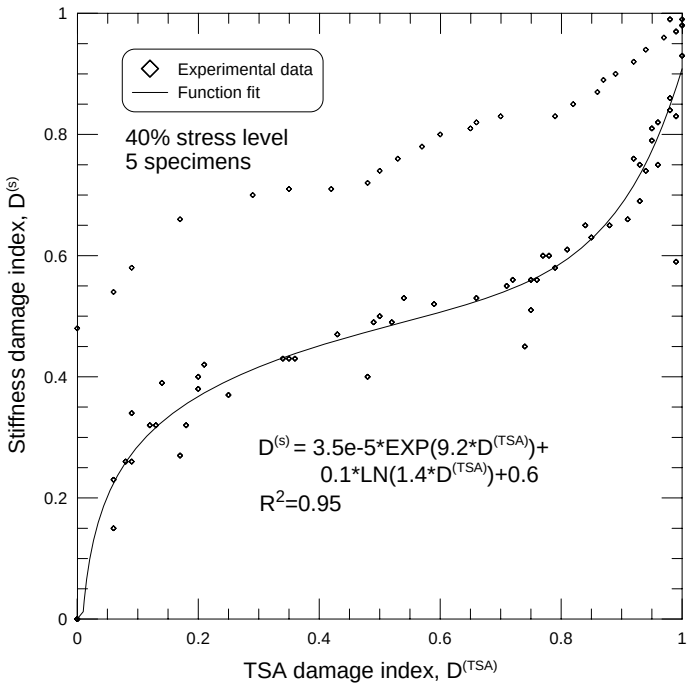

Fig. 4.9. Stiffness damage index versus TSA damage index for 40% stress level

The Markov chain models are separately utilized to simulate the fatigue process for the two sets of specimens subjected to 50% and 40% stress levels. The cycles to failure are used to provide mean and variance for MCM to calibrate the number of damage states. The first set of 16 specimens is randomly sampled to select the number of samples used to calibrate the corresponding MCM. Different MCM calibrations with various numbers of specimens are performed. The maximum and minimum life predictions are generated based on randomly selected specimens. Each randomly-selected procedure for a certain amount of specimens is repeated 10 times, and the predicted maximum and minimum fatigue life under various damage states are averaged over the 10 trials. The maximum and minimum fatigue life predicted from each MCM using the two damage indices are shown in Figs. 4.10 and 4.11. Due to the large number of TSA measurements, the experimental data in Fig. 4.11 has been filtered, and each data point is plotted for every 10 measurements of each of the 16 specimens to allow meaningful plot of total data. The number of damage states of eleven is found to provide suitable predictions for the cycles to failure for the first data set. Therefore, the Markov chain model is calibrated to use 11 damage states (0 to 10) for the two damage functions in the 16 specimens (i.e., corresponding to $D(N_i) = 0$ to 1). The conditional probabilities, p and q, in the stationary Markov chain model are 0.9923 and 0.0077, respectively, determined from Eq. (4.14). It is found that the predictions of maximum and minimum fatigue life bounds satisfactorily converge when five or more fatigue data set are analyzed. Therefore, only five fatigue tests in the second set of coupons (40% stress) are conducted. Figures 4.12 and 4.13 show the upper and lower MCM fatigue life prediction for the second set of tests with the two damage variables, respectively. The experimental TSA data in Fig. 4.13 has

been filtered for every 20 measurements for each specimen. The Markov chain predictions tend to be conservative for the maximum bound of fatigue life when the laminates fail to meet the serviceability requirements (i.e., damage index equals one). This could be attributed to the longer fatigue life of one specimen in experimental results.

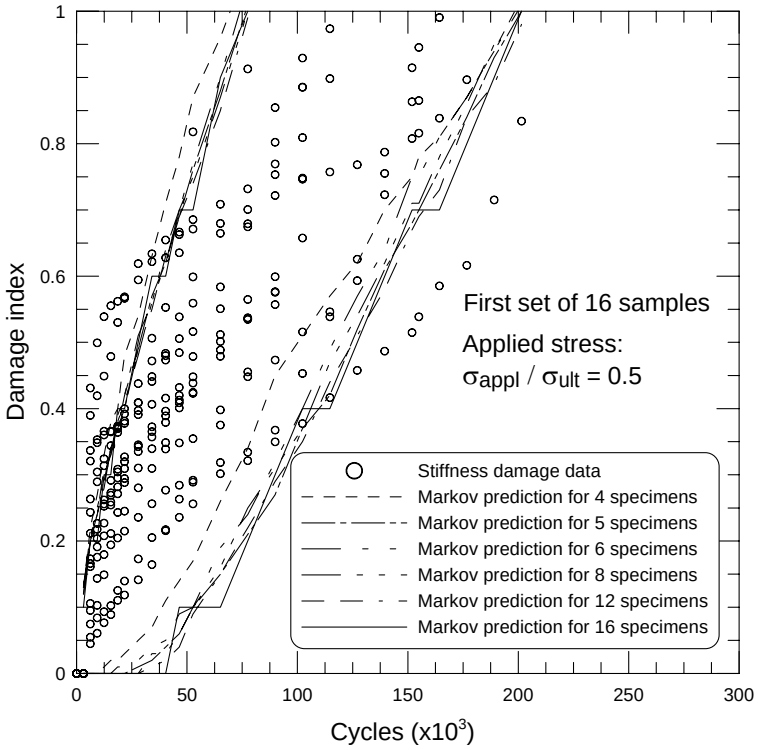

Fig. 4.10. Markov chain predictions in the form of upper and lower bounds over fatigue life for stiffness measurements of 16 specimens subjected to 50% stress level

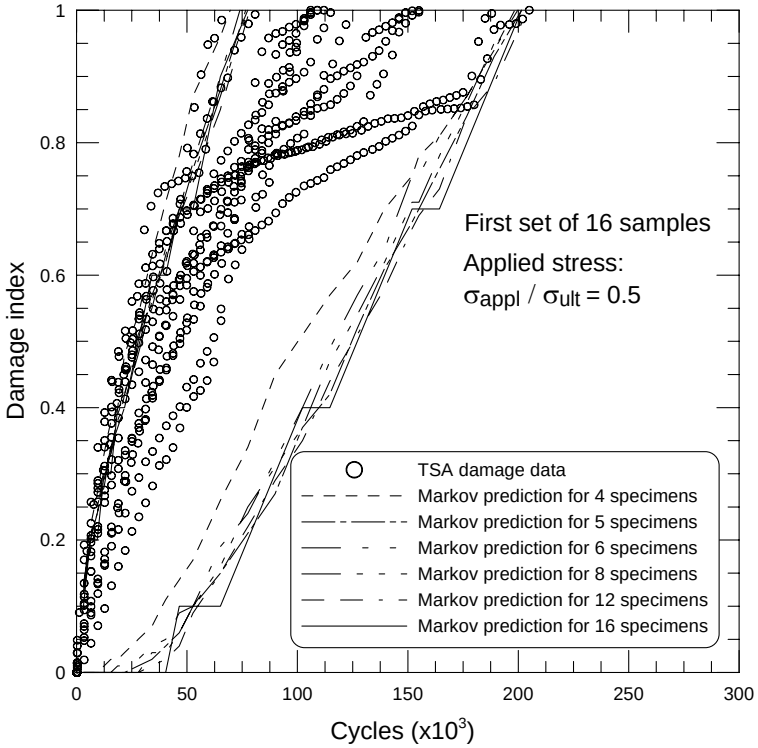

Fig. 4.11. Markov chain predictions in the form of upper and lower bounds over fatigue life for TSA measurements of 16 specimens subjected to 50% stress level

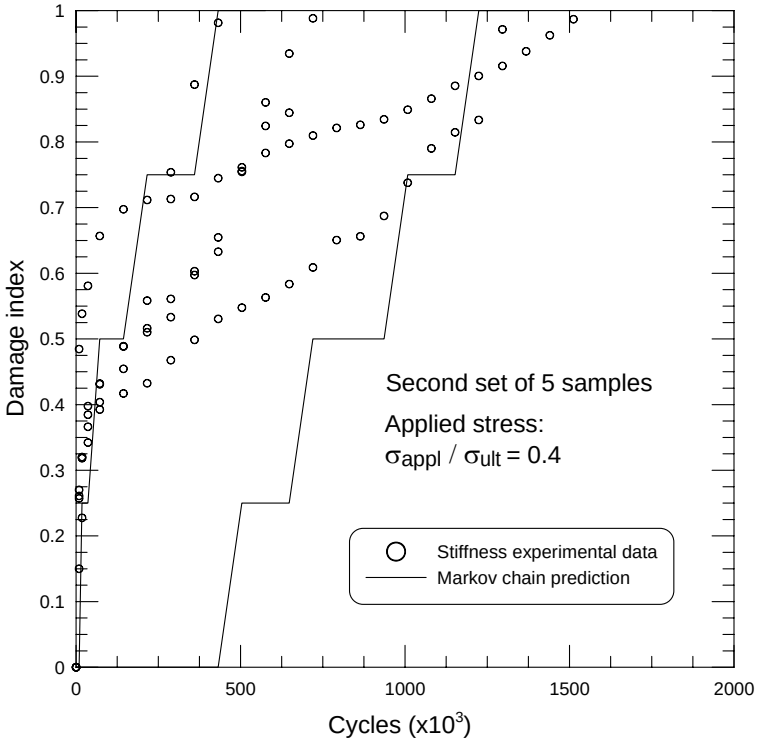

Fig. 4.12. Markov chain predictions in the form of upper and lower bounds over fatigue life for stiffness measurements of 5 specimens subjected to 40% stress level

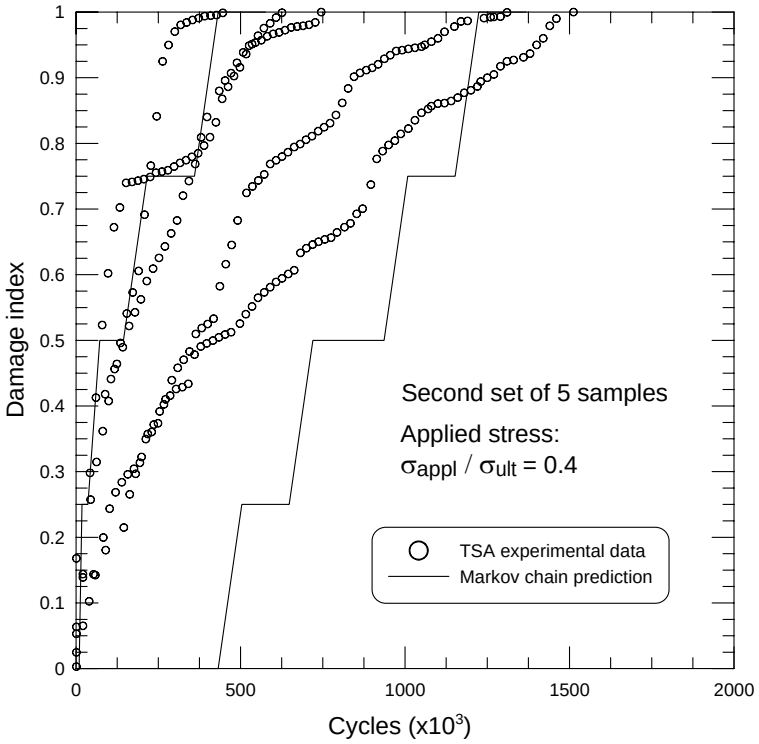

Fig. 4.13. Markov chain predictions in the form of upper and lower bounds over fatigue life for TSA measurements of 5 specimens subjected to 40% stress level

4.4 Stochastic S-N Curve Utilizing Calibrated Markov Chain Models

In this section, we utilize the previously calibrated MCMs to generate stochastic S-N curves when given a limited number of fatigue tests. Suppose we are given a limited number of S-N data sets (k) where failure occurs at different fatigue cycles but at the same applied stress level. We proceed by using a (k-1) order polynomial to generate an S-N curve fitting the mean k-values of the sets. The associated S-N bounds representing scattered data or variance can now be constructed. Figure 4.14 shows a schematic illustrating the proposed algorithm to generate the stochastic S-N curves. The stochastic S-N construction procedure is implemented using the algorithm detailed in Fig. 4.15. The algorithm iteratively finds the distribution over a general fatigue cycle, $N_f^{(i)}$, from previously calibrated MCMs. The code developed marches over increasing $N_f^{(i)}$ values. At a given (i, j) iteration, a variance, $VAR^{(i,\,j)}$ of the cycles to failure, is used based on previously converged value for $N_f^{(i-1)}$ as shown in Fig. 4.15. The MCM described in Eq. (4.1) is utilized, and a new mean cycles to failure, $N_f^{MCM\,(AVG)}$, is calculated from the MCM distribution for each inner iteration (j). If the difference between the $N_f^{MCM\,(AVG)}$ and the input $N_f^{(i)}$ is within a preset tolerance, the current j-iteration converges, and then we proceed to the next i-step. If no convergence is achieved, we iterate by increasing the variance to $VAR^{(i,\,j+1)}$, and proceed until the convergence is achieved. Once the j-iteration has converged for an i-step, $N_f^{(i)}$, the trial variance, $VAR^{(i+1,\,j)}$, is calculated based on the previously converged variance. The procedure is executed for $i_{\max}$ step values through the entire fatigue cycles, $N_f^{(i=i_{\max})}$, in order to complete the stochastic S-N curve.

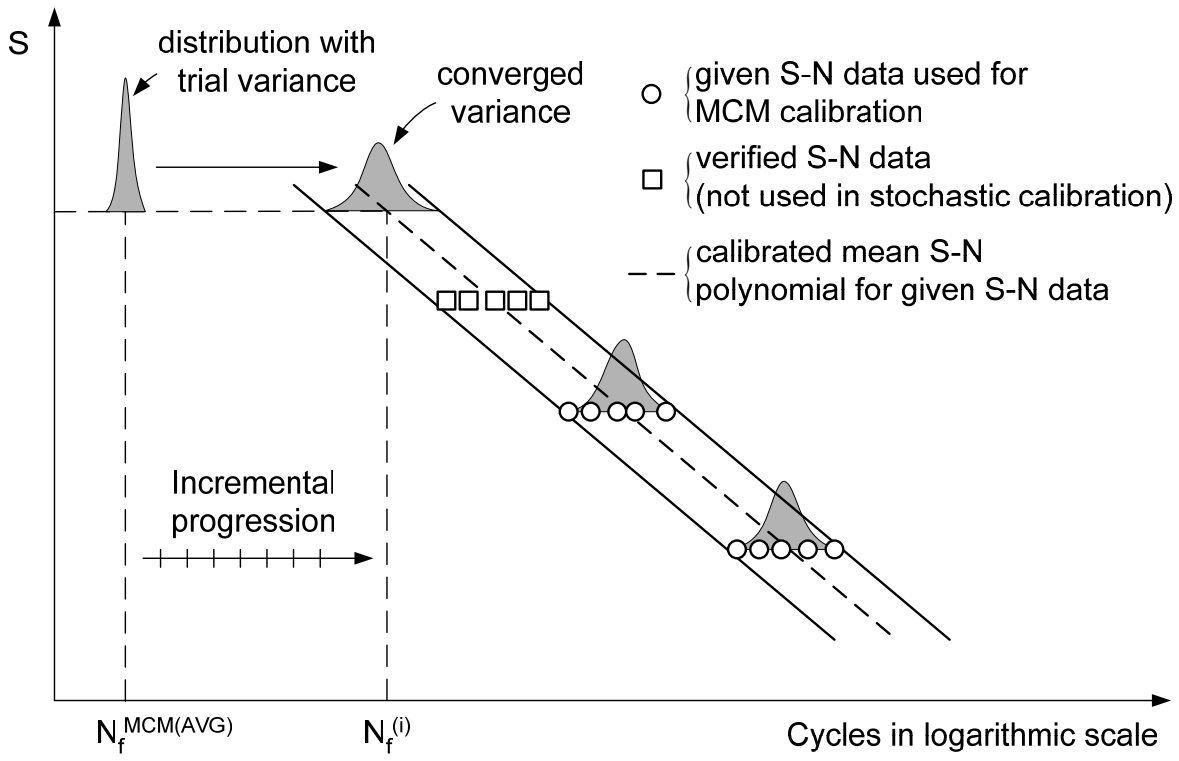

Fig. 4.14. Schematic representation of the construction of stochastic S-N curves

Step 1. Initialize variables

INITIALIZE $N_f^{(0)}$, ΔN_f, $VAR^{(0,0)}$, ΔVAR, ΔX – duty cycle, $j = 0$,

$i_{\max} = N_f^{(\text{final})} / \Delta N_f$

Step 2. Find convergent MCM variance for each *i*-step

LOOP $i = 1, 2, 3, \cdots, i_{\max}$

$N_f^{(i)} = N_f^{(i-1)} + \Delta N_f$

$VAR^{(i,j)} = VAR^{(i-1,\,j)}$

Step 3. *j*-iterations for variance within current *i*-step

$j = j + 1$

$VAR^{(i,j)} = VAR^{(i,j-1)} + \Delta VAR$

CALCULATE p, q USING Eq. (4.14)

INITIALIZE X

$m_f = \text{Integer}\left(N_f^{(i)} / \Delta X \right)$

LOOP $m = 1, 2, 3, \ldots, m_f$

$X = X + \Delta X$

$\pi_X^{(m)} = \pi_0 P^X$

CALCULATE $N_f^{MCM\,(AVG)}$, $N_f^{MCM\,(MAX)}$, $N_f^{MCM\,(MIN)}$

IF $\left| N_f^{MCM\,(AVG)} - N_f^{(i)} \right| > \text{TOL}$, THEN GOTO Step 3

ELSE GOTO Step 2

Fig. 4.15. Proposed algorithm for generating stochastic S-N curves using previously calibrated MCMs

Two different fatigue experiments with applied stress levels, 50% and 40% of the ultimate stress, have been conducted for several composite laminates until serviceability failure occurs, previously described in Section 4.2. The stochastic S-N curve with scattered data for serviceability can now be constructed using the newly proposed algorithm. The averages in the region for cycles to failure without experimental data can be obtained using a logarithmic equation that fits the mean of the cycles to failure for both the 50%

and 40% stress levels. Therefore, this logarithmic equation calibrated from experiments can be assumed to be valid for the average cycles to failure at different applied stresses. The stochastic S-N curve, shaded region shown in Fig. 4.16, is generated from the algorithm using the calibrated MCM from the experiments with 50% and 40% applied stress levels conducted in this study. The first order logarithmic equation representing the average fatigue cycles to failure is:

$$S = -36.1 \times \log(N_f) + 344.8 \quad \text{(MPa)} \tag{4.18}$$

where S is the applied stress and N_f is the average cycles to failure.

The average of this stochastic S-N curve prediction, $N_f^{MCM(AVG)}$, obtained from the proposed stochastic algorithm converges to N_f in Eq. (4.18). The shaded region provides a good estimate for the bounds over the fatigue cycles to failure under various stress levels.

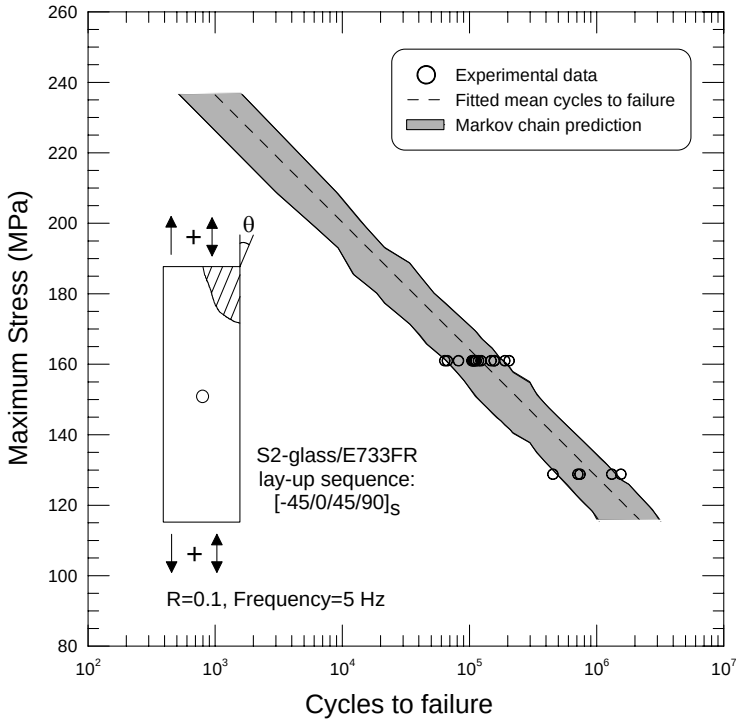

Fig. 4.16. Constructed stochastic S-N data based on two limited data sets and previously calibrated MCM for the set with 50% stress level

Next, the stochastic S-N method is applied to other composite laminates with different lay-ups from test results available in the literature (Mandell and Samborsky, 1997). Their lay-up sequences and material properties are summarized in Table 4.5. The presented fatigue experiments are conducted under a stress ratio of 0.1 and various frequencies.

Table 4.5. Adopted material properties and lay-up sequences of composite laminates (Mandell and Samborsky, 1997)

Fiber/Matrix	Ply configuration	V_F (FVF) (%)	σ_{ult} (MPa)	E_{11} (GPa)	E_{22} (GPa)
E-Glass/Polyester	$[0]_5$	39	773	31.0	7.24
E-Glass/Polyester	$[0]_7$	51	1,187	38.9	-
E-Glass/Polyester	$[0/\pm45/0]_s$	36	661	23.6	-

Figure 4.17 shows the stochastic S-N curve generated for E-Glass/Polyester laminate with a $[0]_5$ lay-up. A fourth-order logarithmic equation is fitted for the average cycles to failure in the five sets of experiments with different applied stresses. This logarithmic equation can be expressed as:

$$S = -3\times\log(N_f)^4 + 68\times\log(N_f)^3 - 481\times\log(N_f)^2 + 1372\times\log(N_f) + 745 \quad \text{(MPa)} \tag{4.19}$$

The MCM is recalibrated for the E-Glass/Polyester composite. The fatigue data set with applied stress of 552 MPa is used for this purpose. Similar to the previous composite system, eleven damage states are obtained for the MCM calibration. Next, the stochastic *S-N* algorithm as described in Fig. 4.14 is utilized. The stochastic S-N bounds are found to effectively converge around the forth order logarithmic equation representing the average cycles to failure. As a result, the stochastic S-N curve bounds have good agreement with the experimental data.

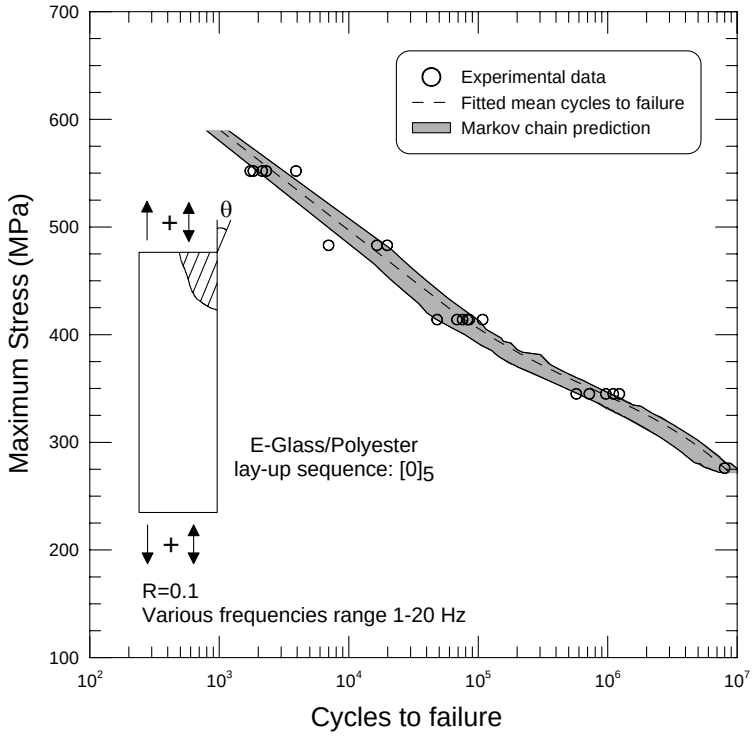

Fig. 4.17. Constructed stochastic S-N data based on five limited data sets and previously calibrated MCM for the set with applied stress of 552 MPa

Figure 4.18 shows the Markov chain prediction for E-Glass/Polyester with a $[0]_7$ lay-up. The damage state of 10 steps is calibrated from the experiments (522 MPa) with this material system since it has a different fiber volume fraction. The second order logarithmic equation fitted to the average cycles to failure under maximum stresses, 345, 414, and 522 MPa, can be expressed as:

$$S = 19.3 \times \log(N_f)^2 - 311.9 \times \log(N_f) + 1524.8 \quad \text{(MPa)} \tag{4.20}$$

The fatigue cycles to failure under a maximum stress of 690 and 827 MPa are not used in the fitting of Eq. (4.20) in order to be used in the verification of the stochastic S-N. These two fatigue data sets follow the overall stochastic S-N curve. This indicates that both the Markov chain prediction and the stochastic S-N approach have good agreement with the fatigue cycles to failure and can provide an effective fatigue damage model.

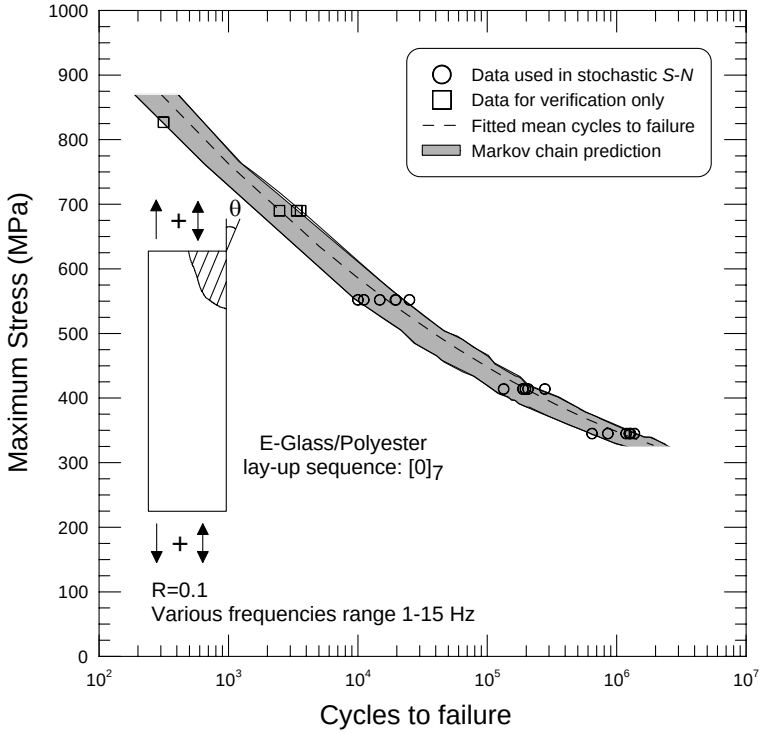

Fig. 4.18. Constructed stochastic S-N data based on three limited data sets and previously calibrated MCM for the set with applied stress of 552 MPa

Finally, Fig. 4.19 shows the Markov chain prediction and the fatigue experiments for E-Glass/Polyester with a $[0/\pm45/0]_s$ lay-up. The MCM total damage state (12 steps) is calibrated from the data set corresponding to the 414 MPa stress level. Because only two different maximum stresses are available, a first order logarithmic equation is used to fit the average cycles to failure for the two sets of experiments. The logarithmic equation can be expressed as:

$$S = -65.9 \times \log(N_f) + 677.5 \quad \text{(MPa)} \tag{4.21}$$

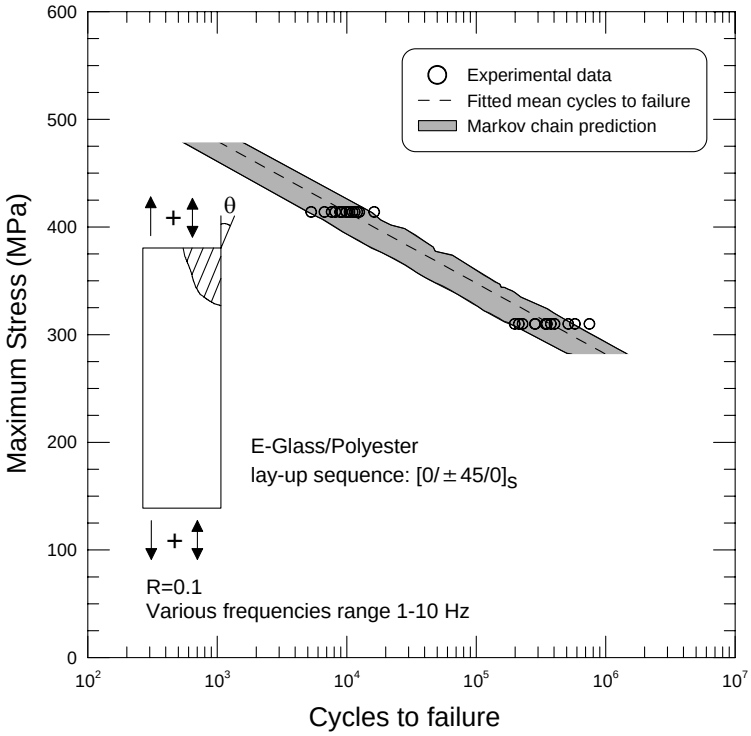

Fig. 4.19. Constructed stochastic S-N data based on two limited data sets and previously calibrated MCM for the set with applied stress of 414 MPa

CHAPTER 5

CONCLUSIONS AND FUTURE RESEARCH

New experimental and analytical methods are developed to investigate the deformation and damage behavior of composite materials utilizing TSA techniques. The first part of this thesis demonstrates and validates the derivations for two new quantitative TSA methods that correlate the measured infrared signal with the sum of in-plane strains for orthotropic composites with and without transversely-isotropic surface coating layers. The second part of this study employs the newly developed quantitative TSA methods in order to calculate the mixed-mode SIFs for cracks in an orthotropic medium subjected to off-axis loadings. The SIFs from the experimental TSA methods are compared to numerical SIFs values calculated using two computational models: the VCCT and a general FE crack-tip strain field solutions. The third part of this study develops a new stochastic S-N fatigue life model for composites using the Markov chain model with damage metrics from the TSA methods. This chapter presents some major conclusions followed by further research recommendations.

5.1 Conclusions

Two new quantitative TSA methods are developed and verified by comparing experiments with FE methods and Savin's elasticity solution. First, thick-section pultruded composites with transversely isotropic surface layers with the ESE(T) geometry are used for TSA experiments and FE verification. The pultruded composites are cut with four material angles with respect to loading directions in order to generate material anisotropy. This material system requires a thermo-mechanical coefficient calibrated from a uniform

straight coupon to map the measured IR signal emitted from the ESE(T) specimens into sum of in-plane strains. The sum of in-plane strains obtained from FE models are compared with the TSA experiments. The results show good agreement between TSA experiments and FE simulations for the four cases.

Next, the TSA formulations have been successfully derived for orthotropic composite materials without surface coating layers. The quantitative TSA method can map the measured IR signal with the sum of in-plane strains via two calibrated thermomechanical coefficients. Orthotropic composite laminates made from S2-glass/E733FR unidirectional layers and a $[0_5/90/0_5]$ lay-up sequence are used. An open-hole specimen with a 30° off-axis material angle is used for the comparison among TSA experiment, FE simulation, and Savin's elasticity solution. The simulated IR signal obtained from the FE method and Savin's solution has a good correlation with the TSA experiment. The S2-glass/E733FR laminates from the same monolithic panel are also cut into the ESE(T) fractured geometry with four material angles. The full-field IR signal simulated form the FE models via calibrations show good agreement with that obtained from TSA experiments.

A new quantitative TSA-based method has also been developed for experimentally measured mixed-mode SIFs in cracked composite materials. The required coefficients for calculating the mixed-mode SIFs are obtained from fitting-correlating the full-filed IR data or the sum of in-plane strains with Lekhnitskii's polynomial expansions using the least-squares method. The previous ESE(T) pultruded and S2-glass/E733FR composites with four different material orientations are used to generate the mixed-mode SIFs. Measured mode-I SIFs using Lekhnitskii's solution coupled with the experimental

TSA method have good agreement with numerical values determined from the well-known VCCT-FE method and Lekhnitskii's solution coupled with FE. However, mode-II SIF values are relatively small and very sensitive to the crack tip geometry and location, so the uncertainties of the crack tip location and/or friction at crack tip could have larger effect on the mode-II SIFs.

A new stochastic S-N fatigue damage model has been proposed. The Markov chain models are successfully employed to predict the fatigue damage evolution in composite laminates using both TSA techniques and a mechanical gauge (extensometer). Notched composite laminated specimens subjected to different stress levels are investigated under fatigue loading using stiffness and TSA area degradation metrics. Three different composite laminate lay-ups obtained from the literature are also investigated using the proposed stochastic S-N curve approach. The results for the TSA and stiffness experiments show the Markov chain models can effectively describe the fatigue damage evolution for specific constant amplitude with maximum stress level. The proposed stochastic S-N approach also provides a classical S-N curve with variability due to the nature of fatigue. Markov chain theory combined with the proposed approach can reduce the need for a massive number of fatigue tests under various stress levels while maintaining satisfactory predictions. This study also presents a new remote sensing and non-destructive evaluation technique combined with new statistical approaches to reduce the number of lab tests in developing inspection protocol for preventing serviceability failures due to fatigue in composite structures. The new stochastic S-N model is shown to be predictive and can provide reliable S-N data for the relatively large range of fatigue cycles.

5.2 Future Research

An IR-TSA experimental method for mixed-mode SIFs in composite materials has been established and verified with FE simulations. The values obtained between IR-TSA and FE methods exhibit some larger errors. The sharpness/geometry and actual location of the crack tip can affect the accuracy of the SIFs. More accurate SIFs may be accomplished by the following methods:

1. The actual location of the crack tip in the composite specimen is not well-defined. The damage at the crack tip can further complicate the analysis of the location. A future research on the IR-TSA response in the near crack tip region can help define the crack tip location in experiments.
2. The sharpness/geometry of the crack tip is not identical in the experiments and FE simulations. A highly accurate machine can be used to create refined composite samples or a new VCCT in FE modeling to account for a blunt crack tip can be developed.

The propagation of an angled crack can occur when the loading is a combination of tensile and shear stresses. This loading condition is especially common for an anisotropic medium. Once the stress field at the crack tip of an anisotropic medium is well-defined, the local mixed-mode SIFs at the tip of the kink can be further investigated. Therefore, the propagation path of the crack in an anisotropic medium subjected to mixed-mode loadings can be predicted.

The proposed new stochastic S-N curve is developed solely based on Markov chain model calibrated from experimental data. A more sophisticated stochastic model incorporating failure criterion such as the Tsai-Wu failure criterion can be implemented so that fewer fatigue tests are required to obtain the stochastic S-N curve. The failure cri-

teria and statistical approaches can be also used in FE simulations in order to verify or simulate fatigue data. The fatigue data generated by the Markov chain model or FE simulations can further be used in reliability evaluations.

This study used the stiffness and TSA-based damage area metrics for stochastic S-N curve evaluation. The fatigue damage evolution monitored by the TSA techniques can be also used for various material or structural systems such as composite shear lap joints. The debonding front in the shear lap region creates stress concentrations that can be detected by IR-TSA and therefore a new damage metric (e.g. debonding front of the lap joint) can be used for evaluation.

APPENDIX A

LEKHNITSKII'S ELASTICITY SOLUTION FOR ANISOTROPIC MATERIALS

This appendix comprehends the Lekhnitskii's complex variable elasticity solution for anisotropic plates. The first section introduces Lekhnitskii's general solution for the stress functions for an anisotropic plate subjected to remote stresses. The second section introduces Savin's solution derived from Lekhnitskii's solution to calculate the stress field around an elliptical hole in anisotropic materials. The third section presents the formulations for the stress field in the vicinity of the crack tip and the SIFs at the crack tip.

A.1 Lekhnitskii's Solution for Anisotropic Materials

Consider the static state in a small rectangular block of material; the equilibrium equation without body force can be expressed as:

$$\frac{\partial \sigma_{ij}}{\partial x_j} = 0 \tag{A.1}$$

The compatibility equation can be expressed as:

$$\delta_{pks} \frac{\partial}{\partial x_k} \left(\frac{\partial \varepsilon_{sj}}{\partial x_i} - \frac{\partial \varepsilon_{si}}{\partial x_j} \right) = 0 \tag{A.2}$$

For the plane stress condition, the following stresses and strains are zero.

$$\sigma_{zz} = \sigma_{zx} = \sigma_{zy} = 0$$
$$\varepsilon_{zx} = \varepsilon_{zy} = 0$$

Consider the generalized Hooke's law in an anisotropic material; the in-plane strains can be expressed as:

$$\varepsilon_{xx} = a_{11}\sigma_{xx} + a_{12}\sigma_{yy} + a_{16}\sigma_{xy} \tag{A.3a}$$

$$\varepsilon_{yy} = a_{12}\sigma_{xx} + a_{22}\sigma_{yy} + a_{26}\sigma_{xy} \tag{A.3b}$$

$$2\varepsilon_{xy} = a_{16}\sigma_{xx} + a_{26}\sigma_{yy} + a_{66}\sigma_{xy} \tag{A.3c}$$

where the a_{ij} terms are material compliances.

The Airy stress function can be expressed as:

$$\sigma_{xx} = \frac{\partial^2 \phi}{\partial y^2} \tag{A.4a}$$

$$\sigma_{yy} = \frac{\partial^2 \phi}{\partial x^2} \tag{A.4b}$$

$$\sigma_{xy} = -\frac{\partial^2 \phi}{\partial x \partial y} \tag{A.4c}$$

where ϕ is a potential function that can be solved via boundary conditions.

Substituting Eqs. (A.4) into Eqs. (A.3) yields:

$$\varepsilon_{xx} = a_{11}\frac{\partial^2 \phi}{\partial y^2} + a_{12}\frac{\partial^2 \phi}{\partial x^2} - a_{16}\frac{\partial^2 \phi}{\partial x \partial y} \tag{A.5a}$$

$$\varepsilon_{yy} = a_{21}\frac{\partial^2 \phi}{\partial y^2} + a_{22}\frac{\partial^2 \phi}{\partial x^2} - a_{26}\frac{\partial^2 \phi}{\partial x \partial y} \tag{A.5b}$$

$$2\varepsilon_{xy} = a_{16}\frac{\partial^2 \phi}{\partial y^2} + a_{26}\frac{\partial^2 \phi}{\partial x^2} - a_{66}\frac{\partial^2 \phi}{\partial x \partial y} \tag{A.5c}$$

Substituting Eqs. (A.5) into the in-plane strains (*x*-*y* plane) in Eqs. (A.2) and collecting terms yield:

$$a_{11}\frac{\partial^4 \phi}{\partial y^4} - 2a_{16}\frac{\partial^4 \phi}{\partial x \partial y^3} + \left(2a_{12} + a_{66}\right)\frac{\partial^4 \phi}{\partial x^2 \partial y^2} - 2a_{26}\frac{\partial^4 \phi}{\partial x^3 \partial y} + a_{22}\frac{\partial^4 \phi}{\partial x^4} = 0 \tag{A.6}$$

The general solution for Eq. (A.6) is in the form $\phi(x, y) = F(x + \mu \cdot y)$, where μ is a complex variable. Therefore, Eq. (A.6) becomes a characteristic equation expressed as:

$$a_{11} \cdot \mu^4 - 2a_{16} \cdot \mu^3 + \left(2a_{12} + a_{66}\right) \cdot \mu^2 - 2a_{26} \cdot \mu + a_{22} = 0 \tag{A.7}$$

The characteristic equation has four complex roots, and the roots always occur in conju-

gate pairs. The roots can be expressed as:

$$\mu_1 = \alpha_1^* + i\beta_1^* \tag{A.8a}$$
$$\mu_2 = \alpha_2^* + i\beta_2^* \tag{A.8b}$$
$$\mu_3 = \overline{\mu}_1 \tag{A.8c}$$
$$\mu_4 = \overline{\mu}_2 \tag{A.8d}$$

The general solution of ϕ is given by:

$$\phi(x,y) = F_1(x+\mu_1 \cdot y) + F_2(x+\mu_2 \cdot y) + F_3(x+\overline{\mu}_1 \cdot y) + F_4(x+\overline{\mu}_2 \cdot y) \tag{A.9}$$

Because ϕ is real, Eq. (A.9) can be written as:

$$\phi(x,y) = 2\,\mathrm{Re}\left[F_1(z_1) + F_2(z_2)\right] \tag{A.10}$$

where $z_1 = x + \mu_1 \cdot y$, $z_2 = x + \mu_2 \cdot y$

The in-plane stresses can be expressed from Eqs. (A.4):

$$\sigma_{xx} = 2\,\mathrm{Re}[\mu_1^2 \cdot F_1'' + \mu_2^2 \cdot F_2''] \tag{A.11a}$$
$$\sigma_{yy} = 2\,\mathrm{Re}[F_1'' + F_2''] \tag{A.11b}$$
$$\sigma_{xy} = -2\,\mathrm{Re}[\mu_1 \cdot F_1'' + \mu_2 \cdot F_2''] \tag{A.11c}$$

Substituting Eq. (A.10) into Eqs. (A.5) and integrating with respect to *x* and *y* yield the displacements:

$$u_{xx} = 2\,\mathrm{Re}\left[p_1 \cdot F_1' + p_2 \cdot F_2'\right] \tag{A.12a}$$
$$u_{yy} = 2\,\mathrm{Re}\left[q_1 \cdot F_1' + q_2 \cdot F_2'\right] \tag{A.12b}$$

where the rigid-body motion term is dropped and

$$p_i = a_{11}\mu_i^2 - a_{16}\mu_i + a_{12} \tag{A.13a}$$
$$q_i = a_{12}\mu_i - a_{26} + \frac{a_{22}}{\mu_i} \tag{A.13b}$$

Let $\Phi_1(z_1) = \dfrac{dF_1}{dz_1}$, $\Phi_2(z_2) = \dfrac{dF_2}{dz_2}$; the stresses and the displacements in Eqs. (A.11) and

(A.12) can be rewritten as:

$$\sigma_{xx} = 2\,\mathrm{Re}[\mu_1^2 \cdot \Phi_1' + \mu_2^2 \cdot \Phi_2'] \tag{A.14a}$$

$$\sigma_{yy} = 2\,\mathrm{Re}[\Phi_1' + \Phi_2'] \tag{A.14b}$$

$$\sigma_{xy} = -2\,\mathrm{Re}[\mu_1 \cdot \Phi_1' + \mu_2 \cdot \Phi_2'] \tag{A.14c}$$

$$u_{xx} = 2\,\mathrm{Re}[p_1 \cdot \Phi_1 + p_2 \cdot \Phi_2] \tag{A.15a}$$

$$u_{yy} = 2\,\mathrm{Re}[q_1 \cdot \Phi_1 + q_2 \cdot \Phi_2] \tag{A.15b}$$

A.2 Savin's Solution for Stresses around an Elliptical Hole in Anisotropic Materials

Consider an infinite anisotropic plane subjected to a uniform remote traction, *p*, with an angle α from the x-axis (shown in Fig. A.1).

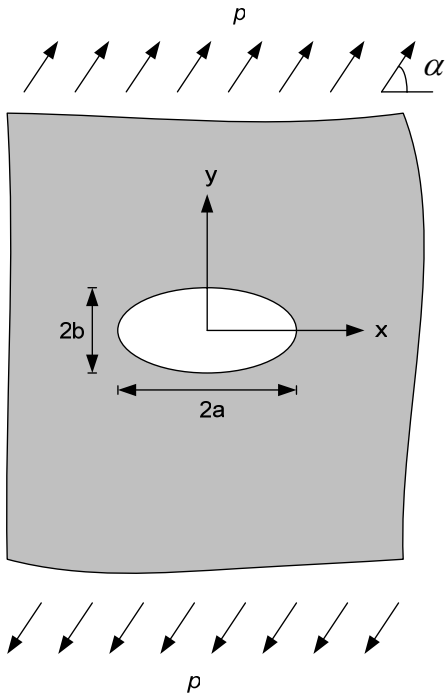

Fig. A.1. Infinite anisotropic open-hole plate subjected to a uniform tension

The potential functions, Φ_1 and Φ_2, obtained form Savin's solution can be expressed as:

$$\Phi_1(z_1) = B * z_1 + \varphi_0(z_1) \tag{A.16a}$$

$$\Phi_2(z_2) = (B'^* + iC'^*)z_2 + \psi_0(z_2) \tag{A.16b}$$

Since it is traction free on the surface around the hole, we can express the tractions as:

$$f_1 = \int Y_n ds = 2\,\mathrm{Re}\left[\Phi_1 + \Phi_2\right] = 0 \tag{A.17a}$$

$$f_2 = \int X_n ds = -2\,\mathrm{Re}\left[\mu_1 \cdot \Phi_1 + \mu_2 \cdot \Phi_2\right] = 0 \tag{A.17b}$$

The coefficients can be solved as:

$$B^* = p\frac{\cos^2\alpha + (\alpha_2^2 + \beta_2^2)\sin^2\alpha + \alpha_2 \sin 2\alpha}{2[(\alpha_2 - \alpha_1)^2 + (\beta_2^2 - \beta_1^2)]} \tag{A.18a}$$

$$B'^* = p\frac{[(\alpha_1^2 - \beta_1^2) - 2\alpha_1\alpha_2]\sin^2\alpha - \cos^2\alpha - \alpha_2 \sin 2\alpha}{2[(\alpha_2 - \alpha_1)^2 + (\beta_2^2 - \beta_1^2)]} \tag{A.18b}$$

$$C'^* = p\left\{\frac{(\alpha_1 - \alpha_2)\cos^2\alpha + [\alpha_2(\alpha_1^2 - \beta_1^2) - \alpha_1(\alpha_2^2 - \beta_2^2)]\sin^2\alpha}{2[(\alpha_2 - \alpha_1)^2 + (\beta_2^2 - \beta_1^2)]} + \frac{[\alpha_1(\alpha_1^2 - \beta_1^2) - (\alpha_2^2 - \beta_2^2)]\sin\alpha\cos\alpha}{2[(\alpha_2 - \alpha_1)^2 + (\beta_2^2 - \beta_1^2)]}\right\} \tag{A.18c}$$

$$\varphi_0(z_1) = -\frac{ip(a - i\mu_1 b)}{4(\mu_1 - \mu_2)}\left\{\frac{b(\mu_2 \sin 2\alpha + 2\cos^2\alpha) + ia(2\mu_2 \sin^2\alpha + \sin 2\alpha)}{z_1 + \sqrt{z_1^2 - (a^2 + \mu_1^2 b^2)}}\right\} \tag{A.18d}$$

$$\psi_0(z_2) = \frac{ip(a - i\mu_2 b)}{4(\mu_1 - \mu_2)}\left\{\frac{b(\mu_1 \sin 2\alpha - 2\cos^2\alpha) + ia(2\mu_1 \sin^2\alpha + \sin 2\alpha)}{z_2 + \sqrt{z_2^2 - (a^2 + \mu_2^2 b^2)}}\right\} \tag{A.18e}$$

Substituting Eqs. (A.16) into Eqs. (A.14) yields:

$$\sigma_x = p\cos^2\alpha + 2\,\mathrm{Re}[\mu_1^2\varphi_0'(z_1) + \mu_2^2\psi_0'(z_2)] \tag{A.19a}$$

$$\sigma_y = p\sin^2\alpha + 2\,\mathrm{Re}[\varphi_0'(z_1) + \psi_0'(z_2)] \tag{A.19b}$$

$$\tau_{xy} = p\sin\alpha\cos\alpha - 2\,\mathrm{Re}[\mu_1\varphi_0'(z_1) + \mu_2\psi_0'(z_2)] \tag{A.19c}$$

Therefore, the stress field around an elliptical hole in an anisotropic plate subjected to

remote stresses and be determined by Eqs. (A.19).

A.3 Lekhnitskii's Anisotropic Solution for SIFs at a Crack Tip

The potential functions in Lekhnitskii's solution can be expressed as polynomials to calculate the stress field in the crack tip vicinity in an anisotropic plate. The polynomials can be expressed as:

$$\Phi_1(z_1) = \sum_{j=1}^{n} b_j z_1^j \tag{A.20a}$$

$$\Phi_2(z_2) = \sum_{j=1}^{n} c_j z_2^j \tag{A.20b}$$

where the b_j and c_j are complex constants in the following form:

$$b_j = \beta_j + i\beta_{j+n} \tag{A.21a}$$

$$c_j = \gamma_j + i\gamma_{j+n} \tag{A.21b}$$

For the cracked anisotropic plate subjected to remote stresses shown in Fig. A.2, the tractions are free on the crack surface. The tractions can be expressed as:

$$f_1 = \int Y_n ds = 2\,\mathrm{Re}\left[\Phi_1 + \Phi_2\right] = 0 \tag{A.22a}$$

$$f_2 = \int X_n ds = -2\,\mathrm{Re}\left[\mu_1 \cdot \Phi_1 + \mu_2 \cdot \Phi_2\right] = 0 \tag{A.22b}$$

Substituting Eqs. (A.20) into Eqs. (A.22) yields:

$$\sum_{j=1}^{n} \mathrm{Re}[b_j z_1^j + c_j z_2^j] = 0 \tag{A.23a}$$

$$\sum_{j=1}^{n} \mathrm{Re}[\mu_1 b_j z_1^j + \mu_2 c_j z_2^j] = 0 \tag{A.23b}$$

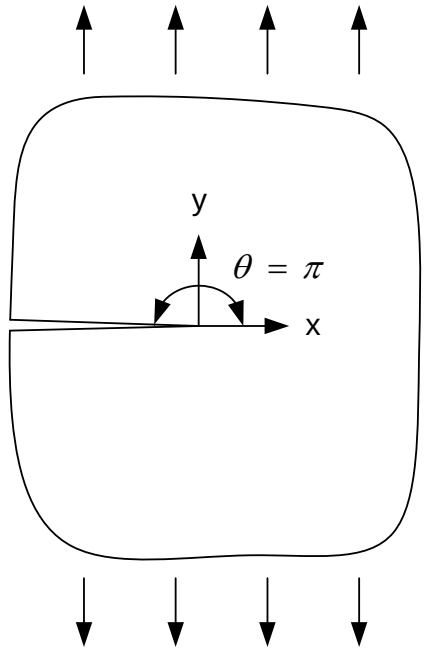

Fig. A.2. Infinite anisotropic cracked plate subjected to remote stresses

The variable, z_j, in the potential functions can be expressed in the polar coordinates:

$$z_k = \lambda_k e^{i\theta_k} = \lambda_k[\cos(\theta_k) + i \cdot \sin(\theta_k)] \tag{A.24}$$

where $\theta = \pi$ on the crack surface.

Substituting Eq. (A.24) into Eqs. (A.23) to obtain c_j and then the potential functions can be expressed as:

$$\Phi_1(z_1) = \sum_{j=1}^{n} (\beta_j + i\beta_{j+n}) z_1^j \tag{A.25a}$$

$$\Phi_2(z_2) = \sum_{j=1}^{n} (M_{1j}\beta_j + M_{2j}\beta_{j+n}) z_2^j \tag{A.25b}$$

where

$$M_{1j} = \frac{-\beta_1^*}{\beta_2^*} \text{ and } M_{2j} = \frac{\alpha_2^* - \alpha_1^*}{\beta_2^*} - i \text{ for odd } j \tag{A.26a}$$

$$M_{1j} = -1 + i\frac{\alpha_1^* - \alpha_2^*}{\beta_2^*} \text{ and } M_{2j} = -i\frac{\beta_1^*}{\beta_2^*} \text{ for even } j \tag{A.26b}$$

Substituting Eqs. (A.26) into Eqs. (A.14) yields the stress and displacement functions:

$$\sigma_x = \sum_{j=1}^{2n} A_j(z_1, z_2)\beta_j \tag{A.27a}$$

$$\sigma_y = \sum_{j=1}^{2n} B_j(z_1, z_2)\beta_j \tag{A.27b}$$

$$\sigma_{xy} = \sum_{j=1}^{2n} C_j(z_1, z_2)\beta_j \tag{A.27c}$$

$$u = \sum_{j=1}^{2n} D_j(z_1, z_2)\beta_j \tag{A.27d}$$

$$\mathrm{v} = \sum_{j=1}^{2n} E_j(z_1, z_2)\beta_j \tag{A.27e}$$

where

$$A_j(z_1, z_2) = j\,\mathrm{Re}\left\{\mu_1^2 z_1^{(j-2)/2} + \mu_2^2 M_{1j} z_2^{(j-2)/2}\right\} \tag{A.28a}$$

$$A_{j+n}(z_1, z_2) = j\,\mathrm{Re}\left\{i\cdot\mu_1^2 z_1^{(j-2)/2} + \mu_2^2 M_{2j} z_2^{(j-2)/2}\right\} \tag{A.28b}$$

$$B_j(z_1, z_2) = j\,\mathrm{Re}\left\{z_1^{(j-2)/2} + M_{1j} z_2^{(j-2)/2}\right\} \tag{A.28c}$$

$$B_{j+n}(z_1, z_2) = j\,\mathrm{Re}\left\{i\cdot z_1^{(j-2)/2} + M_{2j} z_2^{(j-2)/2}\right\} \tag{A.28d}$$

$$C_j(z_1, z_2) = -j\,\mathrm{Re}\left\{\mu_1 z_1^{(j-2)/2} + \mu_2 M_{1j} z_2^{(j-2)/2}\right\} \tag{A.28e}$$

$$C_{j+n}(z_1, z_2) = -j\,\mathrm{Re}\left\{i\cdot\mu_1 z_1^{(j-2)/2} + \mu_2 M_{2j} z_2^{(j-2)/2}\right\} \tag{A.28f}$$

$$D_j(z_1, z_2) = 2\,\mathrm{Re}\left\{p_1 z_1^{j/2} + p_2 M_{1j} z_2^{j/2}\right\} \tag{A.28g}$$

$$D_{j+n}(z_1, z_2) = 2\,\mathrm{Re}\left\{i\cdot p_1 z_1^{j/2} + p_2 M_{2j} z_2^{j/2}\right\} \tag{A.28h}$$

$$E_j(z_1, z_2) = 2\,\mathrm{Re}\left\{q_1 z_1^{j/2} + q_2 M_{1j} z_2^{j/2}\right\} \tag{A.28i}$$

$$E_{j+n}(z_1, z_2) = 2\,\mathrm{Re}\left\{i\cdot q_1 z_1^{j/2} + q_2 M_{2j} z_2^{j/2}\right\} \tag{A.28j}$$

Sih et at. (1965) derived the SIFs at crack tip for plane anisotropic media. The SIFs can be expressed as:

$$K_I + \frac{K_{II}}{\mu_2} = -\sqrt{2}\left(\frac{\mu_1}{\mu_2} - 1\right)\lim_{z_1\to 0}\Phi_1'(z_1) = -\sqrt{2}\left(\frac{\mu_1}{\mu_2} - 1\right)\cdot b_1 \tag{A.29a}$$

$$K_I + \frac{K_{II}}{\mu_1} = \sqrt{2}\left(1 - \frac{\mu_2}{\mu_1}\right)\lim_{z_2\to 0}\Phi_2'(z_2) = \sqrt{2}\left(1 - \frac{\mu_2}{\mu_1}\right)\cdot c_1 \tag{A.29b}$$

By solving Eqs. (A.29) and taking the real parts, the SIFs become:

$$K_I = \sqrt{2}\,(\beta_1 + \gamma_1) \tag{A.30a}$$

$$K_{II} = -\sqrt{2}\,(\mu_2\gamma_1 + \mu_1\beta_1) \tag{A.30b}$$

Substituting Eq. (A.24) into Eq. (A.23b) and setting $j = 1$ yield:

$$\gamma_1 = [(\alpha_2^* - \alpha_1^*)\beta_{n+1} - \beta_1^*\beta_1]/\beta_2^* \tag{A.31}$$

Substituting Eq. (A.31) into Eqs. (A.30) to obtain the SIFs:

$$K_I = \sqrt{2}\,[(1-\beta_1^*/\beta_2^*)\beta_1 + (\alpha_2^* - \alpha_1^*)\beta_{n+1}/\beta_2^*] \tag{A.32a}$$

$$K_{II} = -\sqrt{2}\,\{(\alpha_1^* - \alpha_2^*\beta_1^*/\beta_2^*)\beta_1 + [\beta_2^* - \beta_1^* + \alpha_2^*(\alpha_2^* - \alpha_1^*)/\beta_2^*]\beta_{n+1}\} \tag{A.32b}$$

where the α_1^*, α_2^*, β_1^*, and β_2^* are coefficients of μ_1 and μ_2.

The only unknowns in Eqs. (A.32) are β_1 and β_{n+1}. In order to calculate SIFs, the β_1 and β_{n+1} can be estimated by fitting Eqs. (A.27) with an experimentally or numerically obtained stress/strain field as described in Chapter 3 in this study.

REFERENCES

Anderson, T.L., Fracture Mechanics: Fundamentals and Applications, Third Edition, CRC Press, 2005

Bakis, C. E., Yih, H. R., Stinchcomb, W. W., and Reifsnider, K. L., 1989, "Damage Initiation and Growth in Notched Laminates Under Reversed Cyclic Loading," Composite Materials: Fatigue and Fracture, Second Volume, ASTM STP 1012, Philadelphia, pp. 66-83.

Barone, S., and Patterson, E. A., 1998, "Polymer Coatings as Strain Witness in Thermoelasticity," Journal of Strain Analysis, vol. 33, no. 3, pp. 223-232.

Begley, J. A. and Landes, J. D., 1972, "The J-Integral as a Fracture Criterion," ASTM STP 514, ASTM, pp. 1-20.

Bogdanoff, J. L., 1978, "A New Cumulative Damage Model, Part 1," Journal of Applied Mechanics, vol. 45, pp. 246-250.

Bogdanoff, J. L., 1978, "A New Cumulative Damage Model, Part 3," Journal of Applied Mechanics, vol. 45, pp. 733-739.

Bogdanoff, J. L. and Krieger, W., 1978, "A New Cumulative Damage Model, Part 2," Journal of Applied Mechanics, vol. 45, pp. 251-257.

Bogdanoff, J. L. and Kozin, F., 1980, "A New Cumulative Damage Model, Part 4," Journal of Applied Mechanics, vol. 47, pp. 40-44.

Bogdanoff, J. L. and Kozin, F., 1982, "On Nonstationary Cumulative Damage Models," Journal of Applied Mechanics, vol. 49, pp. 39-42.

Cavaliere, P., Rossi, G. L., Di Sante, R., and Moretti, M., 2007, "Thermoelasticity for the Evaluation of Fatigue Behavior of 7005/AL2O3/10p Metal Matrix Composite Sheets Joined by FSW," International Journal of Fatigue, vol. 30, pp. 198-206.

Creative Pultrusion Inc., 2000, "Pltex Pultrusion Global Design Manual of Standard and Custom Fiber Reinforced Polymer Structural Profiles," vol. 3 - Revision 1, Creative Pultrusions Inc., Alum Bank, PA.

Dally, J. W. and Sanford, R. J., 1987, "Strain-Gage Method for Measuring the Opening-Mode Stress-Intensity Factor, K_I," Experimental Mechanics, vol. 27, no. 4, pp.381-388.

Diaz, F. A., Patterson, E. A., Tomlinson, R. A., and Yates, J. R., 2004, "Measuring Stress Intensity Factors during Fatigue Crack Growth using Thermoelasticity," Fatigue & Fracture of Engineering Materials & Structures, vol. 27, pp.571-583.

Diaz, F. A., Yates. J. R., and Patterson, E. A., 2004, "Some Improvements in the Analysis of Fatigue Cracks using Thermoelasticity," International Journal of Fatigue, vol. 26, pp. 365-376.

Dugdale, D. S., 1960, "Yielding of Steel Sheets Containing Slits," Journal of The Mechanics and Physics of Solids, vol. 8, pp. 100-104.

Dulieu-Smith, J. M., Quinn, S., Shenoi, R. A., Read, P. J. C. L., and Moy, S. S. J., 1997, "Thermoelastic Stress Analysis of a GRP Tee Joint," Applied Composite Materials, vol. 4, no. 5, pp. 293-303.

Dunn, S. A., 1993, "On the Effects of Through-thickness Thermal Conduction on Stress Measurement by Thermoelastic Techniques," Experimental Mechanics, vol. 33, no. 1, pp. 32-36.

El-Hajjar, R., Experimental Study and Analytical Modeling of Translayer Fracture in Pultruded FRP Composites, Ph.D. thesis, Georgia Institute of Technology, 2004.

El-Hajjar, R. and Haj-Ali, R., 2003, "A Quantitative Thermoelastic Stress Analysis Method for Pultruded Composites," Composites Science and Technology, pp. 967-978.

El-Hajjar, R. and Haj-Ali, R., 2004, "IR-Thermography for Strain Analysis in Pultruded Fiber Reinforced Plastics," Experimental Techniques, vol. 28, no.9, pp. 967-978.

El-Hajjar, R. and Haj-Ali, R., 2004, "In-plane Shear Testing of Thick-section Pultruded FRP Composites using a Modified Arcan Fixture," Composites, Part B, vol. 35, no. 5, pp. 421-428.

El-Hajjar, R. and Haj-Ali, R., 2005, "Mode-I Fracture Toughness Testing of Thick Section FRP Composites using the ESE(T) Specimen," Engineering Fracture Mechanics, vol. 72, pp. 631-643.

Gibson, R.F., Principles of Composite Materials Mechanics, McGraw-Hill, 1994.

Griffith, A. A., 1920, "The Phenomena of Rupture and Flow in Solid," Philosophical Transactions of the Royal Society of London, Series A, Royal Society of London, vol. 221, pp.163-198.

Haj-Ali, R., Wei, B. S., Johnson, S., and El-Hajjar, R., 2008, "Thermoelastic and Infrared-Thermography Methods for Surface Strains in Cracked Orthotropic Composite Materials," Engineering Fracture Mechanics, vol. 75, pp. 58-75.

Hutchinson, J. W. 1968, "Singular Behavior at the End of a Tensile Crack Tip in a Hardening Material," Journal of the Mechanics and Physics of Solids, vol. 16, pp. 13-31.

Ingles, C. E., 1913, “Stress in a Plate due to the Presence of Cracks and Sharp Corners,” Transactions of the Naval Architects, vol. 55, pp. 219-230.

Irwin, G. R., 1948, “Fracture Dynamics,” Fracture of Metals, American Society for Metals, pp. 147-166.

Irwin, G. R., 1957, “Analysis of Stress and Strain near the End of a Crack Traversing a Plate,” Journal of Applied Mechanics, vol. 24, pp. 361-364.

Johnson, S. and Haj-Ali, R., 2004, “Infrared Thermography for Fatigue Damage Detection in FRP Composites,” ASC-2004, ASC/ASTM-D30 Joint 19th Annual Technical Conference, 8 pp.

Johnson, S., Kim, H. K., Wei, B. S., and Haj-Ali, R., 2006, “Infrared Thermography for Damage and Fatigue of Thick-Section FRP Composites,” 9th International Fatigue Congress (Fatigue 2006), Atlanta, Georgia, USA, 9 pp.

Ju, S. H. and Rowlands, R. E., 2003, “Thermoelastic Determination of K_I and K_{II} in an Orthotropic Graphite-Epoxy Composite,” Journal of composite materials, vol. 37, pp.2011-2025.

Khalil, S. A., Sun, C. T., and Hwang, W. C., 1986, “Application of a Hybrid Finite Element Method to Determine Stress Intensity Factors in Unidirectional Composites,” International Journal of Fracture, vol. 31, pp.37-51.

Kozin, F. and Bogdanoff, J. L., 1980, “A Critical Analysis of Some Probabilistic Models of Fatigue Crack Growth,” Engineering Fracture Mechanics, vol. 14, pp. 59-89.

Kozin, F. and Bogdanoff, J. L., 1983, “On the Probabilistic Modeling of Fatigue Growth,” Engineering Fracture Mechanics, vol. 18, no. 3, pp. 623-632.

Krueger, R., 2002, “The Virtual Crack Closure Technique: History, Approach and Applications,” NASA/CR-2002-211628, ICASE Report no. 2002-10, April.

Lekhnitskii, S. G., Theory of Elasticity of an Anisotropic Body, Holden-Day, San Francisco, 1963.

Liu, Y. and Mahadevan, S., 2005, “Probabilistic Fatigue Life Prediction of Multidirectional Composite Laminates,” Composite Structures, vol. 69, pp. 11-19.

Liu, Y. and Mahadevan, S., 2007, “Stochastic Fatigue Damage Modeling under Variable Amplitude Loading,” International Journal of Fatigue, vol. 29, pp. 1149-1161.

Loeve, M., Probability Theory, Fourth Edition, New York, Springer, 1977.

Lohr, D. T., Enke, N. F., and Sandor, B. I., 1987, “Analysis of Fatigue Damage Evolution by Differential Infrared Thermography,” Proceedings of the SEM Conference on Dynamic Failure.

Mackenzie, A. K., 1989, “Effects of Surface Coatings on Infrared Measurements of Thermoelastic Responses,” Stress and Vibration: Recent Developments in Industrial Measurement and Analysis, vol. 1084, pp. 59-71.

Maleski, M. J., Kirugulige, M. S., and Tippur, H. V., 2004, “A Method for Measuring Mode I Crack Tip Constraint Under Static and Dynamic Loading Conditions,” Society for Experimental Mechanics, vol. 44, no. 5, pp. 522-532.

Mandell, J. F. and Samborsky, D. D., DOE/MSU Composite Material Fatigue Database: Test Methods, Materials, and Analysis, Contractor Report SAND97-3002, Montana State University, 1997.

Muskhelishvili N. I., Some Basic Problems of the Mathematical Theory of Elasticity, Groningen, P. Noordhoff, 1977.

O’Brian, T. K., 1993, “Local Delamination in Laminates with Angle Ply Matrix Cracks, Part II: Delamination Fracture Analysis and Fatigue Characterization,” Composite Materials: Fatigue and Fracture, Fourth Volume, ASTM STP 1156, Philadelphia, pp. 507-538.

O’Brian, T. K. and Hooper, S. J., 1993, “Local Delamination in Laminates with Angle Ply Matrix Cracks, Part I: Tension Tests and Stress Analysis,” Composite Materials: Fatigue and Fracture, Fourth Volume, ASTM STP 1156, Philadelphia, pp. 491-506.

Rice, J. R., 1968, “A Path Independent Integral and the Approximate Aanalysis of Strain Concentration by Notches and Cracks,” Journal of Applied Mechanics, vol. 35, pp. 379-386.

Rice, J. R. and Rosengren, G. F., 1968, “Plain Strain Deformation near a Crack Tip in a Power Law Hardening Material,” Journal of the Mechanics and Physics of Solids, vol. 16, pp. 1-12.

Roh, Y. S. and Xi, Y., 2000, “A General Formulation for Transition Probabilistic of Markov Model and the Application of Fracture of Composite Materials,” Probabilistic Engineering Mechanics, vol. 15, pp. 241-250.

Rowatt, J. D. and Spanos, P. D., 1998, “Markov Chain Models for Life Prediction of Composite Laminates,” Structural Safety, vol. 20, pp. 117-135.

Rybicki, E. F. and Kanninen, M. F., 1977, “A Finite Element Calculation of Stress Intensity Factors by a Modified Crack Closure Integral,” Engineering Fracture Mechanics, vol. 9, pp. 931-938.

Savin, G. N., Stress Concentration around Holes, International Series of Monographs in Aeronautic, Pergamon Press Ltd., 1961.

Schapery, R. A., 1968, "Thermal Expansion Coefficients of Composite Materials Based on Energy Principles," Journal of Composite Materials, vol. 2, pp. 380-404.

Shih, C. F., 1981, "Relationship between the J-Integral and the crack opening displacement for stationary and extending cracks," Journal of the Mechanics and Physics of Solids, vol. 29, pp. 305-326.

Shukla, A., Agarwal, B. D., and Bhushan, H., 1989, "Determination of Stress Intnsity Factor in Orthotropic Composite Materials Using Strain Gages," Engineering Fracture Mechanics, vol. 32, pp. 469-477.

Sih, G. C., Paris, P. C., and Irwin, G. R., 1965, "On cracks in Rectilinearly Anisotropic Bodies," International Journal of Fracture Mechanics, vol. 1, pp. 189-203.

Surfer 7, Contouring and 3D Surface Mapping for Scientists and Engineers, User's guide, Golden Software Inc., 1999.

Swain, R. E., Bakis, C. E., and Reifsnider, K. L., 1993 "Effect of Interleaves on the Damage Mechanisms and Residual Strength of Notched Composite Laminates Subjected to Axial Fatigue Loading," Composite Materials: Fatigue and Fracture, Fourth Volume, ASTM STP 1156, Philadelphia, pp. 552-574.

Tamuzs, V., Dzelzitis, K., and Reifsnider, K., 2004, "Fatigue of woven composite laminates in off-axis loading I. the mastercurves," Applied Composite Materials, vol. 11, pp. 259-279.

Tamuzs, V., Dzelzitis, K., and Reifsnider, K., 2004, "Fatigue of woven composite laminates in off-axis loading II. prediction of the cyclic durability," Applied Composite Materials, vol. 11, pp.281-293.

Tanimoto, T., 2006, "Correlation of Statistical Fatigue Properties in a Wide Stress Range for FRP Laminates with Failure Mechanisms," International Journal of Fatigue, vol. 28, pp. 1493-1500.

Thomson, W. K., 1878, "On the Thermoelastic, Thermomagnetic, and Pyro-electric Properties of Matter," Philosophical Magazine, vol. 5, pp. 4-27.

Tomlinson, R. A. and Marsavina, L., 2004, "Thermoelastic Investigations for Fatigue Life Assessment," Experimental Mechanics, vol. 44, no. 5, pp. 487-494.

Tong, P., 1975, "A Hybrid Crack Element for Rectilinear Anisotropic Material," International Journal for Numerical Methods in Engineering, vol. 11, pp. 377-403.

Tong, P., Pian, T. H. H., and Lasry, S. J., 1973, “A Hybrid-Element Approach to Crack Problems in Plane Elasticity,” International Journal for Numerical Methods in Engineering, vol. 7, pp. 297-308.

Welch, C. S. and Zickel, M. J., 1993, “Thermal Coating Characterization Using Thermoelasticity,” in Review of Progress in Quantitative NDE, vol. 12B, pp. 1923-1930.

Wells, A.A., 1963, “Application of Fracture Mechanics at and beyond General Yielding,” British Welding Journal, vol. 11, pp. 563-570.

Westergaard H. M., 1939, “Bearing Pressures and Cracks,” Journal of Applied Mechanics, vol. 6, pp. 49-53.

Wong, A. K., Jones, R., and Sparrow, J. G., 1987, “Thermoelastic constant or thermoelastic parameter? Journal of Physics and Chemistry of Solids,” vol. 48, no. 8, pp. 749-753.

Wu, W. F. and Ni, C. C., 2004, “Probabilistic Models of Fatigue Crack Propagation and Their Experimental Verification,” Probabilistic Engineering Mechanics, vol. 19, pp. 247-257.

Xi, Y. and Bazant, Z. P., 1997, “Random Growth of Crack with R-curve: Markov Process Model,” Engineering Fracture Mechanics, vol. 57, no. 6, pp. 593-608.

Zhang, D., and Sandor, B. I., 1989, “Thermographic analysis of stress concentrations in a composite,” Experimental Mechanics, vol. 29, no. 2, pp. 121-125.

Zhang, D. and Sandor, B. I., 1990, “A thermoelsticity Theory for Damage in Anisotropic Materials,” Fatigue & Fracture of Engineering Materials & Structures, vol. 13, no. 5, pp. 497-509.

Zhang, D., Enke, N. F., and Sandor, B. I., 1990, “Thermographic Stress Analysis of Composite Materials,” Experimental Mechanics, vol. 30, no.1, pp. 68-73.

VITA

Bo-Siou Wei was born in Taipei, Taiwan on September 18, 1976. He received his bachelor's and master's degree at National Central University (NCU) in Taiwan. After military service as a second lieutenant in 2003, he began research at the Center for Bridge Engineering Research at NCU. Many new nondestructive and evaluation methods were developed and applied for the existing bridges and buildings. He then came to the U.S. in 2004 to pursue a Ph.D. at Georgia Tech to further explore the nondestructive approaches for composite materials using infrared thermoelastic stress analysis (IR-TSA). Meanwhile, he obtained a second master's degree in Mechanical Engineering at Georgia Tech with a focus in solid mechanics. He is also a registered engineer-in-training in California. A selection of his publications at Georgia Tech follows:

Refereed journals

1. Haj-Ali, R., Choi, J., Wei, B.S., Popil, R.E., and Schaepe, M., 2008, "Nonlinear Refined Finite Element Models for Corrugated Fiberboards," Composite Structures, In press.
2. Haj-Ali, R., Wei, B.S., Johnson, S., and El-Hajjar, R., 2008, "Thermoelastic and Infrared-Thermography Methods for Surface Strains in Cracked Orthotropic Composite Materials," Engineering Fracture Mechanics, vol. 75, pp.58-75.
3. Wei, B.S., Haj-Ali, R., and Johnson, S., "A Non-Stationary Markov Chain Model for Fatigue Prediction in Composites Using Thermoelasticity and Thermography Techniques," submitted.
4. Tan, X., Wei, B.S., Johnson, S., Armanios, E., and Haj-Ali, R., "Damage Progression Assessment of Co-cured Composite," submitted.

Conference proceedings

1. Johnson, S., Wei, B.S., Akil, H.M., and Haj-Ali, R., 2008, "Mechanical Characterization of Jute and Kenaf as Primary Reinforcement in Pultruded Bio-Composites," 23rd Annual Technical Conference of the American Society for Composites (ASC), Memphis, TN, USA.
2. Johnson, S., Wei, B.S., and Haj-Ali, R., 2008, "A Stochastic Fatigue Damage Model for Composite Single Lap Shear Joints Based on Markov Chains and Thermoelastic Stress Analysis," 23rd Annual Technical Conference of the American Society for Composites (ASC), Memphis, TN, USA.

3. El-Hajjar, R., Wei, B.S., Johnson, S., and Haj-Ali, R., 2007, “Quantitative Infrared Thermoelastic Strain Analysis Methods for Notched,” 22nd Annual Technical Conference of the American Society for Composites (ASC), Seattle, Washington, USA.

4. Wei, B.S., Johnson, S., and Haj-Ali, R., 2007, “A Non-Stationary Markov Chain Model for Fatigue Prediction in Composites Using Thermoelasticity and Thermography Techniques,” 18th Engineering Mechanics Division Conference of the American Society of Civil Engineering (ASCE), Blacksburg, Virginia, USA.

5. Choi, J, Wei, B.S., Haj-Ali, R., and Popil, R.E., 2007, “Nonlinear Material and Structural Models for Corrugated Fiberboards and Box Containers,” 18th Engineering Mechanics Division Conference of the American Society of Civil Engineering (ASCE), Blacksburg, Virginia, USA.

6. Popil, R.E., Schaepe, M.K., Haj-Ali, R., Wei, B.S., and Choi J., 2006, “Adhesive Level Effect on Corrugated Board Strength - Experiment and FE Modeling,” Progress in Paper Physics Conference (PPP2006), Oxford, Ohio, USA.

7. Wei, B.S., Johnson, S., and Haj-Ali, R., 2006, “Applied Markov Chain Models to Experimental Fatigue and Computational Damage of Composite materials and Structures,” 7th World Congress on Computational Mechanics (WCCM-7), Los Angeles, California, USA.

8. Haj-Ali, R., Wei, B.S., Johnson S., and El-Hajjar, R., 2006, “Mixed-Mode Stress Intensity Factors in Composite Materials using Quantitative Thermoelasticity,” 14th International Conference on Composites/Nano Engineering (ICCE-14), Boulder, Colorado, USA.

9. Johnson, S., Kim, H.K., Wei, B.S., and Haj-Ali, R., 2006, “Infrared Thermography for Damage and Fatigue of Thick-Section FRP Composites,” 9th International Fatigue Congress (Fatigue 2006), Atlanta, Georgia, USA, 9 pp.